

# Modelling monolithic scintillator detectors for positron emission tomography

The research presented in this thesis was performed at the Radiation Detection & Medical Imaging (RD&M) section of the department of Radiation, Radionuclides & Reactors (R<sup>3</sup>), Faculty of Applied Sciences, Delft University of Technology, Delft, The Netherlands.

Visiting address: Mekelweg 15, 2629 JB Delft, The Netherlands.

# Modelling monolithic scintillator detectors for positron emission tomography

Proefschrift

ter verkrijging van de graad van doctor  
aan de Technische Universiteit Delft,  
op gezag van de Rector Magnificus prof. dr. ir. J.T. Fokkema,  
voorzitter van het College voor Promoties,  
in het openbaar te verdedigen op woensdag 7 oktober 2009 om 10:00 uur

door  
Dingeman Jan VAN DER LAAN

Natuurkundig Ingenieur  
Technische Universiteit Delft  
geboren te Middelharnis

*Dit proefschrift is goedgekeurd door de promotor(en):*

Prof. dr. ir. C.W.E. van Eijk,

Prof. dr. F.J. Beekman.

*Samenstelling promotiecommissie:*

Rector Magnificus, voorzitter

Prof. dr. ir. C.W.E. van Eijk, Technische Universiteit Delft, promotor

Prof. dr. F.J. Beekman, Technische Universiteit Delft, promotor

Dr. ir. D.R. Schaart, Technische Universiteit Delft, copromotor

Prof. dr. ir. L.J. van Vliet, Technische Universiteit Delft

Prof. dr. H. Löhner, Rijksuniversiteit Groningen

Prof. dr. A.A. Lammertsma, Vrije Universiteit Amsterdam

Dr. P. Bruyndonckx, Vrije Universiteit Brussel

Prof. dr. ir. T.H.J.J. van der Hagen, Technische Universiteit Delft, reservelid

© 2009 D.J. van der Laan and IOS Press

All rights reserved. No part of this book may be reproduced, stored in a retrieval system, or transmitted, in any form or by any means, without prior permission from the publisher.

ISBN: 978-1-60750-059-9

Keywords: Monolithic scintillator detectors, positron emission tomography (PET), Monte Carlo simulation, minimum variance bound, spatial resolution

*Published and distributed by IOS Press under the imprint Delft University Press*

*Publisher & Distributor*

IOS Press

Nieuwe Hemweg 6b

1013 BG Amsterdam

Netherlands

fax: +31-20-687 0019

email: info@iospress.nl

*Distributor in the USA and Canada*

IOS Press, Inc.

4502 Rachael Manor Drive

Fairfax, VA 22032

USA

fax: +1-703-323 3668

e-mail: sales@iospress.com

LEGAL NOTICE

The publisher is not responsible for the use which might be made of the following information.

PRINTED IN THE NETHERLANDS

---

# Contents

---

<b>1</b>	<b>Introduction</b>	<b>1</b>
1.1	Introduction PET . . . . .	2
1.2	Purpose . . . . .	4
1.3	Monte Carlo simulations . . . . .	6
1.4	Outline . . . . .	7
<b>2</b>	<b>PET detectors</b>	<b>9</b>
2.1	Introduction . . . . .	9
2.1.1	Spatial resolution . . . . .	9
2.1.2	Signal to noise ratio . . . . .	11
2.1.3	Summary . . . . .	13
2.2	Existing Designs . . . . .	13
2.2.1	Designs for small animal applications . . . . .	14
2.2.2	Designs with depth-of-interaction determination . . . . .	18
2.3	Monolithic scintillation detectors . . . . .	19
2.3.1	Introduction . . . . .	19
2.3.2	Position estimation . . . . .	20
<b>3</b>	<b>Optical simulations</b>	<b>23</b>
3.1	Introduction . . . . .	23
3.2	Methods and materials . . . . .	24
3.2.1	Description of the PET detector . . . . .	24
3.2.2	Simulation parameters . . . . .	25
3.2.3	Spatial resolution measurements . . . . .	27
3.2.4	Monte Carlo simulations . . . . .	28
3.3	Results and discussion . . . . .	31
3.3.1	Simulation parameters . . . . .	31
3.3.2	Comparison between simulation and experiment . . . . .	33
3.4	Conclusions . . . . .	39

<b>4</b>	<b>The influence of statistics and noise</b>	<b>41</b>
4.1	Introduction . . . . .	42
4.2	Theory . . . . .	43
4.2.1	Model of the observations . . . . .	44
4.2.2	Lower bound for independent detector signals . . . . .	45
4.2.3	Covariance between detector signals . . . . .	47
4.3	Materials and methods . . . . .	48
4.3.1	Detectors . . . . .	48
4.3.2	Cramér-Rao model input parameters . . . . .	49
4.3.3	Optical simulations . . . . .	49
4.3.4	Comparison with experiment . . . . .	50
4.4	Results and discussion . . . . .	52
4.4.1	Comparison with experiment . . . . .	52
4.4.2	Influence of the detector properties . . . . .	54
4.4.3	Influence of covariance between detector signals . . . . .	57
4.5	Conclusion . . . . .	58
<b>5</b>	<b>Point spread function</b>	<b>61</b>
5.1	Introduction . . . . .	61
5.2	Model . . . . .	62
5.2.1	Detector operating principle . . . . .	62
5.2.2	Model of the detector PSF . . . . .	63
5.3	Materials and methods . . . . .	66
5.3.1	Detector . . . . .	66
5.3.2	Measurement setup . . . . .	67
5.3.3	Spatial resolution measurements . . . . .	68
5.3.4	Simulation of scattering and beam . . . . .	68
5.3.5	Model fitting procedure . . . . .	69
5.4	Results and discussion . . . . .	69
5.4.1	Detector PSF . . . . .	69
5.4.2	Correction for test beam diameter . . . . .	70
5.4.3	Validation of the model . . . . .	72
5.5	Conclusions . . . . .	76
<b>6</b>	<b>Simulated scanner performance</b>	<b>77</b>
6.1	Introduction . . . . .	78
6.2	Methods . . . . .	78
6.2.1	Monte Carlo simulations . . . . .	78
6.2.2	Intrinsic detector PSF . . . . .	80
6.2.3	Scanner performance . . . . .	81
6.3	Results . . . . .	82
6.3.1	Spatial resolution . . . . .	82
6.3.2	Sensitivity . . . . .	84
6.3.3	Count rate performance . . . . .	84
6.4	Discussion . . . . .	84
6.5	Conclusions . . . . .	89

<b>7 Conclusion</b>	<b>91</b>
7.1 The parameters and their importance . . . . .	92
7.2 Conclusion . . . . .	95
<b>A The influence of geometry</b>	<b>97</b>
A.1 Introduction . . . . .	97
A.2 Cramér-Rao lower bound . . . . .	100
A.3 Methods . . . . .	102
A.3.1 Cramér-Rao simulations . . . . .	102
A.3.2 Simulations using beams . . . . .	104
A.4 Results and Discussion . . . . .	105
A.4.1 Cramér-Rao results . . . . .	105
A.4.2 Comparison with beam simulations . . . . .	110
A.5 Conclusion . . . . .	112
A.6 Acknowledgments . . . . .	114
<b>B Derivation of the covariance matrix</b>	<b>115</b>
<b>Summary</b>	<b>125</b>
<b>Samenvatting</b>	<b>129</b>
<b>Curriculum Vitae</b>	<b>133</b>
<b>List of publications</b>	<b>135</b>



# CHAPTER 1

---

## Introduction

---

Monolithic scintillators combined with arrays of solid state light detectors can be used to build novel types of detectors for high-resolution positron emission tomography (PET). From calculations and measurements these detectors seem very promising. The most important advantage of these detectors is that PET systems based on these detectors can have a much higher sensitivity. Furthermore, because they use solid state light detectors, they can be combined with other imaging modalities such as MRI. The intrinsic spatial resolution of these detectors seems to be comparable to that of current high-resolution PET detectors that use small scintillator crystals coupled to photo-multiplier tubes (PMTs). One part of this work aims to further investigate the performance of these detectors and to investigate whether or not these detectors are indeed promising for high-resolution and high-sensitivity PET. The other more important part aims to obtain a qualitative and quantitative understanding of the relation between the properties of the detector such as shape, dimensions, materials used, etc. and the performance of the detectors. A better understanding of the influence of design parameters on the performance is useful to obtain a better design. Therefore, a large part of this thesis is devoted to modelling of the detector.

Although the monolithic scintillator detectors investigated here are developed for high-resolution PET, this type of detector can also be used for other applications in which one needs to determine the position of ionizing particles. The models derived here can easily be adapted for many other types of detector that determine the position of the ionizing particles from the distribution of scintillation light on a position-sensitive light detector.

Before discussing the main goals of this thesis, a short introduction to PET is presented. Finally, the use of Monte Carlo simulations for studying these detectors is discussed, followed by an outline of this thesis.

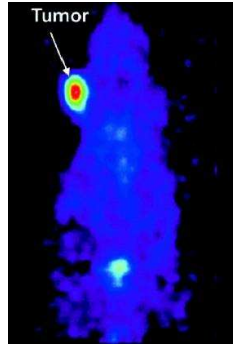


FIGURE 1.1: *PET image of a rat injected with a tracer that accumulates in tumor tissue.*

## 1.1 Introduction PET

PET is an imaging technique that measures the distribution of a tracer inside a subject to be investigated, e.g. a human body or animal. A tracer consists of molecules of which one or more atoms have been replaced by radioactive atoms. This tracer is injected into the bloodstream of the patient. Depending on the kind of tracer used, it accumulates after injection in certain parts of the body. The PET scanner detects the radiation emitted by the radioactive atoms and the distribution of the radioactive atoms inside the body can be reconstructed.

For example, a much used tracer is FDG (Fluorodeoxyglucose) which is similar to glucose. Tissues that need energy take up the FDG and break it down into smaller molecules. Therefore, the FDG accumulates in tissues that use energy. This could be active parts of the brain, but also tumors, since tumor tissue often uses much glucose. Figure 1.1 shows a PET image of a rat with a tumor in its neck. The blue parts of the image contain a low concentration of tracer, while the green/red parts contain a higher concentration. The tracer has accumulated in the tumor, making the tumor clearly visible in the image.

The question then is: ‘How does a PET scanner measure the distribution of the tracer inside the body?’ The radioactive atoms of the tracer emit positrons (the ‘E’ and ‘P’ of PET). When the positron has lost its energy, it annihilates with an electron and two annihilation photons are formed that travel in almost opposite directions. A PET scanner tries to detect both of these annihilation photons. We then know that the tracer was located somewhere along the line between the two detection points. This line is called the line of response (LOR). A large number of these LORs (typically millions) are collected. From these LORs the distribution of the tracer can be estimated.

Figure 1.2 illustrates how the distribution of the tracer can be reconstructed from the LORs. Suppose we only collect LORs that are vertical or horizontal. We create a histogram of the LORs for each of the two directions. These histograms are called projections. What we then could do is back-project these histograms as is shown in the second figure. This results in a very crude approximation of the source. When the number of angles for which we collect the LORs increases,

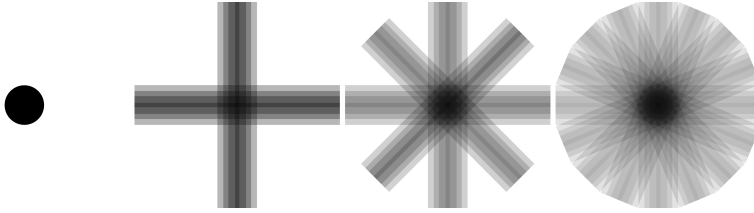


FIGURE 1.2: *Simplified view of 2D image reconstruction of a cylinder (first image; black circle). The second to fourth images show the resulting reconstruction as the number of projections increase.*

as is shown in the other two images, we see that the back-projection starts to look more and more like the original source. The way the reconstruction is done in an actual scanner is more complicated, but this example illustrates how the three dimensional distribution of the tracer can be determined from the LORs.

### Comparison to other imaging modalities

As was mentioned in the previous section, PET images the distribution of a tracer inside the body. This tracer is a chemical substance, and by choosing a specific tracer a specific chemical process inside the body can be imaged. This is one of the major differences with other imaging modalities: with PET, chemical processes can be imaged. Most other imaging modalities, e.g. CT and MRI, mainly image anatomy.

PET images tissue function, and sometimes anatomical information is needed to be able to determine precisely where inside the body the process that is imaged with PET takes place. Therefore, PET images are often combined with anatomical images, usually CT images. The CT image gives the anatomical information, while the PET image gives information on the chemical process.

Two other imaging modalities can also image chemical processes: functional-MRI and SPECT [50]. However, the sensitivity of PET is much higher than these two modalities. The sensitivity of PET is  $10^2$ – $10^3$  higher than that of SPECT [14]. Especially functional-MRI has in comparison a very low sensitivity. Therefore, PET can detect much smaller quantities of tracer and with PET it is also easier to accurately quantify the amount of tracer inside a (part of a) certain organ. One of the advantages of the new detectors discussed in this thesis is that the sensitivity of a scanner based on these detectors can be much higher than in current PET scanners, while maintaining the spatial resolution of these scanners. This makes it possible to better create dynamic PET images: chemical process can be followed in time.

The main disadvantage of PET, when compared to other imaging modalities is its limited spatial resolution (suppose all tracer is concentrated at one point; the reconstructed image will not show a point but a volume; the bigger the volume the worse the spatial resolution; the spatial resolution is usually specified by giving the full width at half maximum of this volume). As will be discussed in the next chapter the spatial resolution of a PET scanner can be in the order

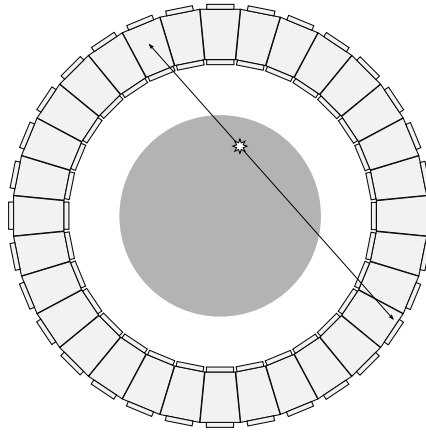


FIGURE 1.3: *Transaxial view of a PET scanner: the dark gray circle represents the patient, around it a ring of detectors.*

of 0.5–1 mm, while the spatial resolution of for example CT can be in the order of 10  $\mu\text{m}$ .

#### Parts of a PET scanner

Since the scanner has to detect two photons that travel in approximately opposite directions, most scanners are cylindrically shaped. The patient is located in the center of the scanner. Figure 1.3 shows an example. The scanner usually consists of multiple rings of detectors. A detector can detect one annihilation photon at a time. Detectors usually consist of one or more scintillation crystals in which the annihilation photon interacts. The energy lost by the annihilation photon during the interaction(s) is converted into light in the scintillation crystals. Attached to the scintillation crystals are light sensors. The signal of the light sensor is furthermore processed by front-end electronics and finally the detector signals are digitized and sent to a computer, where the information of all detectors is combined and preprocessed for the image reconstruction.

## 1.2 Purpose

In recent years there has been an increase of interest in small animal positron emission tomography (PET). Small animal PET requires a high spatial resolution and, especially when dynamic studies are to be performed, a high sensitivity [13] (the amount of tracer that can be used in these animals is limited). In order to achieve the required resolution, most current designs use arrays of small scintillation crystals coupled to position-sensitive photomultiplier tubes (PMTs). Although in principle the resolution can be improved in this design by decreasing the dimensions of the crystals, much sensitivity is lost when decreasing the crystal size because of the dead space between the crystals occupied by reflective

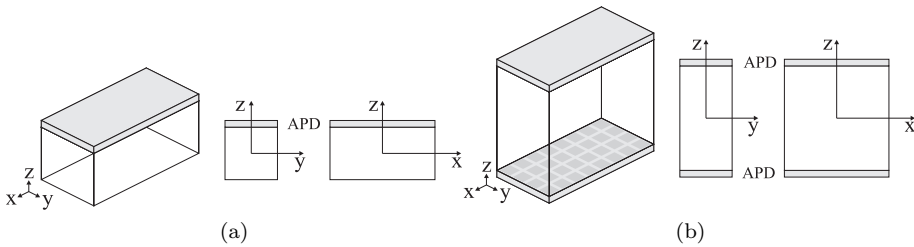


FIGURE 1.4: *Two examples of monolithic scintillation detectors. The arrow indicates the direction of the annihilation photons. (Left) a  $20 \times 10 \times 10 \text{ mm}^3$  LYSO crystal read out by a Hamamatsu S8550 APD array that is attached to the side at which the beam enters the crystal, and (right) a  $20 \times 10 \times 20 \text{ mm}^3$  LYSO crystal read out by two APD arrays.*

material for optical separation. Additional dead space may exist between the detector modules, which may, for example, be dictated by the relatively large size of the position-sensitive photomultiplier tubes. Finally, increasing the length of the crystals in order to increase the sensitivity requires correction for the depth-of-interaction (DOI), since otherwise the resulting parallax error will decrease the resolution outside the center of the scanner (see the next chapter for more details on DOI and ‘parallax error’).

Monolithic scintillation detectors can avoid these problems. These detectors consist of a continuous scintillation crystal read out by position sensitive photodetectors. The Philips CPET system is, for example, based on this type of detector [4], although the design of the detector is different from that of the detector investigated in this thesis. The CPET does not have DOI correction. Designs with DOI correction have also been investigated [19, 16, 6], but these are either too complicated or have insufficient spatial resolution for small animal PET.

The detectors investigated in this thesis consist of several cubic centimeters of scintillating material coupled on one or more sides to avalanche photo-diode (APD) arrays. Two examples of this detector are shown in figure 1.4. The coordinates of the entry point of an incoming gamma photon are estimated from the light distribution on the pixels of the APD arrays. Before estimation can take place, the estimation algorithm has to be trained using measured light distributions produced by annihilation photons with known entry points.

Compared to detectors using arrays of small crystals, the proposed monolithic scintillation detectors have several advantages. First of all, the detection efficiency is increased because the dead space between the crystals in a crystal array is avoided and because the dead space between the detector modules can be minimized due to the small size of the APD arrays. They are also easier to manufacture. Furthermore, integration with MRI devices may become possible because of the use of APD arrays instead of PMTs. Measurements performed on this type of detector have shown that the intrinsic detector resolution is comparable to that of detectors using arrays of small crystals [42, 10, 11].

The performance of these detectors is determined by a large number of factors, such as the type of scintillator used, the type of APD array used, electronic noise, the position estimation algorithm. A better understanding of the relation between these factors and the performance will lead to a more efficient optimization of the design. Therefore, the main research question of this work is:

*What processes influence the performance of PET detector modules based on monolithic scintillation crystals read out by avalanche photo-diode arrays and in what way do they influence the performance?*

The second part of the question will be *quantified* as much as possible. The focus will be on the spatial resolution of the detectors. Although other performance measures of the detectors are also relevant, as will be shown in the next chapter, this part of the performance is most difficult to model. The sensitivity of the detector is discussed in chapter 6. I will focus on the scintillator LSO/LYSO, since this scintillator at present has the best properties for high resolution PET. There are some other scintillators that are very promising, especially LaBr, but this material was not yet available. As for the avalanche photo-diode array, I will focus on the Hamamatsu S8550 APD array, since this is at the moment one of the few APD arrays suitable for PET that is commercially available.

### 1.3 Monte Carlo simulations

Simulations are a very powerful tool to investigate the influence of design parameters on the performance of detectors. Of course, simulations will always be a approximation of reality, but in simulations it is possible to vary parameters that can not be varied in measurements. What would be the performance if we would have no electronic noise? What would be the performance if radiation did not scatter? Questions like this cannot be answered by measurements, but can give valuable information on how the system works. Since the focus of this thesis is to get a better understanding of the behaviour of the system, simulations will be the main tool. Of course, the input will be based on measurements and the output will be compared to measurements.

For simulating these detectors, I used Monte Carlo simulations. Monte Carlo simulations are basically simulations that use random numbers (hence the name Monte Carlo). Since transport of radiation is by nature a stochastic process<sup>1</sup>, Monte Carlo simulations lend themselves very well to this type of problem.

An example: Suppose we have an annihilation photon with an energy of 511 keV traveling through a certain material. There are a number of interactions this photon can have: it can Compton scatter or it can undergo photo-electric absorption. Both types of interactions have a constant probability per distance travelled in a given material. The simulation program determines for each of the processes the (random) distance at which the interaction would occur. The interaction with the shortest distance is selected. The photon is transported the given distance and then undergoes the interaction, where new particles (e.g.

---

<sup>1</sup>Or can at least be modelled very accurately as a stochastic process.

electrons, photons) may be created and the properties of the photon (e.g. energy, direction) are modified. This is repeated until all particles are stopped.

## 1.4 Outline

Chapter 2 discusses detector modules for high-resolution PET and the performance of these detectors in more depth and gives an overview of the high-resolution PET detector modules that are currently on the market. This chapter can be skipped by those who are already familiar with PET detectors. Chapters 3 through 6 are the main part of the thesis.

Chapter 3 shows how monolithic scintillator detectors can be modelled with the Monte Carlo codes GEANT4 [5] and GATE [30]. For an accurate simulation of these detectors a large number of parameters need to be specified accurately. The chapter shows how these parameters can be determined and validates the simulations against measurements. As part of this work, a module for performing optical simulations of scintillation detectors has been added to GATE. The parameters determined in this chapter are used in the subsequent chapters.

In chapter 4 a statistical model of the measured signals is determined. This model is used to derive the Cramér-Rao lower bound or minimum variance bound on the spatial resolution. This lower bound gives the relation between the best possible resolution that can be obtained the design parameters of the detector. This gives valuable insight in the performance of the detector, which can be used to optimize the design. It can furthermore be used to check if the position estimation algorithm is performing well by comparing the measured spatial resolution to the lower bound.

The spatial resolution of PET detectors is usually measured by measuring the point spread function (PSF), which gives the probability distribution of the measured position around the true position. The shape of the PSF depends on the properties of the detector and the estimation algorithm. Chapter 5 gives a model for the measured PSF.

Until chapter 6, all chapters focus on the performance of a single detector module. In chapter 6 the measured properties of such a detector module are used in a simulation of a complete small animal scanner based on monolithic scintillator detectors. The sensitivity, count rate performance and spatial resolution of such a scanner is investigated.



# CHAPTER 2

---

## PET detectors

---

**This chapter first describes the properties that a good PET detector should have. Subsequently an overview of existing designs is given. Finally, a description of the proposed detector design is given: the monolithic scintillation detector.**

### 2.1 Introduction

PET scanners usually consist of one or more rings of detectors. In this section we will discuss what a good detector module has to do, the limitations of detectors and what designs are being used at the moment with their advantages and disadvantages. Finally, we will discuss how monolithic scintillation detectors work.

In order to determine what a detector has to do, we first need to determine what a PET scanner has to do. With a PET scanner, the distribution of a radiotracer inside a body is determined. We would like to have this distribution with a high resolution, so that we may look at the concentration of tracer in very small volumes, with a high accuracy and a high precision.

#### 2.1.1 Spatial resolution

The spatial resolution of a scanner determines how close the LOR passes the molecule which emitted the primary positron. A number of factors contribute to this spatial resolution. A first factor is the positron range. After being emitted the positron travels through the material until it is almost completely stopped. At that point the probability of annihilation with an electron increases strongly. The range the positron travels depends on the primary energy and therefore on the isotope used (see table 2.1).

TABLE 2.1: *Properties of common isotopes used in PET [66].*

Isotope	<sup>11</sup> C	<sup>13</sup> N	<sup>15</sup> O	<sup>18</sup> F	<sup>68</sup> Ga	<sup>82</sup> Rb
Half life (minutes)	20.3	9.97	2.07	109.7	68.3	1.3
Maximum $\beta^+$ energy (MeV)	0.96	1.19	1.70	0.64	1.90	3.15
Radial range in water (mm)						
50% absorption	1.11	1.42	1.49	1.02	1.68	1.69
90% absorption	2.19	2.78	2.57	1.80	3.95	5.80

A second resolution limiting factor is the acollinearity of the two annihilation photons. The positron will have lost most of its energy when it annihilates; however, the electron, being bound to an atom, will have momentum. From the conservation of momentum it then follows that the annihilation photons will not have exactly opposite directions. Since it is the electron that has the momentum, this deviation from opposite directions depends on the material. It is usually around  $0.5^\circ$  FWHM. More information on this angle can be found in chapter 3. The distance of the LOR from the annihilation position depends on the radius of the scanner and the position of the annihilation according to

$$\epsilon_{acoll} = \frac{r_1 r_2}{r_1 + r_2} \sin \varphi_{acoll} \quad \varphi_{acoll} \rightarrow 0, \quad (2.1)$$

where  $r_1$  and  $r_2$  are the distances of the first and second annihilation photon to their respective detectors, and  $\varphi_{acoll}$  is the acollinearity angle. This error is largest in the center of the scanner. For a typical small-animal scanner diameter of 12 cm, this results in a acollinearity contribution of approximately 0.25 mm.

The spatial resolution is furthermore limited by the fact that it is not possible to determine exactly where each of the annihilation photons entered the detectors. The reasons for this are one of the main topics of the thesis and will be discussed in more depth later. The spread of the estimated entry point around the true entry point is called the line spread function (LSF), when we look at only one coordinate, or the point spread function (PSF), when we look at both coordinates. Usually the FWHM and FWTM of these functions are used to specify the detector resolution.

Combining the contributions mentioned above, the spatial resolution in the center of the scanner can be written as

$$\epsilon \approx \sqrt{\frac{\epsilon_{spat}}{2} + \left(\frac{\sin 0.5^\circ}{4} D\right)^2 + r_{positron}^2} \quad (2.2)$$

where  $\epsilon_{spat}$  is the detector resolution in FWHM of the LSF,  $D$  the diameter of the scanner, and  $r_{positron}$  the FWHM of the positron range distribution. Only the detector resolution term can be improved upon by the detector design. The other terms are largely fixed and therefore impose a limit on the spatial resolution achievable with PET.

Another cause of resolution loss is the parallax error. Most current PET detector designs use small long scintillation crystals to determine the entry point

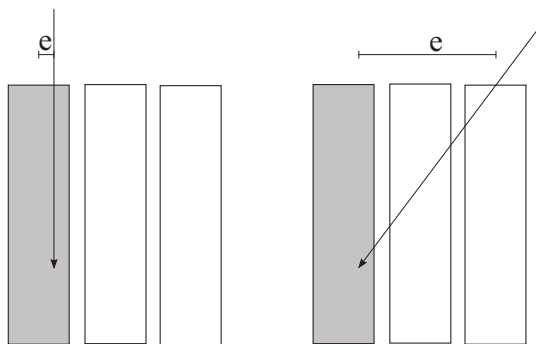


FIGURE 2.1: *The parallax error.  $e$  is the error between the entry point of the photon in the detector and the centre of the crystal in which the photon is detected.*

of the annihilation photons. The entry point is determined by the scintillation crystal in which the annihilation photon was detected (see figure 2.1). When the annihilation photon enters the detector under an angle, the difference or error between the entry point of the photon and the center of the scintillation crystal becomes larger. The further away from the center of the scanner the annihilation took place, the larger the incident angles of the annihilation photons become. Therefore, in most designs the resolution becomes worse further away from the center of the scanner.

The parallax error can be avoided in two ways. In the first method, also the depth at which the annihilation photon was absorbed in the detector is determined from the signals that come from the detector. In the second method, knowledge of the incident angle is used in combination with the signals to determine the entry point directly. The incident angle can be determined from the position at which the second annihilation photon was absorbed.

### 2.1.2 Signal to noise ratio

In principle we want to know the activity of the tracer in each voxel as accurately as possible. After reconstruction of the image, we have an estimate of the number of annihilations in each voxel. As the measurement is based on a counting process, this number will follow approximately a Poisson distribution. Therefore, the precision is limited by the number of LORs that are measured. The number of measured LORs can be increased by increasing the activity, by measuring longer, or by increasing the sensitivity<sup>1</sup> of the scanner. An increase of activity or measurement time is in practice not always possible, therefore, it is desirable to increase the sensitivity of the scanner. The sensitivity is the probability of detecting both photons of one annihilation (a true LOR or a ‘true’).

The sensitivity can be increased by increasing the solid angle of the scanner

---

<sup>1</sup>The sensitivity is the fraction of annihilation photon pairs emitted by the tracer that is detected by the scanner.

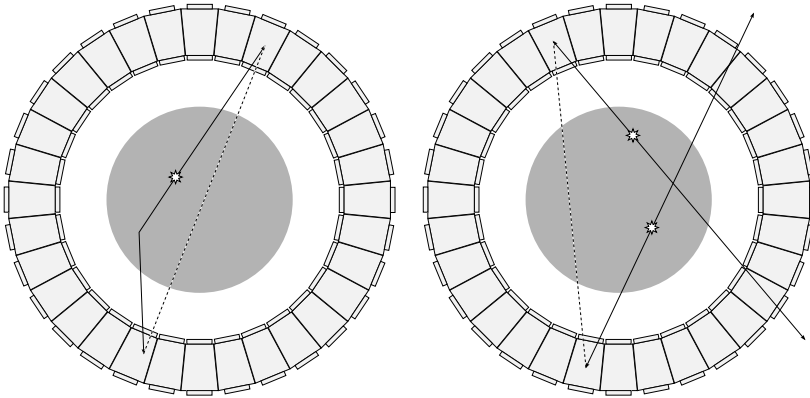


FIGURE 2.2: *The left image shows scatter, the right randoms. The solid lines are the trajectories of the annihilation photons, the dotted line is the resulting line-of-response.*

with respect to the subject and by increasing the detector efficiency, which is the probability that a photon is detected given that the photon passes through the detector. Since two annihilation photons have to be detected to have a LOR, the sensitivity increases with the cube of the detector efficiency. When the activity is high, it can happen that a photon is detected by a detector, while this detector is not yet finished with processing the previous event. These events are usually lost, therefore decreasing the detector efficiency. The time between the detection of one event till the moment the detector is ready to accept the next event is called the dead time<sup>2</sup>.

Another problem is that measured LORs do not always pass through the voxel in which the annihilation took place. In this case, both the accuracy and the precision are affected. This can be caused by the limited spatial resolution of the detector. However, in that case the measured LOR will usually still be close to the true LOR. Scatter and randoms have a much stronger effect. Scatter occurs when one or both of the annihilation photons is scattered inside the subject and both are detected by the scanner. The photons will still be in coincidence, however, the measured LOR is no longer correct. Through scattering the annihilation photons loose energy. Therefore, when the energy resolution of the detector is high enough, scatters can be detected. However, this only works when the detector absorbs all energy of the annihilation photons.

Randoms occur when two photons are detected at almost the same time that come from different annihilations<sup>3</sup>. Events that occur within a certain time window are considered to be from one annihilation. The width of this window is

<sup>2</sup>To be more specific: most scanners have multiple dead times on different levels of the scanner, e.g. detector level, module (containing multiple detectors) level, etc.

<sup>3</sup>When more than two photons are detected at the same time, it is known that random events have occurred. Most scanners ignore these events. However, some other method of dealing with these events might be possible.

determined largely by the timing resolution (the precision with which the time of an interaction inside the detector can be determined) of the detector. Decreasing the width of the timing window will decrease the number of randoms, but at the expense of sensitivity. Increasing the sensitivity of the scanner and the activity will also increase the probability of randoms.

Fortunately, it is possible to correct the image for the randoms and the scatter. Unfortunately, this introduces noise in the image. The total signal-to-noise ratio inside a voxel can be shown to be proportional to [72]

$$NEC = \frac{T^2}{T + S + 2kR} \quad (2.3)$$

where NEC is the number of noise equivalent counts, and  $T$  is the number of trues,  $R$  the number of randoms,  $S$  the number of scatters, and  $k$  the ratio of the diameter of the subject to the diameter of the field-of-view (FOV) of the scanner. It is more common to use rates (events per second), which gives the noise equivalent count rate (NECR).

### 2.1.3 Summary

Summarizing, we want our detectors to have:

**High detector resolution** Increases the spatial resolution in the image. In order to have good spatial resolution away from the center of the scanner the detector also needs to correct for the DOI.

**High efficiency** Increases the number of measured LORs and therefore increases the signal. However, also the noise (randoms and scatters) increases.

**Good timing resolution** Decreases the noise in the image by reducing the randoms.

**Good energy resolution** Decreases the noise in the image by reducing the scatters.

**Small dead time** Increases the detector efficiency for high activities. Higher activities can be used.

## 2.2 Existing Designs

In this section we will discuss a number of existing designs for small-animal PET scanner. Where possible the following performance parameters of the scanners are given: the trans-axial resolution of a point or line source in the center of the scanner determined using filtered back-projection (FBP), the sensitivity (number of detected LORs per second divided by the activity of the source) of the scanner measured using a point source in the center of the scanner, and the energy resolution of the detectors. Most current designs have only limited DOI correction. Therefore, we will also discuss different methods of DOI correction.

### 2.2.1 Designs for small animal applications

#### MicroPET R4

The microPET systems are based on a design from UCLA [15]. The scanner was commercialized by Concorde Microsystems which has recently been taken over by Siemens. The microPET R4 is a 4 ring system designed for rodents and has been evaluated by C. Knoess et al. [35].

Since it is a system for rodents the ring diameter is 148 mm (animal port 120 mm). The axial FOV is 78 mm. The detectors consist of a  $19 \times 19 \times 10$  mm<sup>3</sup> LSO crystal sawed into a  $8 \times 8$  array with 9 mm deep cuts. The cuts are filled with reflective material. The size of the pixels is  $2.2 \times 2.2$  mm with a pitch of 2.45 mm. They are coupled to a position-sensitive PMT using optical fibers to make close packing of the detectors possible. There are 24 mm detector modules in a ring.

The measured image resolution in the center is 1.85 mm FWHM in axial direction and 1.66 mm in trans-axial direction (measured with a 1 mm diameter <sup>22</sup>Na point source using FORE+2D-FBP reconstruction and an energy window of 350–750 keV). The maximum sensitivity is 4.37% for a point source in the center of the FOV (energy window 250–750 keV). The maximum NECR is 174 kcps for a mouse phantom and 93 kcps for a rat phantom (using a coincidence window of 6 ns). The average energy resolution is 23% and varies between 17 and 36% per detector.

#### MicroPET P4

This scanner uses the same detectors as the microPET R4, but since it is designed for primates it has a ring diameter of 260 mm and used 42 detector modules in a ring. It has been evaluated by Y.C. Tai et al. [75]. The timing resolution is 3.2 ns, the average energy resolution 26%. The image resolution (using a  $\varnothing 0.5$  mm <sup>22</sup>Na point source and FORE+2D-FBP reconstruction) drops from 1.8 mm FWHM to 3 mm, 2.4 mm and 2.6 mm at four centimeter from the center in radial, tangential and axial direction, respectively. The sensitivity at the center is 2.25% and the NECR peaks at 100 to 290 kcps (using a time window of 10 ns and an energy window of 250–750 keV).

#### MicroPET II

The microPET II is designed for a higher resolution than the above two microPET systems. It has been evaluated by Y.C. Tai et al. [76]. The scanner consists of 90 detector modules in three rings, resulting in a ring diameter of 16 cm and an axial length of 4.9 cm. The detector is in principle the same, only the crystal consists of  $14 \times 14$  LSO crystals measuring  $0.975 \times 0.975 \times 12.5$  mm<sup>3</sup>. The crystal pitch is 1.15 mm. The absolute sensitivity at the center of the FOV is 2.26% (using an energy window of 250–750 keV and a coincidence window of 10 ns). The average intrinsic spatial resolution of the detectors is 1.21 mm FWHM (measured using a 0.5 mm <sup>22</sup>Na source) and varies from 1.01 mm to 1.34 mm. The image resolution (using a  $\varnothing 250$   $\mu$ m <sup>18</sup>F needle source and FORE+2D-FBP) is 0.83 mm FWHM in the center and drops to 1.47 mm, 1.17 mm, 1.42 mm (radial, tangential, axial)

at one centimeter from the center. The mean energy resolution is 42% and varies from 28% to 75% per detector.

### MicroPET Focus

The microPET Focus is one of the most recent scanners [77]. The scanner has 168 detectors in 4 rings. The ring diameter is 25.8 cm and the axial length of the scanner is 7.6 cm. Each detector consists of  $12 \times 12$   $1.51 \times 1.51 \times 10 \text{ mm}^3$  LSO crystals with a pitch of 1.59 mm. Compared to the previous scanners the dead space between the pixels is reduced strongly. Therefore it can have a higher sensitivity as the microPET R4, even though it has approximately the same ring diameter and length. The absolute sensitivity is 3.4% at the center (250–750 keV energy window, 10 ns time window). The NECR reaches 645 kcps for a mouse phantom (250–750 keV energy window, 6 ns time window). The average energy resolution of the detectors is 18.5%. The image resolution in the center is 1.3 mm FWHM in radial and tangential direction and 1.45 mm in axial direction (0.5 mm  $^{22}\text{Na}$  source, energy window of 250–750 keV, reconstruction using FORE+2D-FBP). The image resolution remains below 1.80 mm FWHM at 1 cm radial offset.

### ClearPET

The ClearPET scanner is developed by the Crystal Clear Collaboration and comprises actually a number of slightly different scanners. The results presented here are for the ClearPET-Neuro developed at Forschungszentrum Jülich [87, 34], since only results for that scanner have been published. Since the ClearPET-Neuro is meant to be used for both rodents and primates (monkeys), the diameter of the scanner can be varied from 13 to 30 cm by moving the detectors in the radial direction.

The axial length of the scanner is 11 cm. The ring consists of 20 detector modules. Each detector module contains four detector modules. Every other module is shifted by 7 mm to obtain a more uniform sensitivity. The detectors are phoswich detectors: the inside layer is LuYAP and the outside layer LSO. The two layers can be distinguished by the different decay times of the scintillators. Each layer consists of  $8 \times 8$  crystals with a pitch of 2.3 mm. The crystals are coupled to a position-sensitive PMT using a mask that corrects the gain non-uniformities of the PMT channels.

The modules have an effective deadtime of 36 ns and a timing resolution of 2 ns. The average energy resolution of the LuYAP layer is 24.3% and that of the LSO layer is 23.2%. The intrinsic spatial resolution of the detectors is 1.48 mm. The reconstructed image resolution in the center is 1.64 mm FWHM, which drops to 1.7 mm at 4 cm from the center (measured using a  $\varnothing 0.5 \text{ mm}$   $^{18}\text{F}$  line source, an energy window of 350–650 keV and 3D-OSEM reconstruction). The simulated sensitivity is 4.2% [65] for the smallest diameter.

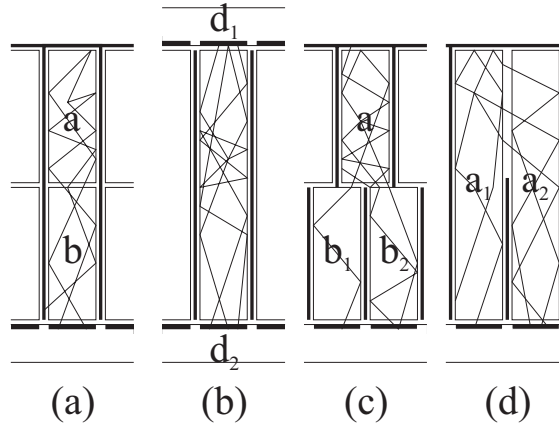


FIGURE 2.3: Some detector designs with depth-of-interaction determination: (a) Phoswich, (b) double-sided readout, (c) and (d) light sharing.

### MADPET-II

The MADPET-II is developed at the Technische Universität München [49]. The unique elements in this scanner are the detector modules that consist of two layers of LSO pixels each read out by a Hamamatsu S8550 APD array. The layers consist of  $8 \times 4 \times 2 \times 2 \times 6 \text{ mm}^3$  and  $2 \times 2 \times 8 \text{ mm}^3$  crystals for the front and back layer, respectively. Because of the two layers, this detector has depth-of-interaction correction. Each individual crystal is read out by a pixel of the APD array. The pitch between the pixels is 2.3 mm.

The scanner consists of a ring of 18 detector modules and has an inner diameter of 71 mm and an axial FOV of 18 mm. The energy resolution of the modules is between 20.2% and 23.9%; the overall timing resolution is 10.2 ns. The system resolution is determined from Monte Carlo simulations and is 1.1 mm FWHM in the center of the scanner.

### HIDAC

While all previous designs use small scintillator crystals coupled to light detectors [32], the HIDAC uses gas filled chambers. Because of this design a very high resolution is possible and the detector also has DOI correction. A disadvantage is the low sensitivity. A reconstructed image resolution is 1.21 mm FWHM trans-axial and 1.31 mm FWHM axial for a  $\varnothing 0.5 \text{ mm}$   $^{22}\text{Na}$  point source (using 3D-OSEM reconstruction). The sensitivity is 0.9% using a  $^{22}\text{Na}$  point source in the center of the scanner.

TABLE 2.2: Specifications of small-animal PET scanners. The image resolution is the trans-axial resolution in the center of the scanner; the number between brackets is the axial resolution. As the HIDAC uses gas filled chambers some of the fields are not relevant.

Scanner	N-crystals	Scintillator	Crystal size	Pitch	E-res	Image-res	Sensitivity
MicroPET R4	8×8	LSO	2.2×2.2×10	2.45	23	1.66(1.85)	4.4
MicroPET P4	8×8	LSO	2.2×2.2×10	2.45	26	1.8	2.3
MicroPET II	14×14	LSO	0.975×0.975×12.5	1.15	42	0.83	2.3
MicroPET Focus	12×12	LSO	1.51×1.51×10	1.59	19	1.3(1.45)	3.4
ClearPET Neuro	8×8	LSO/LuYAP	2×2×2×10	2.3	24/23	1.64	4.2
MADPET-II	8×4	LSO	2×2×6/8	2.3	22	1.1	-
HIDAC	-	-	-	-	-	1.2 (1.2)	0.9

## 2.2.2 Designs with depth-of-interaction determination

### Phoswich

The scintillator pixels in phoswich detectors are divided into multiple layers of different scintillator materials (see figure 2.3(a)). The materials need to be chosen in such a way, that the light of the top layers can pass through the bottom layers, and that the properties of the light pulses coming from the materials are sufficiently different, so that the layer in which the interaction took place can be determined from the shape of the light pulse. Usually the decay time of the light pulse is used to determine the layer. For example, the ClearPET (see 2.2.1) uses a layer LSO on top of a layer LuYAP [58]. Other options that were investigated are LSO and LYSO [63], LSO, GSO and BGO [69], and three layers of GSO with different cerium concentrations [84].

Using phoswich the DOI resolution can be improved by only a factor two or three. However, this can already give a substantial improvement of the uniformity of the spatial resolution. Since (1) the amount of light coming from the different layers will usually differ, and (2) the pulse shapes will also differ (phoswich would not work otherwise), the electronic processing of the pulses is more difficult.

### Variation of light yield

This method is somewhat similar to the phoswich method. In this case, the amount of light reaching the light detector depends on the distance of the interaction from the light detector. For example, R. MacDonald et al. [46, 45] use 4 layers of the same crystal. Because of the optical coupling between the layers the fraction of light reaching the detector depends on the layer. It is also possible to treat the surface of the crystal pixels [52, 56]. A big disadvantage of this method is that it depends on light loss, while one would like to collect all of the light in order to get a good timing and energy resolution.

### Double-sided readout

By using two light detectors to read out the scintillator pixels on both ends, the scintillation light is divided over the two light detectors (see figure 2.3(b)). When the surfaces of the pixels are correctly treated [71], the amount of light reaching each side depends on the depth of the interaction inside the crystal. The ratio

$$R = \frac{N_1 - N_2}{N_1 + N_2},$$

where  $N_1$  and  $N_2$  are the amount of light detected by the front and back detector, can be used to determine the depth (large values are close to the top, small values close to the bottom).

This type of detector can give continuous information on the DOI and several groups are investigating this type of design [21, 26, 28, 27, 29]. It is also possible to put the pixels in axial direction instead of the radial direction [9]. The depth inside the crystal then gives the radial coordinate and the pixel determines the tangential coordinate.

### Light sharing

By sharing the light between pixels in the top part of the detector and not in the bottom part of the detector, there will be multiple pixels giving a signal when the event occurred in the top part of the detector and only one pixel giving a signal when the event occurred in the bottom part of the detector. One way of doing this is to have two layers of crystals, where the top layer is shifted half a layer with respect to the bottom layer [23] (see figure 2.3(c)). The same effect can also be achieved by sawing the top part of a monolithic block into pixels and doing the same for the bottom part with half a pixel shift [85]. An other method is by partially leaving away the reflectors that are usually around the pixels [53] (see figure 2.3(d)). By doing this in two directions, it is possible to separate four layers [60, 62, 78, 86].

### Other designs

T. A. DeVol et al. [20] investigated a design similar to double sided readout. However, the second detector was not attached to the front of the detector but to the side of the detector. S. McCallum [48] et al. use multiple layers of LSO slices with position sensitive photo-diodes sandwiched in between. This DOI method looks like the method that is used in the MADPET (see 2.2.1), where two layers of detectors are used.

## 2.3 Monolithic scintillation detectors

### 2.3.1 Introduction

All scintillation detectors discussed above use small scintillation crystals. In these designs, the interaction position of a gamma photon is determined by finding the crystal in which the interaction took place. The spatial resolution of these detectors is therefore determined largely by the size of the crystals and can in principle be improved by decreasing the size of the crystals. However, this is limited: when the crystal size is decreased the probability of having interactions in multiple crystals from one gamma photon increases, and the amount of dead space between the crystals needed to optically separate the crystals increases. For example, in the ClearPET and MADPET-II detectors approximately 15% of the detector volume does not consist of scintillating material; for the MicroPET Focus this still is approximately 9%.

An alternative to designs based on arrays of small crystals, are monolithic scintillation detectors. These detectors consist of a relatively large scintillation crystal coupled to one or more position sensitive light detectors. The interaction position of a gamma photon is determined from the distribution of the scintillation light over the light detectors. Since the dead space is minimized in this design the sensitivity can be much higher. The shape of the light distribution can also give information about the depth at which the interaction occurred. Therefore, this design can correct for the DOI.

In the design investigated in this work the light detector is a position sensitive APD array. This has the advantage over position sensitive PMTs (PS-PMTs) that

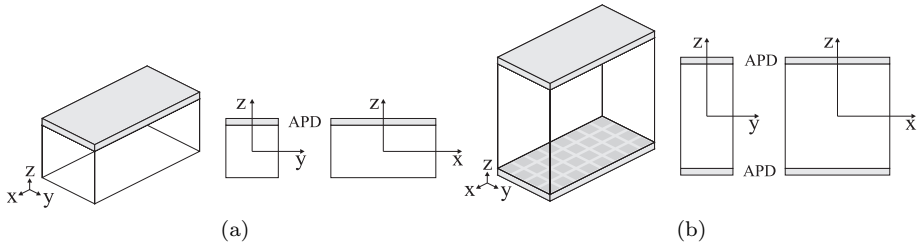


FIGURE 2.4: Two examples of monolithic scintillation detectors. The photons enter the detector from the top. Left a  $20 \times 10 \times 10 \text{ mm}^3$  LYSO crystal read out by a Hamamatsu S8550 APD array that is attached to the side at which the beam enters the crystal, and right a  $20 \times 10 \times 20 \text{ mm}^3$  LYSO crystal read out by two APD arrays.

the space between the detector modules in the detector ring can be very small since the detectors can be much more compact, thereby increasing the sensitivity of the scanner. Furthermore, the gain uniformity of the APD arrays is much better than that of PS-PMTs, where there can be gain differences in the order of a factor two or more. The APD array that will be focussed upon is the S8550 array from Hamamatsu.

The scintillators investigated in this work are LSO and LYSO. The properties of the two are practically equal. These scintillators have good light yield, with a high density allowing for high sensitivity, and they are not hygroscopic.

Figure 2.4 shows the two main designs investigated in this work.

### 2.3.2 Position estimation

A disadvantage of this type of detector is that the position estimation is much more complex than in designs based on small scintillator crystals. In designs based on an array of small crystals the position is determined simply by the identification (id) of the crystal in which the interaction occurs. In monolithic scintillation detectors the position needs to be estimated from the light distribution. In theory it might be possible to derive a function that describes the light distribution as a function of the interaction position. However, in practice there will always be differences between detectors, e.g. the light yield of scintillators vary from crystal to crystal, the gains of the amplifiers are not uniform. Furthermore, because of Compton scatter, fluorescence, etc., the annihilation photon does not interact in one point inside the crystal but interacts in multiple points. The energy of the photon is therefore not deposited in one point of which we might estimate the position but in multiple areas (see chapter 5 for the influence this has on the spatial resolution). Therefore, in practice it will be very difficult to build a model that can predict the interaction position(s) from the measured light distribution.

As an alternative, we use an estimation algorithm that is trained with measured light distributions. During training the algorithm is fed with a large number

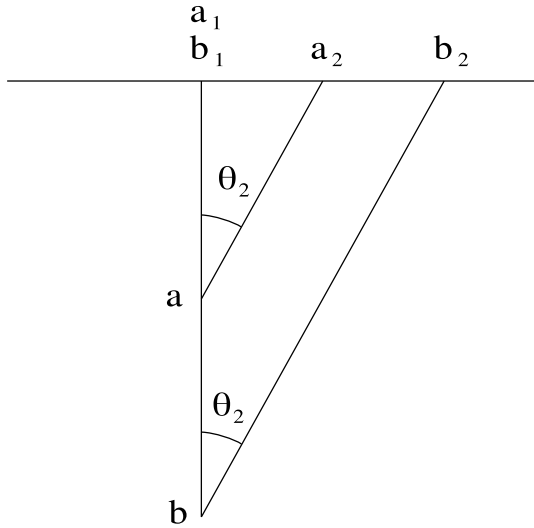


FIGURE 2.5: *The DOI correction: the entry point of an annihilation photon absorbed at  $a$ , is estimated either at  $a_1$  or  $a_2$  depending on the incident angle  $\theta_1 = 0$  or  $\theta_2$ . Likewise for  $b$ .*

of light distributions of which the entry point is known. When the algorithm is trained, it can estimate the entry point of a light distribution of which the entry point is unknown. Since each detector is trained, this algorithm is robust to differences between different detectors. It does not depend on possible incorrect a priori assumptions.

The training is performed by scanning a beam of 511 keV photons in small steps over the detector and collecting a large number of light distributions at every beam position. Since only the  $x$  and  $y$ -coordinate (see figure 2.4) of the entry point of the beam is known, the estimation algorithm can only estimate the entry point. However, by using a separately trained algorithm for different incident angles, the algorithm can still correct for the DOI. When an event is detected, the incident angle of the annihilation photon is estimated from the position of the detector that has detected the second annihilation photon. This angle is then used to select the trained algorithm. The entry point is then estimated using this algorithm. If necessary, this entry point can then be used to obtain a better estimate of the incident angle after which the entry point is re-estimated.

Figure 2.5 illustrates how the DOI correction works. Suppose we have an annihilation photon that is absorbed at  $a$  and one that is absorbed at  $b$ . Since point  $a$  has a different distance to the APD array than  $b$  the light distribution belonging to  $a$  is different to that belonging to  $b$ . The estimation algorithm can therefore distinguish between the two. When the incident angle is 0, the estimation algorithm will estimate  $a_1$  and  $b_1$  as entry points. When the incident angle is  $\theta_2$ , the algorithm will also use training data with this incident angle.

Therefore, the algorithm will estimate entry points  $a_2$  and  $b_2$ .

Different possibilities exist for the algorithm to use. An early design using monolithic scintillator detectors for PET used neural networks (NN) [19]. This is a very practical solution, since NN are fast. However, for the research we are performing, NN have disadvantages. First, since there are a lot of design parameters, the performance of NN tends to depend somewhat on the experience of the person implementing the NN. Second, it is not easy to determine in individual cases why NN made a certain decision. We wanted a method of which the decision making process is easier to follow.

The algorithm that is used in this work is the  $L$  nearest neighbour algorithm. The training data (light distributions with their entry points) is stored in memory. A light distribution of which the entry point needs to be estimated is compared in a least squares sense to all distributions in the training set. The  $L$  distributions in the training set that have the smallest least squares value are selected. The entry point coordinate occurs most frequently among these  $L$  distributions is used as an estimator for the entry point of the light distribution of which the entry point needed to be estimated. In case there are multiple entry points that are most frequent, the one with the smallest least squares value is chosen [83].

In case the number of light distributions in the training set ( $N$ ) goes to infinity and  $L$  also goes to infinity with  $L/N \rightarrow 0$  it can be shown that this algorithm gives optimal results [83].

---

## Optical simulation of monolithic scintillator detectors using GATE/GEANT4<sup>1</sup>

---

**Much research is being conducted on position-sensitive scintillation detectors for medical imaging, particularly for emission tomography. Monte Carlo simulations play an essential role in many of these research activities. As the scintillation process, the transport of scintillation photons through the crystal(s), as well as the conversion of these photons into electronic signals have a major influence on the detector performance, all of these processes generally need to be incorporated in the model to obtain accurate results. In this work the optical and scintillation models of the GEANT4 simulation toolkit are validated by comparing simulations and measurements on monolithic scintillator detectors for high resolution positron emission tomography (PET). We have furthermore made the GEANT4 optical models available within the user-friendly GATE simulation platform. This work demonstrates the use of these models and shows how the necessary optical input parameters can be determined with sufficient accuracy. The results show that the optical physics models of GATE/GEANT4 enable accurate prediction of the spatial and energy resolution of monolithic scintillator PET detectors.**

### 3.1 Introduction

Much research is being conducted on position-sensitive scintillation detectors for medical imaging, particularly for emission tomography [38]. Typical research objectives include improving the performance of existing imaging modalities such as single-photon emission computed tomography (SPECT) and positron emission tomography (PET), developing novel devices for specific applications (e.g.

---

<sup>1</sup>This chapter has been submitted to Physics in Medicine and Biology as: D. J. van der Laan, D. R. Schaart, M. C. Maas, F. J. Beekman, P. Bruyndonckx, and C. W. E. van Eijk, ‘Optical simulation of monolithic scintillator detectors using GATE/GEANT4’.

small-animal tomographs) [77, 49, 88, 68, 14], and/or developing hybrid imaging modalities such as PET/MRI [12, 33, 70].

Monte Carlo simulations play an essential role in many of these research activities. In such simulations many design parameters can be varied much more easily than in measurements. Moreover, simulations can allow one to perform ‘experiments’ that would be impossible in reality. Thus, Monte Carlo simulations are very helpful to better understand the factors that determine detector performance, making optimization of the detector design more efficient.

Optical photons can be seen as the primary information carriers in any position sensitive scintillation detector: the scintillation process, the transport of the scintillation photons through the crystal(s) towards the light sensor(s), and the conversion of these photons into electronic signals all have a major influence on the detector performance. Thus, all of these physical processes generally need to be taken into account in a Monte Carlo model in order to obtain accurate results.

Recently the GATE Monte-Carlo simulation platform [30], which makes a wide range of GEANT4 [5] physics models available through a user-friendly, scripted interface, has come into widespread use in the field of nuclear medicine for simulating PET and SPECT devices. GEANT4 includes models for scintillation and optical transport processes that have been derived from DETECT2000 [37]. Up to now, these models were not available in GATE.

The objectives of the present work are threefold. A first aim is to validate the use of GEANT4 optical models for simulating position-sensitive scintillation detectors, through comparison of simulation and measurement. As a second objective, we have made the GEANT4 optical and scintillation models available within GATE. The third goal is to demonstrate the use of these optical models and to show how the corresponding input parameters can be determined with sufficient accuracy. As the present work was conducted within the scope of a research program on monolithic scintillator detectors for high resolution PET [11, 43], we develop a detailed Monte Carlo model of these detectors and compare the predicted spatial and energy resolutions to experimental results.

## 3.2 Methods and materials

### 3.2.1 Description of the PET detector

The design and operating principle of the monolithic PET detectors investigated in this work have been described in detail elsewhere [44, 40]. Here, we briefly summarize the features relevant for the present study.

Two detector geometries have been investigated. Figure 3.1a shows one of the detectors, consisting of a 20 mm × 10 mm × 10 mm LYSO:Ce crystal (Crystal Photonics) read out by a position-sensitive Hamamatsu S8550SPL APD array optically coupled to the crystal front surface, i.e., the surface at which annihilation photons enter the crystal, by means of Meltmount (Cargille Laboratories, Cedar Grove, NJ, USA). We have shown earlier that this type of detector performs better with the light sensor placed in such front-side readout (FSR) geometry than with conventional back-side readout (BSR), as the majority of the detected annihilation photons interact in the front half of the crystal [43]. The second

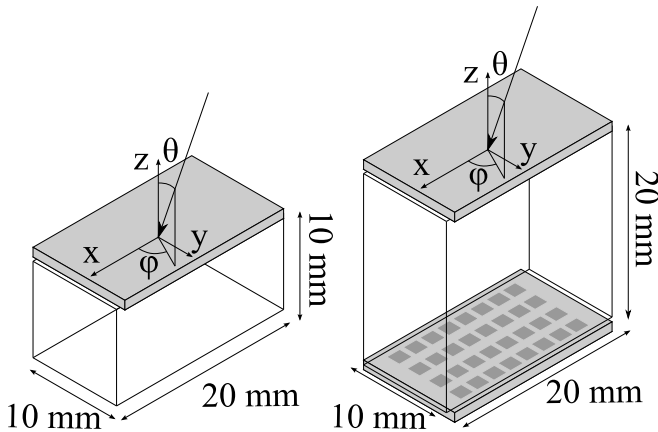


FIGURE 3.1: *Schematic representation of the detectors investigated in this work: (a) a  $20\text{ mm} \times 10\text{ mm} \times 10\text{ mm}$  LYSO:Ce crystal read out by a Hamamatsu S8550SPL APD array on the front surface (FSR geometry), and (b) a  $20\text{ mm} \times 10\text{ mm} \times 20\text{ mm}$  crystal read out on the front and back surfaces (DSR geometry). In both drawings the arrow indicates the path of an annihilation photon incident on the detector front surface. The coordinate system used to specify the entry point and the angle of incidence is also indicated.*

detector is a  $20\text{ mm} \times 10\text{ mm} \times 20\text{ mm}$  LYSO:Ce crystal read out by two APD arrays in double-sided readout (DSR) geometry, see figure 3.1b. Both crystals have optically polished surfaces and are wrapped in highly reflective Teflon tape. The Hamamatsu S8550SPL APD array consists of  $4 \times 8$  pixels, measuring  $1.6\text{ mm} \times 1.6\text{ mm}$  each and spaced  $2.3\text{ mm}$  (center-to-center) apart. The total surface of the APD array measures  $19.5\text{ mm} \times 11.2\text{ mm}$ .

The entry points of detected annihilation photons (‘events’) on the front surface of the crystal are estimated from the measured scintillation light distribution incident on the APD arrays [40]. The position estimation algorithm uses a reference set of light distributions from a large number of events with known entry points. The light distribution of an unknown event is compared using least squares to each of the distributions in the reference set. The  $L$  best fitting distributions (‘nearest neighbours’) are selected and the entry point most frequently occurring among these distribution is assigned to the unknown event.

### 3.2.2 Simulation parameters

Accurate Monte Carlo simulation of a PET scintillation detector requires that all relevant physical processes, such as the interaction of annihilation photons within the crystal, the scintillation process, the transport of scintillation photons to the light sensor, the conversion of the light signals into electronic signals, and the influence of the readout electronics, are properly modelled. In general this requires knowledge of a large number of detector properties that are used as input parameters for the simulation. Some of the parameters needed for the present work

could be obtained from previous studies or from literature, see section 3.1. The remaining optical input parameters were determined experimentally as described in the following.

#### Properties of the scintillator

Measurements were performed on LYSO:Ce crystals from Crystal Photonics. The absolute light yield, i.e., the expectation value of the number of photons emitted per unit energy deposited in the crystal, of a 20 mm  $\times$  10 mm  $\times$  10 mm crystal was determined on a calibrated photo-multiplier tube (PMT) setup, using the method described by J.T.M. de Haas *et al.* [41]. The crystal was irradiated with a  $^{137}\text{Cs}$  source, emitting gamma photons with energy  $E_\gamma = 662$  keV. The intrinsic energy resolution was determined using the same measurement setup by correcting the measured energy resolution  $\Delta E_m/E_m$  for the influences of the excess noise factor and the photon detection efficiency (PDE) of the PMT [22].

The intrinsic emission spectrum of a 20 mm  $\times$  10 mm  $\times$  10 mm crystal was measured in reflection (i.e. the light emission is measured at the irradiated side) using an X-ray tube with a Cu anode operated at 60 kV and 25 mA. The setup used for these measurements has been described by M. D. Birowosuto *et al.* [8].

The optical absorption length  $\lambda_a$  and the optical scattering length  $\lambda_s$  were determined from transmission measurements on a 20 mm thick LYSO:Ce crystal. The measured attenuation length was corrected for reflections at the two crystal-air interfaces. The resulting total bulk attenuation length  $\lambda_{tot}$  can be assumed to be due to (elastic) scattering  $\lambda_s$  and absorption  $\lambda_a$ :

$$\frac{1}{\lambda_{tot}} = \frac{1}{\lambda_s} + \frac{1}{\lambda_a}. \quad (3.1)$$

According to C. Moisan *et al.* [57], it can be assumed that  $\lambda_{tot} = \lambda_s$  at the peak emission wavelength of LYSO:Ce (i.e., at 420 nm). This is equivalent to stating that there are no absorption centres other than  $\text{Ce}^{3+}$  ions within the crystal, as  $\text{Ce}^{3+}$  absorption in LYSO:Ce occurs at wavelengths below about  $\sim 400$  nm only. The measured transmission spectrum indeed appeared to exhibit a horizontal ‘plateau’ at wavelengths  $> 400$  nm. Assuming that  $\lambda_{tot} = \lambda_s$  at each of these wavelengths, a straight line was fitted through this plateau, from which  $\lambda_s$  was derived for all wavelengths between 190 nm and 600 nm (i.e., covering the entire LYSO:Ce emission spectrum). The remaining attenuation at wavelengths  $< 400$  nm was assumed to be entirely due to absorption.

#### Other optical parameters

The relevant optical properties of the active area (pixels) of the S8550SPL APD array could be obtained from literature, see section 3.3.1. However, the reflectance  $r_d$  of the dead area of the APD array could not readily be obtained. Furthermore, different values (ranging from 0.90 to 0.99) are found for the reflectance  $r_{PTFE}$  of the Teflon tape around the crystal [64, 54]. Therefore,  $r_d$  and  $r_{PTFE}$  were determined as follows.

Pulse-height measurements were performed on a polished, trapezoidal LYSO:Ce crystal. The parallel, rectangular top and bottom surfaces of this crystal measure

11.5 mm  $\times$  19.5 mm and 15.4 mm  $\times$  19.5 mm, respectively. The crystal height (distance between top and bottom surfaces) equals 20 mm. A single APD array was optically coupled to the 19.5 mm  $\times$  11.5 mm top surface. The crystal was irradiated with a broad 511 keV photon beam perpendicularly incident on the 15.4 mm  $\times$  19.5 mm bottom surface, and pulse-height spectra were acquired by electronically adding up the signals of the 32 APD pixels. The number of primary electron-hole pairs generated by scintillation photons per event was derived from the position of the photo-peak, using the known gains of the spectroscopic amplifier, the preamplifiers, and the APD array.

The pulse-height measurements, with and without Teflon tape wrapped around the crystal, were replicated in simulations of the same detector geometry in which the values of  $r_d$  and  $r_{PTFE}$  were varied until the same electron-hole pair yield was obtained.

In order to reduce the dependencies between the validation measurements and the determination of the optical parameters, a different crystal shape and read out scheme was used during the determination of the optical parameters.

### 3.2.3 Spatial resolution measurements

The spatial resolution of the detectors was measured as described below in order to compare the results with those obtained from simulation.

#### Setup

The setup used for the position resolution measurements has been described in detail elsewhere [44]. Here, we only summarize the essential features.

The detectors are contained in a light-tight, temperature-controlled box, placed on a computer-controlled XZ $\Omega$ -stage for translating and rotating the detector. A thin ( $<1$  mm diameter) test beam of 511 keV photons is defined by placing the detector under study in coincidence with a second detector, consisting of a  $\varnothing$  19 mm  $\times$  35 mm BGO crystal mounted on a PMT, placed behind a 60 mm thick lead collimator with a  $\varnothing$  5 mm opening. A  $\varnothing$  0.5 mm  $^{22}\text{Na}$  point source is placed in between the two detectors. The distance  $l_{LYSO}$  between the source and the LYSO:Ce crystal and the distance  $l_{BGO}$  between the source and the BGO crystal together determine the beam diameter.

The 32 signals of each APD array are pre-amplified by Cremat CR-110 charge-sensitive preamplifiers. Further amplification and shaping is provided by CAEN N568BB 16-channel spectroscopy amplifiers, which are read out by 32-channel peak-sensing ADCs (CAEN V785).

#### Test beam profile

Spatial resolution measurements performed in the above setup are affected by the finite diameter of the 511 keV photon beam[40, 39]<sup>2</sup>. To accurately simulate the experiments, the beam intensity profile must therefore be incorporated in

---

<sup>2</sup>[39] corresponds to chapter 5 in this thesis.

the model. This is not trivial as the beam profile is determined by many factors and, since the beam diverges, the FWHM of the beam profile increases by approximately 20% over 20 mm.

The beam intensity profile has been determined via detailed Monte Carlo simulations of the measurement setup, taking into account the geometry of the detectors, collimator and  $^{22}\text{Na}$  source, the positron range, and the acollinearity of the annihilation photons emitted. The simulation was performed using both GEANT4 [5] and GATE [30]. Further information on these simulations and the experimental validation of the results are given elsewhere [39]<sup>3</sup>. As in that work, we will characterize the beam diameter  $d_{beam}$  as the full width at half maximum (FWHM) of the cross-sectional beam intensity profile at the crystal front surface.

## Measurements

Spatial resolution measurements were performed by first recording a number of  $n_{ref} = 1500$  reference events at each of a linear array of beam positions spaced 0.25 mm apart along the x-axis of the detector (see figure 1 for the definition of the coordinates). To determine the (one-dimensional) detector spatial response, the entry point of each light distribution in the resulting data set was determined with the position estimation algorithm described in section 2.1, using the remainder of the events as reference data (leave-one-out approach) and taking only the x-coordinate into consideration. The normalized histogram of the differences between the estimated entry point and the beam position was then determined. It is to be noted that this histogram still includes the influence of the test beam diameter  $d_{beam}$  (see section 3.2.3).

### 3.2.4 Monte Carlo simulations

As stated in the introduction, this work aimed to validate the GEANT4 optical and scintillation models and to make these models available in GATE. To this end, simulations have been performed using version 4.8.2 of GEANT4. The required functionality to perform these simulations via the user-friendly, scripted user interface of GATE has been added to version 3.0 of the latter code. The relevant GEANT4 settings are described below.

The following physics processes were used [2, 1]: G4LowEnergyCompton, G4LowEnergyRayleigh, G4LowEnergyPhoto-Electric, G4MultipleScattering, G4eIonisation, G4eBremsstrahlung, G4OpScintillation, G4OpAbsorption, and G4OpBoundaryProcess, G4OpRayleigh. Here, processes starting with ‘G4Op’ involve optical photons, those starting with ‘G4e’ and G4MultipleScattering involve electrons, while the remaining three processes involve photons with ionizing energies.

The following data libraries were used: G4EMLOW 4.2 (i.e. the low-energy electromagnetic (EM) package, containing data files for EM processes down to about  $\sim 250$  eV), and G4RadioactiveDecay 3.1 (i.e. decay of unstable isotopes). For the transport of electrons we used a range cut of 0.1 mm. This range cut is

---

<sup>3</sup>See chapter 5 of this thesis.

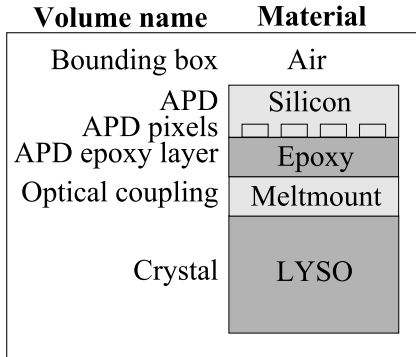


FIGURE 3.2: *Schematic representation of the simulated geometry of the 20 mm  $\times$  10 mm  $\times$  10 mm LYSO:Ce crystal read out by one Hamamatsu S8550SPL APD array on the front surface. Dimensions are not to scale.*

translated into an energy cut for each material based on the density, the effective atomic number, etc.

Figure 3.2 shows a schematic cross-section of one of the simulated detectors. From top to bottom, we have the APD array, the epoxy coating of the APD array, the Meltmount used to optically couple the APD to the crystal, and the LYSO crystal. In the detector with two APD arrays in DSR geometry, this is followed by another layer of Meltmount, epoxy, etc. The entire detector is contained within an air volume. Some elementary properties of the different materials are given in table 3.1. It is noted that the density and chemical composition of the thin Epoxy and Meltmount layers are approximate, as they do not significantly influence the present simulations.

We use the UNIFIED model in GEANT4 for modelling the reflection of photons at surfaces between two dielectric materials [61, 37, 1]. Different types of surfaces are available, but we only use ground and ground-back-painted in this work. Other types, such as polished surfaces, can be seen as special cases of these. A ground surface is assumed to consist of small micro facets, whose normals have small angles relative to the average surface normal. The distribution of these angles is assumed to be Gaussian with mean 0 and standard deviation  $\sigma_\alpha$ . This is illustrated in figure 3.3. For example, a ground surface with  $\sigma_\alpha$  equal to 0 is equivalent to a perfectly polished surface. The probability of reflection and the angles of reflection and refraction follow from the direction of the photon, the angle of the micro facet surface normal, and the refractive indices of the two materials involved. The photon is therefore either reflected back into the original volume or refracted into the next volume.

In case of the ground-back-painted surface, this next volume is considered to be a paint layer of which the refractive index can be specified in the definition of the surface. The paint layer reflects a specified proportion of the photons, assuming Lambertian reflection. All other photons are absorbed. The reflected photons reach a micro facet where they can again be reflected or refracted. This process is repeated until the photon is either absorbed in the paint layer or

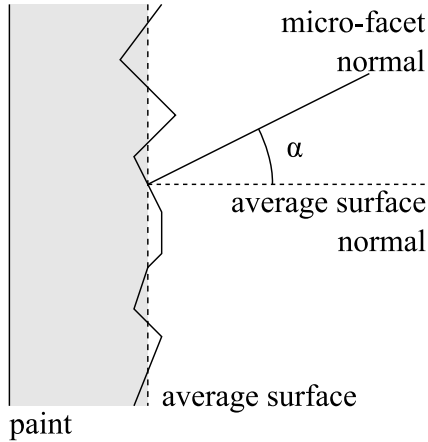


FIGURE 3.3: The UNIFIED model using micro-facets to model the surface roughness. In case of a ground-back-painted surface the outside of the volume is assumed to be covered by a paint layer.

TABLE 3.1: Elementary properties of the materials used in the simulations.

Material	Chemical composition	Density (g/cm <sup>3</sup> )	Refractive index	Ref.
Air	N <sub>0.76</sub> O <sub>0.23</sub> Ar <sub>0.01</sub> C <sub>0.00</sub>	1.29·10 <sup>-3</sup>	1.00	<sup>a</sup>
Silicon	Si <sub>1</sub>	2.33	-	<sup>a</sup>
Epoxy	C <sub>1</sub> H <sub>1</sub> O <sub>1</sub>	1.00	1.52	<sup>b</sup>
Meltmount	C <sub>1</sub> H <sub>1</sub> O <sub>1</sub>	1.00	1.70	<sup>b</sup>
LYSO	Lu <sub>2</sub> Si <sub>1</sub> O <sub>5</sub>	7.40	1.82	[51]

<sup>a</sup> From GATE data-file

<sup>b</sup> Refractive index provided by manufacturer. For chemical composition and density see text.

reflected back into the original volume.

The interface between a dielectric material and a metal is treated somewhat differently [1] from the dielectric-dielectric interface discussed above. As the refractive index is not defined for metals, the probability of reflection has to be specified. This is considered to be specular reflection at the micro-facet. Non-reflected photons are absorbed in the metal.

The type, finish, and value of  $\sigma_\alpha$  of each of the optical interfaces in figure 3.2 are given in table 3.2. Previous simulations have shown that the crystal surface roughness has relatively little influence on the performance of our detectors [79]. It follows that this parameter is not very critical, so we have simply adopted the value of the surface roughness parameter for polished crystal surfaces from Moisan *et al.* [55], viz.  $\sigma_\alpha = 0.1^\circ$ . The same value was used for the epoxy and Meltmount surfaces, while the silicon surfaces of the APD array were assumed to be perfectly flat (i.e.,  $\sigma_\alpha = 0^\circ$ ). Other optical properties of the various materials and surfaces are discussed in section 3.3.1.

TABLE 3.2: *Type and surface finish of each of the optical interfaces defined in the simulations.*

Optical interface	Type	Finish	$\sigma_\alpha$
Air-LYSO	dielectric-dielectric	ground backpainted	0.1
Air-Meltmount/epoxy	dielectric-dielectric	ground backpainted	0.1
Epoxy-APD	dielectric-metal	ground	0
Epoxy-APD	pixels dielectric-metal	ground	0
LYSO-Meltmount	dielectric-dielectric	ground	0.1
Meltmount-epoxy	dielectric-dielectric	ground	0.1

### 3.3 Results and discussion

#### 3.3.1 Simulation parameters

We first discuss the various detector properties needed as input parameters for our simulations. Details of the measurements performed to obtain some of these parameters have been discussed in section 3.2.2.

#### Properties of the scintillator

The parameters needed to accurately model the LYSO:Ce scintillator in GEANT4 [1] are the absolute light yield  $\bar{Y}$ , the FWHM intrinsic energy resolution  $\Delta E/E$ , the emission spectrum, the optical absorption length  $\lambda_a$ , the optical scattering length  $\lambda_s$ , the refractive index  $R_{LYSO}$ , and the surface roughness parameter  $\sigma_\alpha$  that has been explained in section 3.2.4. The values of  $R_{LYSO}$  and  $\sigma_\alpha$  have been given in tables 3.1 and 3.2, respectively.

In GEANT4 the number of scintillation photons  $n_{ph}$  emitted upon absorption of a gamma photon with energy  $E_\gamma$  is sampled from a normal distribution with expectation value  $\bar{n}_{ph} = E_\gamma \bar{Y}$ . Furthermore, the variance in the number of emitted scintillation photons is assumed to be proportional to the amount of energy deposited:

$$\text{var}\{n_{ph}\} = \alpha^2 \bar{n}_{ph} \quad (3.2)$$

with the parameter  $\alpha$  given by

$$\alpha = \frac{\sqrt{\bar{n}_{ph}}}{2.35} \frac{\Delta E}{E}. \quad (3.3)$$

Using the methods discussed in section 3.2.2, we found  $\bar{Y} = 26000$  photons/MeV and  $\alpha = 4.4$  corresponding to an intrinsic energy resolution  $\Delta E/E = 9.0\%$  FWHM at 511 keV.

The solid curve in figure 3.4 shows the LYSO:Ce emission spectrum measured as described in section 3.2.2. The same figure also shows the absorption length (dashed curve) and the scattering length (dashed-dotted curve) that were determined via the method described in the same section.

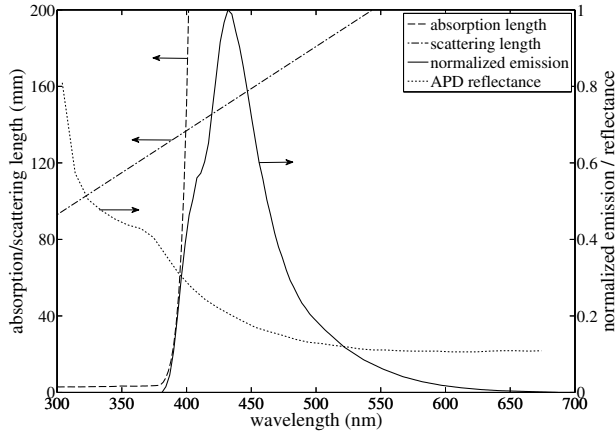


FIGURE 3.4: The LYSO:Ce normalized emission spectrum (solid curve, right  $y$ -axis), optical absorption length  $\lambda_a$  (dashed curve, left  $y$ -axis), scattering length  $\lambda_s$  (dashed-dotted curve, left  $y$ -axis), and the reflectance  $r_a$  of the APD pixels of the Hamamatsu S8550SPL APD array (dotted curve, right  $y$ -axis).

### Properties of the APD array

To model the APD array, we need the refractive index of the epoxy coating  $R_{epoxy}$ , the reflectance  $r_a$  of the active regions of the APD array (i.e., the APD pixels), the reflectance  $r_d$  of the dead area between the pixels, the internal quantum efficiency  $\eta_i$  of the APD pixels (i.e., the probability that absorption of an optical photon results in an electron-hole pair that is amplified), the APD excess noise factor  $J$ , the APD gain  $M$ , and the total equivalent noise charge (ENC) of the detector-amplifier system  $\sigma_e^2$ .

The external quantum efficiency  $\eta_e$  of the pixels of the Hamamatsu S8550SPL APD array has been reported by Mosset *et al.* [59]. As their experiments were performed in air, three factors determine the measured value of  $\eta_e$ , viz.  $\eta_i$ ,  $r_a$ , and the reflection  $r_{epoxy}$  at the epoxy-air interface. Taking first-, second-, and higher-order reflections into consideration, it can be shown that, at perpendicular incidence:

$$\eta_e = \frac{(1 - r_d)(1 - r_{epoxy})}{1 - r_a r_{epoxy}} \eta_i. \quad (3.4)$$

The value of  $r_{epoxy}$  is easily calculated from the refractive index of the epoxy  $R_{epoxy} = 1.52$  (see table 3.1). Reflectance measurements on a variety of photodiodes, which have a similar surface as APDs, showed that the internal quantum efficiency is practically equal to one for wavelengths between 400 nm and 800 nm [24]. Thus, we assume that  $\eta_i = 1$  for the emission wavelengths of LYSO:Ce. The resulting values of  $r_a$  are indicated by the dotted curve in figure 3.4. The parameter  $r_d$  is discussed in the next section.

The APD gain, excess noise factor, and ENC (referred to the input of the preamplifier) were measured to be approximately  $M = 60$ ,  $J = 2$ , and  $\sigma_e = 600$  electrons, respectively [44]. It is noted that the ENC includes contributions of the

APD leakage current and (pre-) amplifier noise. These numbers were used to add noise to the number of electron-hole pairs following from the optical simulations for each APD-pixel, such that the number of electrons  $n_e$  at the output of a pixel is given by

$$n_e = \sum_{i=1} n_{eh} N(M, M^2(J-1)) + N(0, \sigma_e^2), \quad (3.5)$$

where  $N(\mu, \sigma^2)$  is randomly drawn from a normal distribution with mean  $\mu$  and variance  $\sigma^2$ , while  $n_{eh}$  is the number of electron hole pairs generated in the pixel by the event.

### Other optical parameters

The reflectance  $r_d$  of the APD array dead area and the reflectance  $r_{PTFE}$  of the Teflon tape around the crystal were determined by matching optical simulations to pulse-height measurements on a trapezoidal crystal as described in section 3.2.2.

First,  $r_d$  was determined by performing the measurement and the simulations without any Teflon wrapping around the crystal. In the simulations,  $r_d$  was varied from 0.5 to 0.9 in steps of 0.1. Figure 3.5a shows the calculated photo-peak position as a function of  $r_d$ . The measured photo-peak was positioned at 1900 electron-hole pairs, corresponding to  $r_d = 0.8$ .

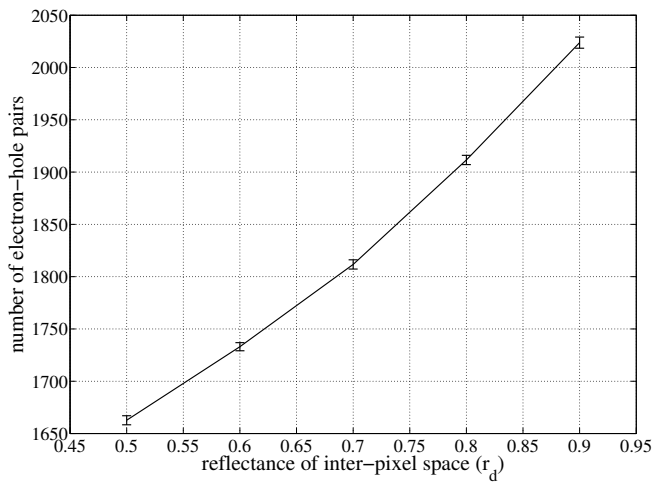
This value of  $r_d$  was subsequently used to determine  $r_{PTFE}$  by repeating the measurement with Teflon tape wrapped around the crystal. In these simulations, the Teflon layer was modelled as a perfectly diffuse reflector [37, 61] with a thin air region between the crystal and the Teflon tape (i.e. we used a back-painted surface with a refractive index of the ‘paint’ of 1, see 3.2.4), and the position of the photo-peak was calculated for different values of  $r_{PTFE}$ . The results are shown in figure 3.5b. The measured photo-peak was positioned at 5300 electron-hole pairs, corresponding to  $r_{PTFE} = 0.95$ .

## 3.3.2 Comparison between simulation and experiment

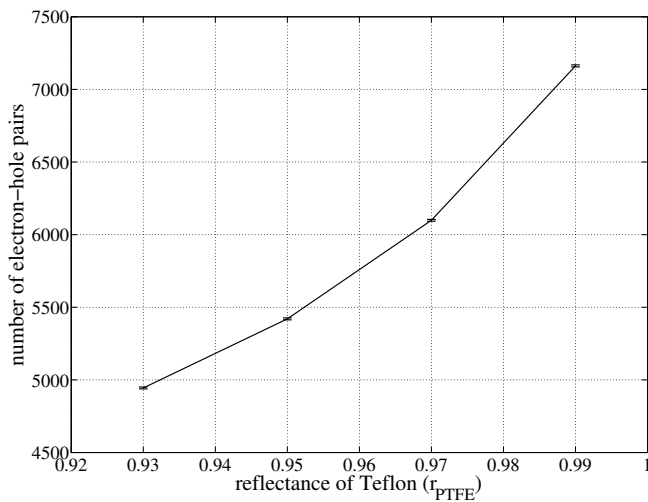
### Detector spatial resolution

Using the input parameters found in section 3.3.1, the spatial resolution measurements discussed in section 3.2.3 were simulated as described in section 3.2.4. It is emphasized that all results presented here include the influence of the finite test beam diameter  $d_{beam} \approx 0.9$  mm FWHM. Furthermore, all results were obtained using  $n_{ref} = 1500$  events per beam position and  $L = 200$  nearest neighbours.

Figure 3.6a shows the measured detector spatial response of the 20 mm  $\times$  10 mm  $\times$  10 mm crystal, averaged over the entire length of the crystal, in comparison to the simulated one. The FWHM and FWTM are equal to 1.66 mm and 4.5 mm, respectively. The corresponding simulated values are 1.67 mm and 4.2 mm, respectively. Taking into account a relative uncertainty of 10% ( $1\sigma$ ) in  $M$ ,  $J$ , and  $\sigma_e$ , the uncertainties in the simulated FWHM and FWTM are estimated to be 0.05 mm ( $1\sigma$ ) and 0.2 mm ( $1\sigma$ ), respectively. Here, the uncertainties due to other parameters were neglected as these are difficult to compute, so these estimates are to be seen as a lower limit on the true uncertainty. Nevertheless,



(a)



(b)

FIGURE 3.5: Simulated position of the photo-peak, (a) as a function of the reflectance  $r_d$  of the dead area between the pixels of the APD array in the absence of any Teflon wrapping, and (b) as a function of the reflectance of the Teflon wrapping  $r_{PTFE}$ , given  $r_d = 0.8$ .

the measured and simulated values agree within the  $2\sigma$  confidence interval of the simulations.

Figure 3.6b shows the measured and simulated spatial responses of the 20 mm  $\times$  10 mm  $\times$  20 mm crystal, both averaged over the entire length of the crystal. The FWHM and FWTM are equal to 1.79 mm and 5.1 mm, respectively. The corresponding simulated values are 1.71 mm and 4.5 mm, respectively. Again the values are in good agreement, although for this crystal the difference between the FWTM values may be significant.

For both crystals, the tails of the measured histograms are slightly higher than those of the simulated ones, which is also apparent from the slightly higher measured FWTM values. This is attributed to scattering of the annihilation photons in materials between the source and the crystal (such as the box containing the detector). In [39]<sup>4</sup> we observed a similar effect.

In previous works it was observed that the spatial resolution of monolithic scintillator detectors is affected near the edges of the crystal [40, 67] aan recent geaccepteerd SiPM artikel (zie bijlage). To investigate if the present simulations correctly reproduce these edge effects, figure 3.7 compares the FWHM of the measured and simulated spatial responses as a function of the  $x$ -position in the crystal, for each of the two detector geometries investigated. These values were obtained from error histograms acquired at 1 mm intervals. The fluctuations in the results are attributed to the relatively small number of events per histogram (approx. 6000 as the step size was 0.25 mm and the number of events per position was 1500). The corresponding uncertainty in the results is in the order of a few tenths of a millimetre. Taking this uncertainty into account, the simulated and measured resolutions are in good agreement.

### Energy resolution

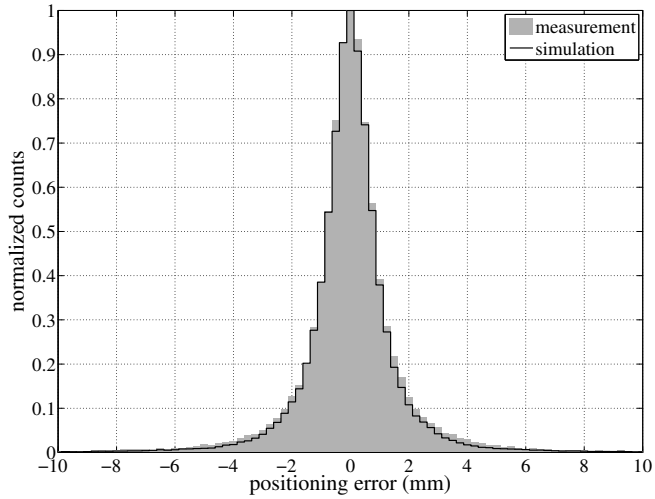
Figure 3.8 shows the pulse-height spectra of the two detectors, determined by adding up the signals of all APD pixels for each event in the reference set. All spectra are normalized such that Gaussians fitted through the photo-peaks are at the same position and have equal heights. For both crystals investigated, the measured and simulated FWHM energy resolutions determined from the Gaussian fits are equal to 10.8% and 10.2%, respectively.

An uncertainty of 10% ( $1\sigma$ ) in the light yield causes an uncertainty of approximately 0.5% ( $1\sigma$ ) in the energy resolution, while an uncertainty of 10% ( $1\sigma$ ) in each of  $M$ ,  $J$ , and  $\sigma_e$  gives rise to an additional uncertainty of approximately 0.15%. Therefore, the measured energy resolutions are well within the confidence intervals of the simulated ones.

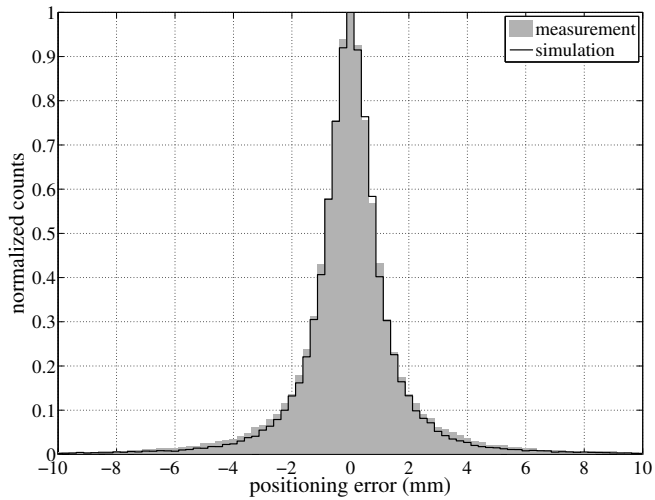
The Compton ridges of the measured energy spectra are slightly higher than those of the simulated energy spectra. This may at least partially be caused by scattering of radiation in materials between the detector and the source. This was also observed in the comparison of the simulated and measured spatial resolutions, see section 3.3.2.

---

<sup>4</sup>See chapter 5 of this thesis.

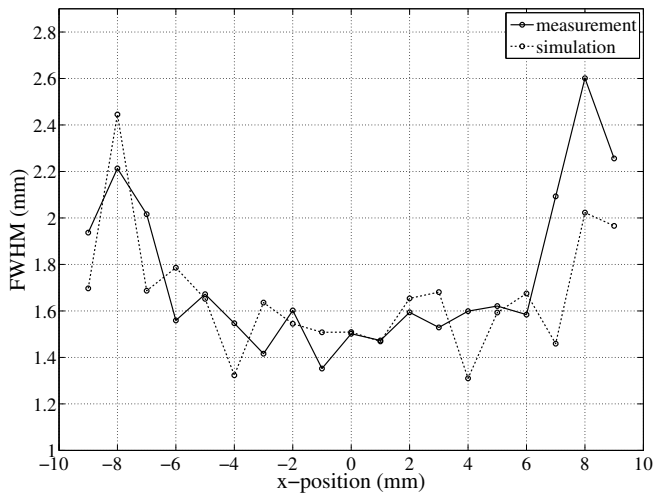


(a)

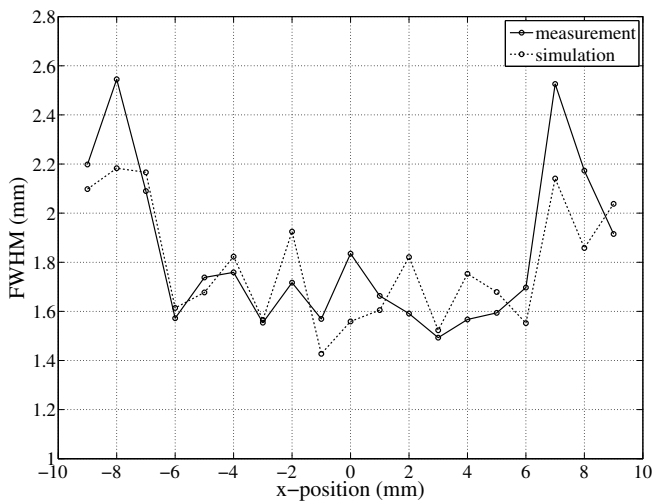


(b)

FIGURE 3.6: Measured and simulated detector spatial response of (a) the  $20\text{ mm} \times 10\text{ mm} \times 10\text{ mm}$  and (b) the  $20\text{ mm} \times 10\text{ mm} \times 20\text{ mm}$  LYSO:Ce crystal, averaged over the entire length of the crystal. Both results were obtained with  $n_{ref} = 1500$  and  $L = 200$  and include the influence of the test beam diameter  $d_{beam} \approx 0.9\text{ mm}$  FWHM.

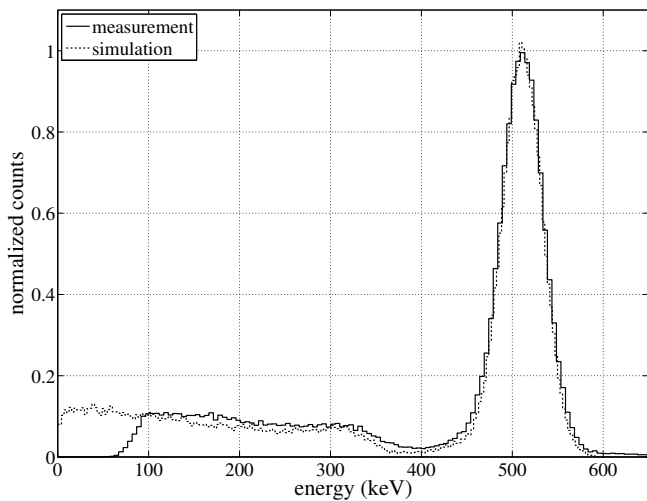


(a)

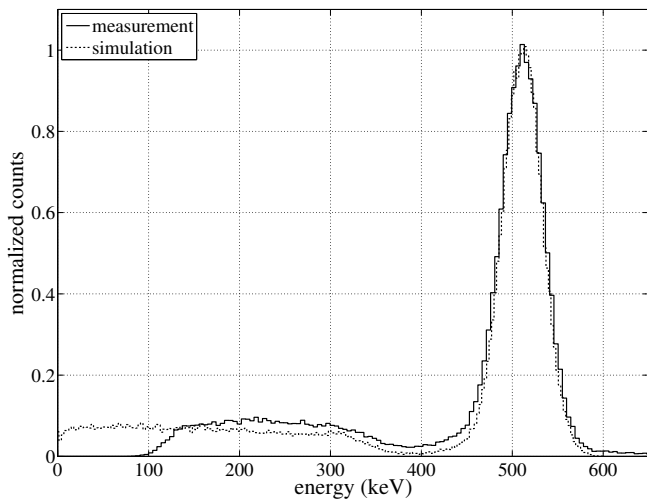


(b)

FIGURE 3.7: The FWHM of the detector spatial response, averaged over 1 mm intervals, as a function of the x-position in the crystal for (a) the 20 mm  $\times$  10 mm  $\times$  10 mm and (b) the 20 mm  $\times$  10 mm  $\times$  20 mm LYSO:Ce crystal.



(a)



(b)

FIGURE 3.8: Measured and simulated pulse-height spectra at 511 keV of (a) the  $20\text{ mm} \times 10\text{ mm} \times 10\text{ mm}$  and (b) the  $20\text{ mm} \times 10\text{ mm} \times 20\text{ mm}$  LYSO:Ce crystal. The measured spectra are electronically cut off below approximately 100–150 keV.

## 3.4 Conclusions

Comparison of simulations and measurements on monolithic scintillator PET detectors shows that the optical physics models of GEANT4 enable accurate prediction of the spatial and energy resolution of such position-sensitive scintillation detectors, provided that all necessary input parameters are known with sufficient accuracy.

As a part of this work, the GEANT4 optical models have been made available within GATE (from version 3.0), so that these routines can now be used for the simulation of e.g. PET and SPECT detectors via GATE's user-friendly, scripted user interface. As optical photons are the primary information carriers in any scintillation detector, this new functionality of GATE may be helpful to many researchers aiming at Monte Carlo aided optimization of existing, and development of new detectors and/or imaging systems.

As illustrated in this work, optical Monte Carlo simulations require accurate knowledge of a relatively large number of input parameters. Not all of these parameters may be readily available. The present work demonstrates how the required optical parameters can be determined such that accurate simulations become possible.



---

### Spatial resolution in position-sensitive scintillation detectors: influence of statistics and noise<sup>1</sup>

---

**We derive the lower bound on the spatial resolution achievable with position-sensitive scintillation detectors. This lower bound depends on the geometry of the detector, the light collection, the light sensor properties, and the readout electronics. The factors that limit the spatial resolution are investigated. The resulting insight in the performance of the detector is useful to optimize its design. Furthermore, the performance of the algorithm used to derive position information from the detector signals can be tested by comparing the measured spatial resolution with the lower bound.**

**Here, we apply the method to monolithic scintillator detectors with depth-of-interaction (DOI) correction for high-resolution positron emission tomography (PET). In these detectors the entry points of annihilation photons on the front surface of the crystal are derived from the scintillation light distributions measured with position-sensitive light sensors.**

**For these detectors, the excess noise factor of the APD array and the light yield of the scintillator contribute most to the measured spatial resolution, while the energy resolution of the scintillator has not influence on the spatial resolution. The position estimation algorithm used in this detector performs very well, since the spatial resolution we obtain using this detector is close to the lower bound.**

**Our method can also be used for other scintillation detectors in which position information is derived from the scintillation light distribution. It can also be adapted to other performance parameters such as timing resolution.**

---

<sup>1</sup>This chapter will be submitted to Physics in Medicine and Biology as: D. J. van der Laan, D. R. Schaart, M. C. Maas, P. Bruyndonckx, F. J. Beekman and C. W. E. van Eijk, ‘Spatial resolution in position-sensitive scintillation detectors: influence of statistics and noise’. The model derived in this chapter is based on a much simpler model derived in [79], which is included in appendix A for reference.

## 4.1 Introduction

Imaging modalities such as computed tomography (CT), planar scintigraphy (PS), single-photon computed tomography (SPECT), and positron emission tomography (PET) utilize X-rays or gamma photons transmitted through or emitted from the subject under study. In most devices, scintillators convert the energy of these ionizing quanta into tiny flashes of light. The data needed for image reconstruction (e.g., position, energy, and time information) are then derived from the electronic signals generated by light sensors optically coupled to the scintillators.

It follows that the detector performance imposes a fundamental limit on the image quality achievable. Therefore, much research is aimed at better scintillation detectors. While in most applications multiple performance parameters are of importance (e.g. energy resolution, time resolution, detection efficiency), one of the most important is the detector intrinsic spatial resolution.

The detector spatial resolution is determined by many factors, such as the detector geometry, information carrier statistics, electronic noise, and the method used to estimate the gamma photon position from the detector signals. To complicate things further, these influences can be interdependent. This makes it difficult to quantify the influences of individual design parameters.

In this work we derive the Cramér-Rao lower bound on the spatial resolution achievable with position-sensitive scintillation detectors. Given a statistical model of the observations (i.e., the detector signals), the Cramér-Rao lower bound equals the smallest value of the standard deviation on the parameter of interest (i.e., the position of the gamma photon) that any unbiased estimator of that parameter can achieve. Here we show how this lower bound can be derived as a function of the relevant detector design parameters.

We can therefore use our model to determine where we can improve our detector design, which, at the same time, leads to a better understanding of the detector. Furthermore, the performance of the position estimation algorithm can be checked, i.e., when the measured spatial resolution is much worse than the lower bound, it can in principle be improved by improving the estimation algorithm. All of this is of value to the development of imaging systems with improved image quality.

This research was performed within the context of the development of monolithic scintillator detectors for PET with intrinsic depth-of-interaction (DOI) correction [40]. The good spatial, energy and time resolutions of these detectors, together with accurate DOI correction and high detection efficiency, facilitate excellent and uniform image quality. In this paper, we will demonstrate our method for such detectors.

Some of the first steps in the development of our method have been reported on earlier [79]. The preliminary, simplified detector model used in that work, in which the detector signals were approximated as mutually independent Poisson distributions, prohibited validation of the results through comparison with measured data. In contrast, we now model the detector signals as a multivariate normal distribution, taking into account the covariance between the signals. The present work is based on a more refined model of the detector geometry and

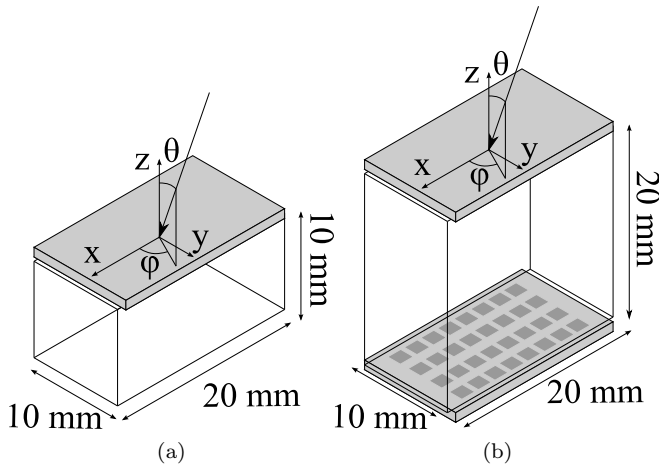


FIGURE 4.1: *Schematic representations of two monolithic scintillation detectors investigated: (a) a  $20 \times 10 \times 10 \text{ mm}^3$  and (b) a  $20 \times 10 \times 20 \text{ mm}^3$   $\text{LYSO}:\text{Ce}^{3+}$  crystal with polished surfaces, clad in Teflon and read out by one or two Hamamatsu S8550SPL APD arrays having  $8 \times 4$  APD pixels each.*

includes a much more detailed, wavelength-dependent model of the generation, transport and detection of the scintillation light that takes into account all relevant optical properties of the crystal and light sensors, as well as the fact that the generation of scintillation photons is not a Poisson process. Furthermore, the quantum efficiency, electron multiplication, and excess noise factor of the APDs, as well as electronic noise, are now taken into account.

In the remainder of this work, we first derive the lower bound on the spatial resolution as a function of the relevant detector properties. Subsequently, the model is used to investigate the relative influence of different design parameters on the detector performance. Finally, we compare the calculated lower bound to the spatial resolution measured with prototype monolithic scintillation detectors.

## 4.2 Theory

We demonstrate our method by analyzing detectors consisting of monolithic  $\text{LYSO}:\text{Ce}^{3+}$  crystals read out by position-sensitive avalanche photodiode (APD) arrays, see Figure 4.1. In these detectors, the entry point of an annihilation photon on the front surface of a monolithic crystal is estimated from the scintillation light distribution measured by the APD arrays.

To derive the lower bound on the spatial resolution, we need the probability distribution of the observations (i.e. the APD array signals) as a function of the parameters to be estimated. We will assume that we have a point source of light at position  $\underline{x} = (x, y, z)^T$  inside the crystal and that we want to estimate the position of that point source. The situation where we have more than one point source for one detected annihilation photon (as e.g. in case of a photo-

effect following Compton scatter), can be approximated by one single average interaction [39]<sup>2</sup>. When we know the probability distribution of the  $N_{apd}$  APD array signals given the position of the point source, the Cramér-Rao lower bound on the variance of the estimated position of the point source can be determined. Hence, in section 4.2.1 we first derive the statistical properties of these signals. In section 4.2.2 we then derive the lower bound.

### 4.2.1 Model of the observations

After absorption of a gamma photon by a scintillator,  $n_{ph}$  optical photons are emitted. The expectation value of  $n_{ph}$  is equal to the product of the light yield of the scintillator and the amount of energy deposited; the variance in  $n_{ph}$  is determined by the intrinsic energy resolution of the scintillator. We express the intrinsic energy resolution as a factor  $\alpha$  times the energy resolution in case the amount of photons emitted would follow a Poisson distribution. Therefore,

$$\text{var}\{n_{ph}\} = \alpha^2 \bar{n}_{ph}. \quad (4.1)$$

Here,  $\alpha > 1$  accounts for the deviation from Poisson statistics of the intrinsic energy resolution and  $\bar{n}_{ph} = \text{E}[n_{ph}]$  is the expectation value of the number of emitted photons  $n_{ph}$ .

Depending on the position  $\underline{x}$  of the light source inside the crystal, a fraction  $f_i(\underline{x})$  of the light emitted will be absorbed by a given APD pixel  $i$ . The remainder of the optical photons is either absorbed by the other  $N_{apd} - 1$  APD pixels or lost due to some other process (e.g. escape, absorption). The  $f_i(\underline{x})$  can be determined by means of Monte Carlo optical simulations, as is explained in more detail in section 4.3.3.

Each photon absorbed in an APD pixel has a chance equal to the internal quantum efficiency  $\varepsilon \leq 1$  to generate an electron-hole pair. Both processes (absorption in a pixel and electron-hole pair generation) are a form of binomial selection. Therefore, the expectation value and the variance in the number of electron-hole pairs created in pixel  $i$  are given by, respectively [7, pp. 642–643],

$$\bar{n}_{eh,i} = \varepsilon f_i(\underline{x}) \bar{n}_{ph}, \quad \text{and} \quad (4.2)$$

$$\text{var}\{n_{eh,i}\} = \varepsilon f_i(\underline{x}) (1 - \varepsilon f_i(\underline{x})) \bar{n}_{ph} + \varepsilon^2 f_i(\underline{x})^2 \text{var}\{n_{ph}\}. \quad (4.3)$$

Each of these primary signals is amplified within the APD in which it is created. One electron-hole pair in pixel  $i$  thus generates  $M$  electrons at the output of the same pixel. However, the amplification  $M$  is not the same for every electron-hole pair. This introduces additional fluctuations. The expectation value and the variance in the total number of electrons at output  $i$  of the APD array are given by, respectively [7, pp. 670–672],

$$\bar{n}_{e,i} = \bar{M} \bar{n}_{eh,i}, \quad \text{and} \quad (4.4)$$

$$\text{var}\{n_{e,i}\} = \bar{M}^2 (J \bar{n}_{eh,i} + \text{var}\{n_{eh,i}\} - \bar{n}_{eh,i}) \quad (4.5)$$

---

<sup>2</sup>See chapter 5 of this thesis.

Here,  $\overline{M}$  is the expectation value of  $M$ , while  $J$  is the excess noise factor defined as

$$J = 1 + \frac{\text{var}\{M\}}{\overline{M}^2} \quad (4.6)$$

In addition to the statistical fluctuations in the number of information carriers, electronic noise also contributes to the variance of the signals. Electronic noise is added both in the APD array itself (dark current) and in the preamplifiers and other electronics used to read out the APD arrays [44]. The sum of the noise contributions can be modelled as additive noise with zero mean and variance  $\sigma_e^2$ . Combining all previous equations, the mean and variance in the observed signals expressed in terms of the number of electrons  $n_i$  at output  $i$  of the APD array, are then given by, respectively,

$$\mu_i \equiv \overline{n}_i = \overline{M}\varepsilon f_i(\underline{x})\overline{n}_{ph}, \quad \text{and} \quad (4.7)$$

$$\sigma_i^2 \equiv \text{var}\{n_i\} = \overline{M}\varepsilon f_i(\underline{x})\overline{n}_{ph} (J + \varepsilon(\alpha^2 - 1)f_i(\underline{x})) + \sigma_e^2, \quad (4.8)$$

where  $\sigma_e^2$  is the equivalent noise charge (ENC) of the detector-amplifier system referred to the preamplifier input.

### 4.2.2 Lower bound for independent detector signals

If  $\hat{\underline{x}} = (\hat{x} + \hat{y} + \hat{z})^T$  are the estimated coordinates of the light source at true position  $\underline{x}$ , the Cramér-Rao inequality for our problem is given by [74]

$$\text{cov}(\hat{\underline{x}}, \hat{\underline{x}}) \geq \mathbf{M}^{-1}, \quad (4.9)$$

where  $\mathbf{M}$  is the Fischer information matrix. This equation shows that the covariance in  $\hat{\underline{x}}$  is always larger than the inverse of the information matrix. Loosely speaking, the more information there is in the observations, the larger the elements of  $\mathbf{M}$  become, and therefore, the more accurately the coordinates of the light source can be estimated. More specifically, the lower bounds on the variances of the estimated coordinates  $\hat{x}$ ,  $\hat{y}$ , and  $\hat{z}$  are given by the diagonal elements of  $\mathbf{M}^{-1}$ .

To derive the information matrix we need a statistical model of the observations (i.e., the number of electrons  $n_i$  at each output of the APD array). In the previous section we already derived expressions for the expectation value  $\mu_i$  and the variance  $\sigma_i^2$  of these observations. Since each  $n_i$  is the sum of a large number of approximately normally distributed variables, it is safe to assume that each  $n_i$  follows a normal distribution. This is confirmed by the fact that the full-energy peak in the measured energy spectra of each of the APD pixels (measured with a LYSO:Ce<sup>3+</sup> crystal on the array, irradiated by a <sup>22</sup>Na source) can be fitted by a Gaussian distribution. The probability density function of each  $n_i$  is then given by

$$p(n_i) = \frac{1}{\sqrt{2\pi}\sigma_i} e^{-\frac{(n_i - \mu_i)^2}{2\sigma_i^2}} \quad (4.10)$$

In first instance, we will simplify the derivation of the lower bound by assuming that the  $N_{apd}$  APD signals are independent of one another. (In the next

section the lower bound will be derived without making this assumption). The information matrix  $\mathbf{M}$  needed to calculate the lower bound can then be written [74]:

$$\mathbf{M} = - \sum_{i=1}^{N_{apd}} \mathbb{E} \left[ \frac{\partial^2 \ln(p(n_i))}{\partial^2 \underline{x}^2} \right] \quad (4.11)$$

Substituting equation (4.10) in equation (4.11), the elements of the information matrix become

$$M_{v,w} = \sum_{i=1}^{N_{apd}} \frac{1}{2\sigma_i^2} \left( \frac{1}{\sigma_i^2} \frac{\partial \sigma_i^2}{\partial v} \frac{\partial \sigma_i^2}{\partial w} + 2 \frac{\partial \mu_i}{\partial v} \frac{\partial \mu_i}{\partial w} \right), \quad (4.12)$$

where  $v$  and  $w$  are equal to  $x$ ,  $y$ , or  $z$ . The partial derivatives in this equation follow from equations (4.7) and (4.8):

$$\frac{\partial \mu_i}{\partial v} = \overline{M} \varepsilon \overline{n}_{ph} \frac{\partial f_i(\underline{x})}{\partial v}, \quad \text{and} \quad (4.13)$$

$$\frac{\partial \sigma_i^2}{\partial v} = \overline{M}^2 \varepsilon \overline{n}_{ph} (J + 2\varepsilon(\alpha^2 - 1)f_i(\underline{x})) \frac{\partial f_i(\underline{x})}{\partial v}, \quad (4.14)$$

with  $v$  equal to  $x$ ,  $y$ , or  $z$ .

By substituting equations (4.13) and (4.14) in equation (4.12), it can be shown that the first term between brackets in equation (4.12) is much smaller than the second if the number of electron-hole pairs in each of the pixels is large enough, i.e., if  $\overline{n}_{eh,i} \gg J + 2\varepsilon(\alpha^2 - 1)f_i(\underline{x})$ . Given equation (4.2), this condition can also be written  $\overline{n}_{ph} \gg 2(\alpha^2 - 1) + J/\varepsilon f_i(\underline{x})$ . In our detector, the number of APD signals  $N_{apd}$  either equals 32 or 64. If we assume that, in first order approximation,  $f_i(\underline{x}) \approx 1/N_{apd} \geq 1/64$  and if we use the measured values of  $\overline{n}_{ph}$ ,  $J$ ,  $\varepsilon$ , and  $\alpha$  given in table 4.1, we see that this condition is easily satisfied in our detectors.

Substituting equations (4.13) and (4.14) in equation (4.12) and neglecting the first term yields

$$M_{v,w} = \sum_{i=1}^{N_{apd}} \frac{\mu_i^2}{\sigma_i^2} \frac{1}{f_i(\underline{x})^2} \frac{\partial f_i(\underline{x})}{\partial v} \frac{\partial f_i(\underline{x})}{\partial w}, \quad \text{for } \overline{n}_{ph} \gg 2(\alpha^2 - 1) + J/\varepsilon f_i(\underline{x}). \quad (4.15)$$

The first factor in the sum,  $\mu_i^2/\sigma_i^2$  is the square of the signal-to-noise ratio of signal  $i$ . The inverse of this factor, the relative variance of signal  $i$ , is given by

$$\frac{\sigma_i^2}{\mu_i^2} = \frac{J}{\varepsilon f_i(\underline{x}) \overline{n}_{ph}} + \frac{\alpha^2 - 1}{\overline{n}_{ph}} + \frac{\sigma_e^2}{(\overline{M} \varepsilon f_i(\underline{x}) \overline{n}_{ph})}. \quad (4.16)$$

Equation (4.15) shows that an increase in the relative variances of the APD signals will increase the lower bound if the light transport inside the detector does not change (i.e., if the  $f_i(\underline{x})$  and their derivatives remain the same). Therefore, the relative signal variances as calculated in equation (4.16) are convenient quantities to use in the analysis of the relative influences of the detector properties  $\overline{n}_{ph}$ ,  $J$ ,  $\varepsilon$ ,  $M$ , and  $\sigma_e$  on the spatial resolution. For a correct investigation of the influence of  $\alpha$  the covariance between the detector signals should be taken into account, as will be done in the next section.

### 4.2.3 Covariance between detector signals

In the previous derivation we assumed that the APD signals are independent of each other. However, since all APD pixels are observing the same light source, any fluctuations in the number of photons emitted by the light source are seen by all of the pixels. This might introduce a positive covariance between the channels. On the other hand, the fact that a photon detected by one APD pixel cannot be detected by any other pixel may introduce a negative covariance.

If the number of photons emitted by the light source follows a Poisson distribution and/or if the fraction of photons detected by each of the pixels is very small, the number of electron-hole pairs in each APD pixel will follow a Poisson distribution and the numbers of electron-hole pairs in the APD pixels become independent of each other [7]. The first condition is not satisfied in scintillation crystals, since the variance in the number of photons emitted is a factor of  $\alpha^2 > 1$  times larger than the value it would have had when it followed a Poisson distribution. For example, for  $\text{LYSO}:\text{Ce}^{3+}$ ,  $\alpha \approx 20$  (see table 4.1). Therefore, we need to investigate if the detection probability is small enough to make the covariance between the APD signals negligible.

The covariance in the number of electron-hole pairs between any arbitrary pair of APD pixels ( $i, j$ ) is given by [7, pp. 646–649]

$$\text{cov}(n_{eh,i}, n_{eh,j}) = \varepsilon f_i(\underline{x}) \bar{n}_{ph} (\delta_{i,j} + \varepsilon(\alpha^2 - 1) f_j(\underline{x})). \quad (4.17)$$

This equation shows that when the source follows a Poisson distribution ( $\alpha = 1$ ), or when the detection probability  $f_i(\underline{x})$  is small, the off-diagonal elements of the matrix disappear, or become small compared to the diagonal elements, respectively. Interestingly, if  $\alpha > 1$ , the fluctuations in the number of photons emitted by the light source dominate, causing a positive covariance between the pixels. On the other hand, if  $\alpha < 1$ , the fact that photons absorbed by one pixel cannot be absorbed by any other pixel dominates, causing a negative covariance between the pixels. Since  $\alpha > 1$  for all known inorganic scintillators, a positive covariance is always to be expected in this type of detector unless  $f_i(\underline{x})$  is small enough for the covariance to be negligible. It can be shown (see appendix B) that the covariance matrix  $\Sigma$  of the APD output signals is given by

$$\Sigma_{i,j} \equiv \text{cov}(n_i, n_j) = \bar{M}^2 \varepsilon f_i(\underline{x}) \bar{n}_{ph} (J \delta_{i,j} + \varepsilon(\alpha^2 - 1) f_j(\underline{x})) + \sigma_e^2 \delta_{i,j}, \quad (4.18)$$

where we used the facts that the amplification process in each APD pixel is independent of those in the other pixels, and that the electronic noise in each read-out channel is independent of those in the other read-out channels.

We assume that the numbers of electrons  $\underline{n} = (n_1, n_2, \dots, n_p)^T$  at the APD array outputs follow a multivariate normal distribution with expectation values  $\underline{\mu} = (\mu_1, \mu_2, \dots, \mu_p)^T$  and covariance matrix  $\Sigma$ , which we have just derived. The information matrix  $\mathbf{M}$  of a multivariate normal distribution is given by [47]

$$M_{v,w} = \frac{\partial \underline{\mu}^T}{\partial v} \Sigma^{-1} \frac{\partial \underline{\mu}}{\partial w} + \frac{1}{2} \text{tr} \left( \Sigma^{-1} \frac{\partial \Sigma}{\partial v} \Sigma^{-1} \frac{\partial \Sigma}{\partial w} \right), \quad (4.19)$$

where  $\text{tr}(\mathbf{A}) \equiv \sum_i A_{i,i}$  is the trace of matrix  $\mathbf{A}$  and the partial derivatives are

given by

$$\frac{\partial \mu}{\partial v} = \overline{M} \varepsilon \overline{n}_{ph} \frac{\partial f}{\partial v} \quad (4.20)$$

and

$$\left( \frac{\partial \Sigma}{\partial v} \right)_{i,j} = \overline{M}^2 \varepsilon \overline{n}_{ph} \left\{ J \frac{\partial f_i(\underline{x})}{\partial v} \delta_{i,j} + \varepsilon (\alpha^2 - 1) \left( \frac{\partial f_i(\underline{x})}{\partial v} f_j(\underline{x}) + f_i(\underline{x}) \frac{\partial f_j(\underline{x})}{\partial v} \right) \right\}, \quad (4.21)$$

where  $\underline{f} = (f_1(\underline{x}) f_2(\underline{x}) \dots f_p(\underline{x}))^T$ .

In order to calculate the information matrix using equation (4.19), the inverse of the covariance matrix,  $\Sigma^{-1}$ , is needed. From equation (4.18) it follows that the covariance matrix can be written

$$\Sigma = \Psi + \overline{M}^2 \varepsilon^2 (\alpha^2 - 1) \overline{n}_{ph} \underline{f} \underline{f}^T, \quad (4.22)$$

where  $\Psi$  is a diagonal matrix, whose elements are given by

$$\Psi_{i,j} = \left( J \overline{M}^2 \varepsilon f_i(\underline{x}) \overline{n}_{ph} + \sigma_e^2 \right) \delta_{i,j}. \quad (4.23)$$

The inverse of equation (4.22) can be calculated using the Woodbury identity [25]:

$$\Sigma^{-1} = \Psi^{-1} - \Psi^{-1} \underline{f} \left( \frac{1}{\overline{M}^2 \varepsilon^2 (\alpha^2 - 1) \overline{n}_{ph}} + \underline{f}^T \Psi^{-1} \underline{f} \right)^{-1} \underline{f}^T \Psi^{-1}. \quad (4.24)$$

The inverse of  $\Psi$  is easily calculated, since  $\Psi$  is a diagonal matrix. Thus, equation (4.24) provides a computationally convenient method for calculating  $\Sigma^{-1}$ , and, therefore, the information matrix  $\mathbf{M}$ .

In section 4.4.3 the influence of the covariance between the channels will be investigated. It will be shown that this influence is small in our detectors.

## 4.3 Materials and methods

### 4.3.1 Detectors

Figure 4.1 schematically shows the two monolithic scintillation detectors studied. The first detector consists of a  $20 \times 10 \times 10 \text{ mm}^3$  LYSO:Ce<sup>3+</sup> crystal with polished surfaces (Crystal Photonics), clad in a Teflon reflector and read out by a Hamamatsu S8550SPL APD array. The Hamamatsu S8550SPL array consists of a  $4 \times 8$  array of  $1.6 \times 1.6 \text{ mm}$  pixels at a pitch of 2.3 mm. The array is optically coupled to the crystal front surface (i.e., the surface that would face the inside of the scanner) using Meltmount (Cargille Laboratories). Front-side readout is made possible by the fact that APD arrays are essentially transparent to 511 keV photons and has been shown in a previous study to provide better results than conventional back-side readout [43].

The second detector, a  $20 \times 10 \times 20 \text{ mm}^3$  LYSO:Ce<sup>3+</sup> crystal read out by two APD arrays, was shown to combine similarly good spatial resolution with increased detection efficiency. Further details on these detectors can be found elsewhere [40, 43].

TABLE 4.1: *Experimentally determined detector properties:  $\bar{n}_{ph}$  is the light yield of the scintillator at 511 keV,  $\alpha$  models the energy resolution of the scintillator,  $\varepsilon$  is the quantum efficiency of the APD pixels,  $\bar{M}$  is the gain of the APD pixels, and  $\sigma_e$  is the standard deviation of the electronic noise in electrons at each APD array output.*

Parameter	$\bar{n}_{ph}$ (ph / 511 keV)	$\alpha$	$\varepsilon$	$\bar{M}$	$J$	$\sigma_e$ (e-)
Value	13286	4.4	1	69	2	600

### 4.3.2 Cramér-Rao model input parameters

The models derived in sections 4.2.2 and 4.2.3 require six detector properties as input parameters:  $\bar{n}_{ph}$ ,  $\alpha$ ,  $\varepsilon$ ,  $\bar{M}$ ,  $J$ , and  $\sigma_e$ . The light yields and energy resolutions of the LYSO:Ce<sup>3+</sup> crystals were measured on a calibrated PMT setup [18]. The internal quantum efficiency  $\varepsilon$  of the APDs is taken as one [24]. The measured external quantum efficiency (approximately 75% at a wavelength of 420 nm [59]) is assumed to be due to reflection of light on the APD pixel, which is included in the simulation. The gain  $\bar{M}$  and excess noise factor  $J$  of the APD array are taken from literature [58, 59]. The ENC has been measured earlier [43]. Table 4.1 provides a summary of these detector properties.

### 4.3.3 Optical simulations

In addition to the above detector properties, the models derived in sections 4.2.2 and 4.2.3 require the fractions of light  $f_i(\underline{x})$  detected by the APD pixels for a light source at  $\underline{x}$ , as well as their partial derivatives. These were obtained from optical Monte Carlo simulations performed with Geant4 [5]. The optical input parameters for these simulations were determined as described in another paper [80]<sup>3</sup>. In that work we also present a validation of our optical simulations against experiment.

In summary, the LYSO:Ce<sup>3+</sup> emission spectrum was measured using the setup described by Birowosuto [8]. The absorption and scattering lengths of LYSO:Ce<sup>3+</sup> were determined as a function of wavelength from the measured transmittance of a 10 mm thick sample. The polished crystal surfaces are modelled as if they consist of micro-facets whose surface normals follow a normal distribution of 0.1° around the average surface normal [55]. The reflectivity of Teflon was taken to be 0.95 [55], that of the APD pixels has been addressed above. The reflectivity of the sensor area between the APD pixels was taken to be 0.8, which yielded best agreement in separate studies in which simulated pulse-height spectra were matched to measured ones for several different geometries [80].

To calculate the fractions  $f_i(\underline{x})$  and their derivatives, a large number of optical photons ( $2 \cdot 10^6$ ) were emitted isotropically from  $\underline{x}$  and tracked until they were absorbed within an APD pixel or elsewhere. This was done for a three-dimensional grid of equidistant point sources within the crystal.

<sup>3</sup>[80] corresponds to chapter 3 of this thesis.

For each point source the fractions  $f_i(\underline{x})$  were determined by dividing the number of photons absorbed in pixel  $i$  by the number of primary photons generated. The partial derivatives were determined by numerical derivation [79]. For example, the partial derivative to  $x$  can be calculated using

$$\left. \frac{\partial f_i(\underline{x})}{\partial x} \right|_{\underline{x}=(x',y',z')} = \frac{f_i(x'+h,y',z') - f_i(x'-h,y',z')}{2h} + O(h^2), \quad (4.25)$$

where  $h$  is the distance between the point sources of light.

The lower bound was subsequently calculated for each point source of light. In all cases, we used the model that includes the influence of the covariance (see section 4.2.3). The spacing  $h$  between the point sources was 0.5 mm in the  $x$ -,  $y$ -, and  $z$ -directions. Given the total number of optical photons in the simulation, this value of  $h$  is a compromise between precision (large  $h$ ) and accuracy (small  $h$ ). The optimum value of  $h$  was determined in preliminary simulations. Since the detectors are symmetric in the  $x$ -,  $y$ -, and, for the 20 mm thick crystal, also the  $z$ -direction, the lower bound only has to be calculated for one quadrant or octant of the crystal.

#### 4.3.4 Comparison with experiment

##### Measurements

To confront our model with experiment, we wish to compare the calculated lower bound to spatial resolution measurements described in detail elsewhere [40]. In these measurements the front surface of a detector is irradiated by a collimated beam of annihilation photons at a rectangular grid of beam positions spaced 250  $\mu\text{m}$  apart. A number of  $n_{ref}$  light distributions are collected at each position.

To determine the spatial resolution of the detector, the entry point of the annihilation photon corresponding to each of the measured light distributions is estimated using the remainder of the distributions as reference data for the position estimation algorithm. The light distribution for which the entry point has to be estimated is compared to each of the distributions in the reference set using least squares. The  $L$  best fitting distributions (nearest neighbours) are selected and the entry point occurring most frequently among these distributions is used as the estimate of the entry point. The point spread function (PSF) of the detector is then calculated as the two-dimensional (2D) histogram of the true minus the estimated entry points. This histogram still contains the influence of the finite beam diameter  $d_{beam}$ , and is therefore referred to as the uncorrected point spread function  $\text{PSF}_u$ .

We studied the influence of various parameters such as electronic noise on the spatial resolution, by varying the parameter of interest in a series of measurements. For efficiency, this was done using a one-dimensional (1D) form of the above experiment, in which reference data were collected along one of the crystal axes and only the coordinate corresponding to that axis was estimated. The 1D histogram of the errors, uncorrected for  $d_{beam}$  and referred to as 1D- $\text{PSF}_u$ , was then derived as a measure of the spatial resolution. All results presented use  $n_{ref}$  equal to 1500.

## PSF model

In section 4.3 we derived the lower bound on the position estimation of a point source of optical photons within the crystal. In contrast, the spatial resolution determined in our measurements includes the influence of the finite diameter of the measurement beam and the influence of Compton scattering and X-ray fluorescence within the crystal. Thus we cannot directly compare the lower bound to the measured resolution. However, in another paper [39]<sup>4</sup> we derived and validated a simple model for the measured PSF that takes into account the effects of the beam diameter, Compton scattering, etc.

The model assumes that, if an annihilation photon undergoes multiple interactions within the crystal, the shape of the resulting scintillation light distribution is the same as if the same total amount of energy is deposited at the energy deposition centroid

$$\underline{x}_c = \frac{\sum_i E_i x_i}{\sum_i E_i} \quad (4.26)$$

where  $E_i$  and  $x_i$  are the energy deposited by, and the position of, the  $i^{\text{th}}$  interaction, respectively.

The spatial probability distribution  $\gamma_b$  of the centroids within the detector is derived from a Monte Carlo simulation of the experimental setup. Then, if the number of distributions in the training set  $n_{ref}$  approaches infinity and the number of nearest neighbours approaches infinity in such a way that  $L/n_{ref}$  approaches zero, the PSF measured with that detector can be described to good approximation by [39]:

$$PSF(\hat{x}_e - \underline{x}_e) = (\gamma_b * N_{\underline{\sigma}})(\hat{x}_e - \underline{x}_e) \quad (4.27)$$

where  $\underline{x}_e$  is the true entry point,  $\hat{x}_e$  is the estimated one, and the operator ‘\*’ denotes a convolution. The function  $N_{\underline{\sigma}}$  accounts for the uncertainty in estimation of the position of the centroid due to statistical fluctuations and noise. It is assumed to be a 2D Gaussian distribution with standard deviations  $\underline{\sigma} = (\sigma_x, \sigma_y)^T$ .

Under the above assumptions,  $N_{\underline{\sigma}}$  models the uncertainty in estimation of the position of a point source of light at the centroid position. Therefore, the lower bound on  $\underline{\sigma}$  is given by  $\underline{\sigma}_{lb} = \sqrt{\text{diag}(\mathbf{M}^{-1})}$ , and substituting  $\underline{\sigma}_{lb}$  in equation (4.27) gives the best possible PSF that can be obtained with the detector. We will denote this result by  $PSF_{lb}$ .

Equation (4.27) is only valid in the centre of the detector [39]. As the PSF of our detectors appears essentially constant over the central region of the detector [40] we have measured the average PSF for entry points with  $-3 \text{ mm} < x < 3 \text{ mm}$  and  $y = 0$  (see figure 4.1). Upon substituting the average values of  $\underline{\sigma}_{lb}$  over  $-3 \text{ mm} < x < 3 \text{ mm}$  and  $-1 \text{ mm} < y < 1 \text{ mm}$  and over  $z$  for  $\underline{\sigma}$  in equation (4.27), the resulting  $PSF_{lb}$  can be compared to the measured  $PSF_u$ .

---

<sup>4</sup>See chapter 5 of this thesis.

## 4.4 Results and discussion

### 4.4.1 Comparison with experiment

#### PSF at detector centre

Figure 4.2 shows the 1D-PSF $_u(x)$  (see section 4.3.4), obtained from measurements on the  $20 \times 10 \times 10 \text{ mm}^3$  and  $20 \times 10 \times 20 \text{ mm}^3$  LYSO:Ce $^{3+}$  crystals (see figure 4.1). The figure also shows the 1D-PSF $_{lb}(x)$  calculated on the basis of the lower bound as described in section 4.3.4. As expected, the 1D-PSF $_{lb}(x)$  is narrower than the 1D-PSF $_u(x)$ . It is interesting to note that the differences are not very large, and that the shapes agree quite well. The 1D-PSF $_u(x)$  has a FWHM of 1.5 and 1.6 mm for the 10 mm thick and 20 mm thick crystals respectively, while that of the 1D-PSF $_{lb}(x)$  equals 1.2 mm for both crystals. Thus, the measured resolution is quite close to the lower bound, suggesting that the estimation algorithm performs quite well.

The PSFs exhibit significant tails. These are due to Compton scattering. Since this part is described mainly by  $\gamma_b$  (see 4.3.4) which is determined from Monte Carlo simulations, and less by  $N_{\underline{\sigma}}$  the agreement between the PSF $_u(x)$  and PSF $_{lb}(x)$  is better in this region.

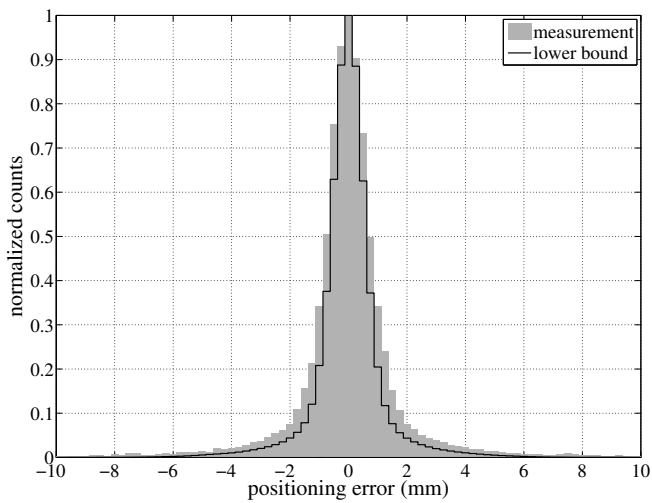
#### Influence of the size of the reference dataset

In order to verify our estimation algorithm and to further validate the calculated lower bound, we increased the number of reference events per beam position  $n_{ref}$ . In figure 4.3, the FWHM of measured 1D-PSF $_u(x)$  (circles) is plotted as a function of the number of reference events per beam position  $n_{ref}$ . As explained in section 4.3.4, 1D measurements were performed for efficiency. Each measured PSF was calculated using the value of  $L$  that minimised its standard deviation, so as to minimise the influence of the positioning algorithm.

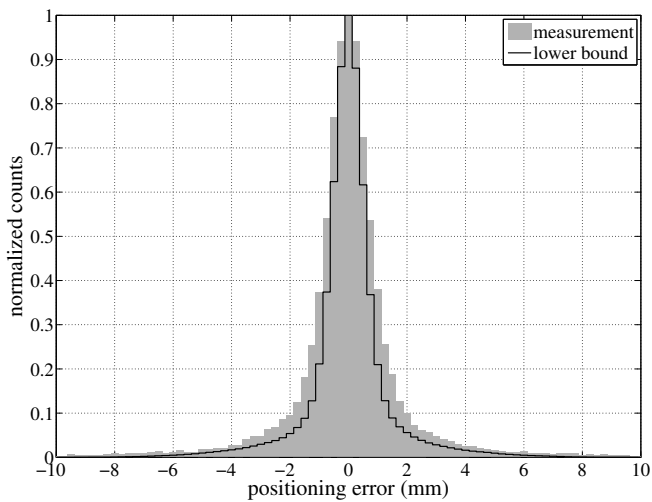
The FWHM of the corresponding 1D-PSF $_{lb}(x)$ , calculated according to section 4.3.4, is indicated by the dashed line. With increasing  $n_{ref}$ , the measured FWHM approaches the calculated lower bound more and more closely, to approximately  $\sim 0.05 \text{ mm}$  at  $n_{ref} = 15000$ . This confirms theory [17], which states that the  $L$ -nearest neighbour algorithm should approach the Cramér-Rao lower bound as  $L \rightarrow \infty$  and  $L/n_{ref} \rightarrow 0$ . Therefore, our estimation algorithm performs well and any deviations from the Cramér-Rao lower bound are caused by the limited size of the reference data set.

#### Influence of noise

As a further test of our model, various amounts of normally distributed noise were added to the measured light distributions and the spatial resolution was determined for each case. Again, 1D experiments were done for efficiency. The symbols in figure 4.4 show the results for the two detectors investigated. The curves in figure 4.4 show the FWHM of 1D-PSF $_{lb}(x)$  calculated as described in section 4.3.4 on the basis of the lower bound, as a function of the electronic noise  $\sigma_e$ . The measured values are always somewhat larger than the lower bound, as



(a)



(b)

FIGURE 4.2: Comparison between the measured  $1D\text{-PSF}_u(x)$  and  $1D\text{-PSF}_{lb}(x)$  based on the Cramér-Rao lower bound, for the  $20 \times 10 \times 10 \text{ mm}^3$  (a) and the  $20 \times 10 \times 20 \text{ mm}^3$  (b)  $\text{LYSO:Ce}^{3+}$  crystal. Measurements were made at the centre of the detector using  $L = 500$ .

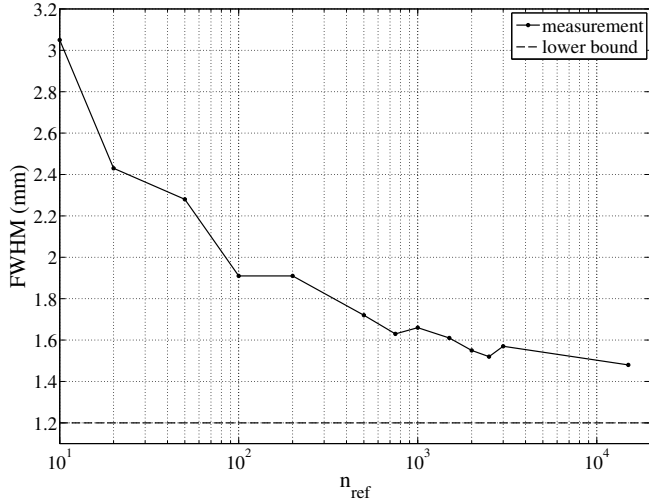


FIGURE 4.3: *FWHM of measured 1D-PSF<sub>u</sub>(x) as a function of  $n_{ref}$  (circles) for the  $20 \times 10 \times 20$  mm<sup>3</sup> LYSO:Ce<sup>3+</sup> crystal. The FWHM of 1D-PSF<sub>lb</sub>(x) based on the Cramér-Rao lower bound is indicated by the dashed line.*

expected. Also, the lower bound correctly predicts that the spatial resolution increases more rapidly with  $\sigma_e$  for the crystal read out by 2 APD arrays than for the crystal read out by 1 APD array. As we will discuss in the next section, this is caused by the large number of pixels in case of readout using 2 APD arrays.

#### 4.4.2 Influence of the detector properties

##### Sensitivity analysis

As was explained in section 4.2.2, one can infer the relative importance of the different detector properties from the relative variances of the detector signals using equation (4.16), provided that the properties determining the transport of light within the detector remain constant. This can e.g. be useful to optimize the design of a scintillation detector, to determine which design parameters are the most important, and to quantify the influence of the various design parameters on the performance.

Lets call the three terms on the right-hand side of equation (4.16) I, II, and III respectively. Term I gives the increase in the relative variance due to the excess noise factor. The excess noise factor  $J$  is always greater than or equal to one. Term II gives the increase of the relative variance due to the fact that the variance in the number of photons emitted by the scintillator per event is larger than that of a Poisson distribution. If the number of optical photons emitted would follow a Poisson distribution (i.e.,  $\alpha = 1$ ), this term would disappear. Term III gives the contribution of electronic noise to the relative variance.

The 10 mm thick and the 20 mm thick crystals are read out by 32 and 64 APD pixels, respectively. Therefore, when the majority of the light is detected,

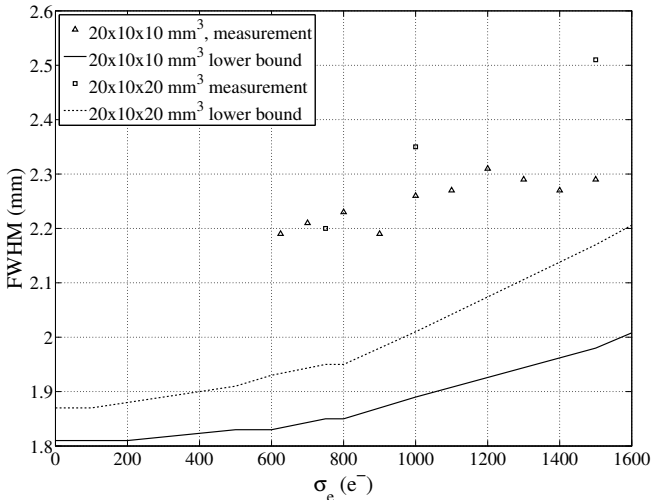


FIGURE 4.4: *The FWHM of the  $1D\text{-PSF}_u(x)$  at the detector centre determined by measurements (symbols) and the  $1D\text{-PSF}_{lb}(x)$  calculated on the basis of the lower bound (curves), as a function of the electronic noise  $\sigma_e$ , for the  $20 \times 10 \times 10 \text{ mm}^3$  and the  $20 \times 10 \times 20 \text{ mm}^3$   $\text{LYSO}:\text{Ce}^{3+}$  crystals, using  $L = 500$ .  $L \rightarrow \infty$  was assumed in the model calculation (equation (4.27)).*

TABLE 4.2: *The average lower bound  $\sigma_{lb}$  and the sensitivity of  $\sigma_{lb}$  to changes in the parameters. The sensitivity is calculated by changing each parameter  $\pm 20\%$  from its nominal value (the nominal values are given in table 4.1).*

	$N_{apd}$	$\sigma_{lb}$ (mm)	Sensitivity of $\sigma_{lb}$ ( $\mu\text{m}/\%$ )				
			$\bar{n}_{ph}$	$\alpha$	$\bar{M}$	$J$	$\sigma_e$
$20 \times 10 \times 10 \text{ mm}^3$	32	0.41	-2.4	0.0	-0.6	1.7	0.6
$20 \times 10 \times 20 \text{ mm}^3$	64	0.34	-2.2	0.0	-0.9	1.3	0.8

$f_i(\underline{x}) \approx 1/32$  or  $f_i(\underline{x}) \approx 1/64$ , respectively. Using these values and the parameter values from table 4.1, the terms I, II, and III can be estimated to be about  $5 \cdot 10^{-3}$ ,  $1 \cdot 10^{-3}$ , and  $4 \cdot 10^{-4}$ , respectively, for the 10 mm thick crystal, and  $1 \cdot 10^{-1}$ ,  $1 \cdot 10^{-3}$ , and  $2 \cdot 10^{-3}$ , respectively, for the 20 mm thick crystal. It thus appears that term I, which accounts for the excess noise factor, is most important for both detectors. As was already observed in section 4.4.1, the 20 mm thick detector is more sensitive to electronic noise than the 10 mm thick detector since it has twice as many APD pixels (64 instead of 32). Finally, the scintillator light yield has a strong influence on the spatial resolution, since it is included in the denominator of all three terms.

Table 4.2 shows the lower bound on the uncertainty in the estimated  $x$ -coordinate averaged over the entire crystal  $\sigma_{lb}$  and the sensitivity thereof to changes in the detector properties, for both of the detector geometries investi-

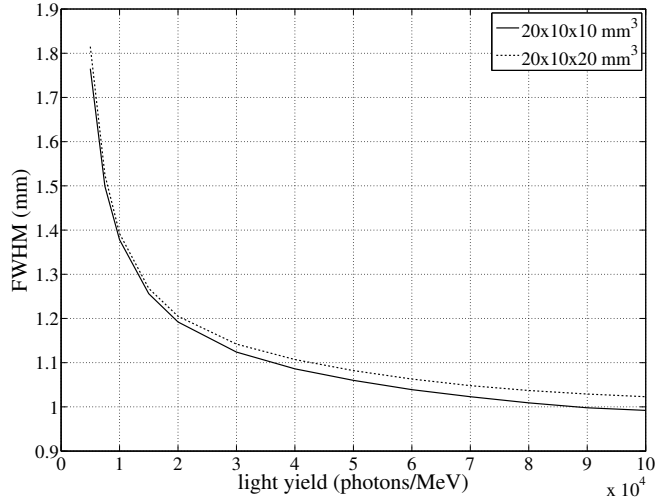


FIGURE 4.5: The FWHM of  $1D\text{-PSF}_{lb}(x)$  as function of light yield (here specified in photons per MeV) for the  $20 \times 10 \times 20 \text{ mm}^3$  and  $20 \times 10 \times 10 \text{ mm}^3$   $\text{LYSO:Ce}^{3+}$  crystal.

gated. The sensitivity was calculated by decreasing and changing the parameter values by  $\pm 20\%$  and dividing the resulting difference in the average lower bound by 40%. Clearly, changes in the light yield and the excess noise factor both have a strong influence on the spatial resolution. In contrast, a change in the energy resolution of the scintillator hardly has any influence.

#### Trend studies

Besides studying the sensitivity of the lower bound to changes of a given detector parameter around its nominal value, we can also use our model to study the variation of the lower bound over a larger range of values of that parameter. Figure 4.4 in the previous section already showed an example of such a study. As further examples, we study here the influence of the two parameters,  $\bar{n}_{ph}$  and  $J$ , that were shown to be most important in the previous section.

Figure 4.5 shows the FWHM of  $1D\text{-PSF}_{lb}(x)$  as a function of the light yield. In the graph we can see the effect of a hypothetical scintillator, which only differs in light yield from  $\text{LYSO:Ce}^{3+}$ . We see that the spatial resolution quickly deteriorates as the light yield decreases from its nominal value of 26,000 photons/MeV. As the light yield increases, the spatial resolution slowly approaches 1 mm FWHM. It should be noted however, that a change in scintillator almost always also means a change in optical transport and thus  $f_i(\underline{x})$  (absorption and emission wavelengths change), energy resolution, and the quantum efficiency of the APD array (caused by the changed emission wavelengths).

Measurements of the light yields of various  $\text{LYSO:Ce}^{3+}$  crystals have shown that the light yield can vary by approximately 20% between different crystals of the same manufacturer [44]. This will lead to differences in resolution between

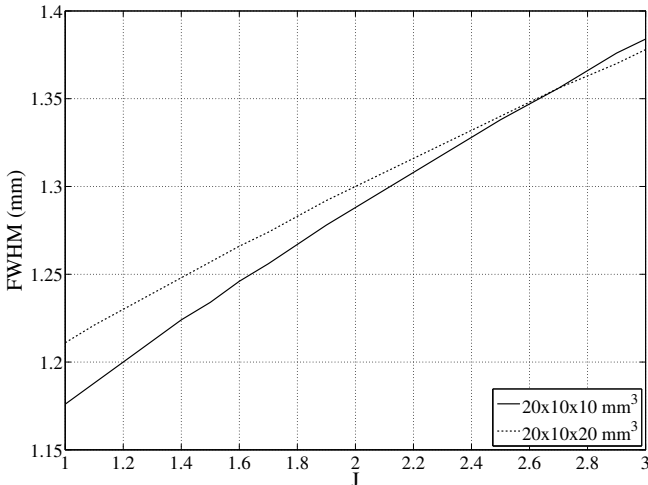


FIGURE 4.6: The FWHM of  $1D\text{-PSF}_{lb}(x)$  as function of excess noise factor  $J$  for the  $20 \times 10 \times 20 \text{ mm}^3$  and  $20 \times 10 \times 10 \text{ mm}^3$   $\text{LYSO:Ce}^{3+}$  crystal.

different detectors in the order of 0.1 mm.

Figure 4.6 shows the FWHM of  $1D\text{-PSF}_{lb}(x)$  as a function of the excess noise factor. Although the excess noise factor is a relatively important contributor to the spatial resolution, the excess noise factor of APDs can not be improved upon much [82]. An improvement of approximately 10% in  $J$  will lead to an improvement of less than 0.05 mm FWHM.

#### 4.4.3 Influence of covariance between detector signals

In section 4.2.3 it was argued that a positive covariance between the detector signals is introduced by the fact that the energy resolution of the scintillator is worse than would be expected on the basis of Poisson statistics. When this covariance between the channels is neglected, we overestimate the influence of the scintillator energy resolution on the spatial resolution of the detector. From equation (4.16) it was argued in section 4.4.2 that the energy resolution has little influence on the spatial resolution. Therefore, we expect the previously calculated lower bounds, that include the covariance, to increase only slightly, when the influence of the covariance is neglected.

To investigate this further, we calculated  $1D\text{-PSF}_{lb}(x)$  (using  $L \rightarrow \infty$ ) for the two detector geometries as a function of  $\alpha$  using the nominal values for the other detector properties (see table 4.1) with and without taking the covariance into account. The results are shown in figure 4.7. At the nominal value of  $\alpha = 4.4$ , we see that the FWHM of  $1D\text{-PSF}_{lb}(x)$  increases from 1.29 mm to 1.32 mm for the 10 mm thick crystal, and from 1.30 mm to 1.31 mm for the 20 mm thick crystal, when neglecting the covariance.

Thus, neglecting the covariance has only a modest influence on the lower bound. Nevertheless, the error in the calculation increases with increasing  $\alpha$ .

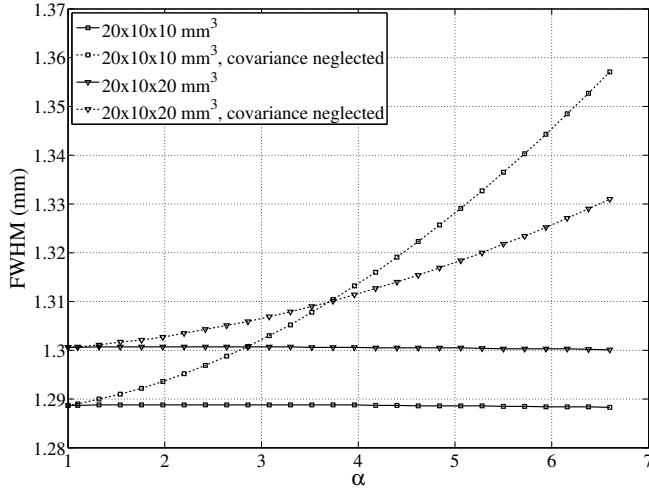


FIGURE 4.7:  $FWHM$  of  $1D-PSF_{lb}(x)$  as a function of  $\alpha$  for  $L \rightarrow \infty$ .

Interestingly, when the covariance is taken into account the value of the intrinsic energy resolution appears to have no effect on the spatial resolution.

## 4.5 Conclusion

In this work we introduce a method to model influences of scintillator properties, scintillation light transport, light sensor properties, photon and charge carrier statistics, and electronic noise on the lower bound on the spatial resolution of position-sensitive scintillation detectors. This model can be used to obtain a better understanding of the performance of a position-sensitive scintillation detector. This makes optimization of the detector design more efficient. Furthermore, the model can be used to predict the best possible performance of the detector. Thus it can be used to determine if a given performance requirement can be met with a given detector. Finally, our model can be used to verify if the algorithm used to estimate the position from the detector signals is performing well.

A comparison of the model to measurements on monolithic scintillation PET detectors shows that our model is capable of explaining the dependence of the spatial resolution on parameters such as light yield end energy resolution of the scintillator, quantum efficiency, gain and excess noise factor of the APD array and electronic noise. As expected, the 1D-PSF as predicted by the model is slightly narrower than the measured one (1.2 mm FWHM versus 1.6 mm FWHM for the  $20 \times 10 \times 20 \text{ mm}^3$  crystal, and 1.2 mm FWHM versus 1.5 mm FWHM for the  $20 \times 10 \times 10 \text{ mm}^3$  crystal). Its shape is consistent with the measured 1D-PSF. The measured spatial resolution appears to be close to the lower bound, which means that the position estimation algorithm used in our detectors is performing well.

The simple expression for the relative variance in the detector signals (equation (4.16)) can be used to investigate the relative influence of the detector prop-

erties on the lower bound. In principle, this equation overestimates the influence of the intrinsic energy resolution of the scintillator, because it does not account for the covariance between the detector signals. However, it was shown that this effect is very small in our detectors. The light yield and the excess noise factor appear to be the most important parameters determining the lower bound in our detectors, followed by the electronic noise and APD gain, whose influences are interdependent.

Perhaps the most important advantage of our method is that it can be used to optimise the spatial resolution of a position-sensitive scintillation detector through a better understanding of its performance. Although we applied it here to a monolithic scintillation detector for PET, our method can also be used, with little to no extra work, for other scintillation detectors that estimate the position of an interaction from the scintillation light distribution. Moreover, our method can also be adapted to other performance parameters. For example, if a model of the pulse shape can be derived, the lower bound on the timing resolution could be derived.



---

## Model analysis of the point spread function of monolithic scintillator PET detectors<sup>1</sup>

---

**We demonstrated previously that monolithic scintillator positron emission tomography (PET) detectors offer the advantages of high spatial resolution, excellent depth-of-interaction (DOI) correction, high detection efficiency, good energy resolution, and simplicity of design. Here we present an analysis of the detector point spread function (PSF) measured with a detector consisting of a monolithic  $\text{LYSO}:\text{Ce}^{3+}$  crystal read out by position-sensitive avalanche photodiode (APD) arrays. A simple model of the detector PSF of monolithic scintillator detectors is derived, which accounts for the spatial distribution of the energy deposited by annihilation photons within the crystal and for the influences of statistical signal fluctuations and electronic noise. A detailed validation of the model is performed through comparison with spatial resolution measurements. The model is shown to describe the measured detector spatial response well at the noise levels found in our experiments. It is furthermore demonstrated how the model can be used to quantify the influence of a finite-diameter test beam of annihilation photons on the measured spatial response, and how a correction for this influence can be made in order to estimate the intrinsic detector PSF.**

### 5.1 Introduction

We demonstrated previously that monolithic scintillator detectors have favourable characteristics for application in positron emission tomography (PET) [40]. They offer the advantages of high spatial resolution, excellent depth-of-interaction (DOI) correction, high detection efficiency, good energy resolution, and simplic-

---

<sup>1</sup>This chapter has been submitted to Medical Physics as: M. C. Maas, D. J. van der Laan, D. R. Schaart, F. J. Beekman, P. Bruijndonckx, Cedric Lamaître and C. W. E. van Eijk, ‘Model Analysis of the Point Spread Function of Monolithic Scintillator PET Detectors’.

ity of design. The detectors consist of a monolithic scintillation crystal coupled to one or more position-sensitive photosensor(s). The entry point of a detected annihilation photon on the front surface of the crystal is derived from the spatial distribution of the scintillation light measured with the photosensor(s). By determining the entry point, the depth-of-interaction is intrinsically corrected for. If solid-state photosensors such as arrays of avalanche photodiodes (APDs) or silicon photomultipliers (SiPMs) [67] are used to read out the crystal, this has the additional advantages that the detector can be made compact and MRI-compatible.

In this work, an analysis of the point spread function (PSF) of monolithic scintillator detectors is presented. To gain an understanding of the factors which determine the PSF, a simple model is derived that accounts for the spatial distribution of the energy depositions following the interaction of an annihilation photon within the scintillator, as well as for the influence of signal fluctuations arising from photon and charge carrier statistics and from electronic noise.

The use of the model is demonstrated by fitting it to the measured spatial response of a prototype monolithic scintillator detector consisting of a LYSO:Ce<sup>3+</sup> crystal and two APD arrays in double-sided readout (DSR) geometry [40]. The model is then used to quantify the effect of the finite diameter of the test beam of annihilation photons on the measured spatial response, and it is shown how a correction for this influence can be made in order to estimate the intrinsic detector PSF. Using the fitting and correction methods thus demonstrated, a detailed validation of the different components of the model is subsequently performed.

## 5.2 Model

### 5.2.1 Detector operating principle

The operating principle of monolithic scintillator detectors has been described in detail elsewhere [40]. In summary, these detectors consist of a monolithic crystal read out by one or more position-sensitive light sensors, see figure 5.1 for an example. Additional details on the detector studied are given in section 5.3.1. The interaction of a 511 keV photon within the detector gives rise to a distribution of scintillation light on the photosensors. The entry point of each detected annihilation photon (‘event’) on the front surface of the crystal is estimated from the measured distribution of the scintillation light. It has been shown before that DOI errors are almost entirely eliminated using this approach [40].

To determine the entry points of unknown events, reference data are first collected by irradiating the detector with 511 keV photons at a grid of known entry points  $\underline{x}_i = (x_i, y_i)$ , and storing the normalized light distributions of  $n_{ref}$  reference events at each  $\underline{x}_i$ . The entry point of an unknown annihilation photon is subsequently estimated by comparing its normalized light distribution with those of all events in the reference set. A subset of the reference data consisting of the  $L$  closest matches (‘nearest neighbours’) is selected, and the most frequently occurring entry point within this subset is assigned to the unknown event.

### 5.2.2 Model of the detector PSF

Upon estimating the entry points of a series of test events using the procedure described in the previous section, a normalized, two-dimensional (2D) histogram of the errors  $\Delta x_i = \hat{x}_j - x_t$  can be created, where  $\hat{x}_j = (\hat{x}_j, \hat{y}_j)$  is the estimated entry point of the  $j$ -th test event recorded at  $x_t = (x_t, y_t)$ . This histogram approaches the point-spread function  $PSF(x, y)$  at  $x_t$  if the number of test events is sufficiently large.

#### Detector PSF

A model of  $PSF(x, y)$  is derived for annihilation photons perpendicularly incident on the detector front surface, see figure 5.1. Three main factors are presumed to contribute to the detector PSF: (1) the spatial distribution of energy depositions within the crystal, (2) photon and electron-hole (e-h) pair statistics and electronic noise in the measured data, and (3) the position estimation algorithm. Each of these contributions is accounted for as described in the following.

An annihilation photon entering the crystal at some entry point  $x_e = (x_e, y_e)$  may give rise to multiple energy depositions, e.g. due to X-rays and Auger electrons following photoelectric absorption, and/or secondary photons and electrons following Compton scattering. For each detected annihilation photon, we define the corresponding energy deposition centroid as the weighted average of these energy depositions. For the present purpose, only the  $x$ - and  $y$ -coordinates  $x_c = (x_c, y_c)$  of this energy deposition centroid are of interest. These are given by:

$$\underline{x}_c = \frac{\sum_n E_n \underline{x}_n}{\sum_n E_n}, \quad (5.1)$$

where  $E_n$  is the energy deposited in the  $n^{\text{th}}$  energy deposition, and  $\underline{x}_n = (x_n, y_n)$  are its  $x$ - and  $y$ -coordinates, respectively. We now define the function  $\gamma_0$  as the probability distribution of  $\underline{x}_c$  for a given  $\underline{x}_e$ :

$$\gamma_0(\underline{x}_c - \underline{x}_e) \equiv \Pr(\underline{x}_c | \underline{x}_e). \quad (5.2)$$

In this work, this distribution is obtained by Monte Carlo simulation.

The following two assumptions are now made. First, it is assumed that the distribution of scintillation light on the photosensor due to an event consisting of multiple energy depositions can be approximated by the light distribution due to a single deposition of the same total energy at the corresponding energy deposition centroid. Second, it is assumed that each centroid position corresponds to a unique expected normalized scintillation light distribution, and, in reverse, that each light distribution corresponds with a unique expected position of the energy deposition centroid.

The light distribution actually measured for a given event may differ from the expected distribution due to statistical signal fluctuations and electronic noise. We will denote the expectation values of the  $x$  and  $y$  coordinates of the energy centroid corresponding with a given, measured light distribution as  $\underline{x}_c' \equiv (x_c', y_c')$ . We now describe the probability distribution of  $\underline{x}_c'$  corresponding to a given  $\underline{x}_c$

by a bivariate normal distribution  $N_\Sigma$  with zero mean and covariance matrix  $\Sigma$ :

$$\Pr(\underline{x}_c' | \underline{x}_c) = N_\Sigma(\underline{x}_c - \underline{x}_c') = \frac{1}{2\pi|\Sigma|^{1/2}} e^{-\frac{1}{2}((\underline{x}_c - \underline{x}_c')\Sigma^{-1}(\underline{x}_c - \underline{x}_c')^T)}, \quad (5.3)$$

where the off-diagonal elements of  $\Sigma$  are assumed to be equal to zero. This distribution is to be seen as a first-order approximation to an unknown underlying distribution, the theoretical determination of which is considered beyond the scope of this work.

The probability that the light distribution actually measured for a given photon entering at  $\underline{x}_e$  corresponds to  $\underline{x}_c'$  can now be written as:

$$\begin{aligned} \Pr(\underline{x}_c' | \underline{x}_e) &= \sum_{x_c} \sum_{y_c} \Pr(\underline{x}_c' | \underline{x}_c) \Pr(\underline{x}_c | \underline{x}_e) \\ &= \sum_{x_c} \sum_{y_c} N_\Sigma(\underline{x}_c' - \underline{x}_c) \gamma_0(\underline{x}_c - \underline{x}_e) = \{N_\Sigma * \gamma_0\}(\underline{x}_c' - \underline{x}_e), \end{aligned} \quad (5.4)$$

where the notation  $f * g(x)$  denotes the convolution of two functions  $f(x)$  and  $g(x)$ , and it is assumed that both  $x_c$  and  $y_c$  have an infinite range.

Based on the measured light distribution with corresponding  $\underline{x}_c'$ , the position estimation algorithm assigns an estimated entry point  $\hat{x}_e$  from the discrete set of reference entry points  $\{\underline{x}_i\}$ , see section 5.2.1. In the following derivation, it is assumed that an equal number of reference events  $n_{ref}$  is recorded at each entry point, so that the total number of events in the reference set equals:

$$N_{ref} = kn_{ref}, \quad (5.5)$$

with  $k$  the total number of reference entry points.

Following the same arguments as above, a reference event recorded at  $\underline{x}_r$  has a probability of generating a light distribution corresponding to  $\underline{x}_c'$  of:

$$\Pr(\underline{x}_c' | \underline{x}_r) = \{N_\Sigma * \gamma_0\}(\underline{x}_c' - \underline{x}_r). \quad (5.6)$$

The probability of misclassification (mispositioning) achieved by the nearest neighbour algorithm generally reaches a minimum at some  $L > 1$ , which depends on  $N_{ref}$ . For the limiting case of  $N_{ref} \rightarrow \infty$ , the optimum is reached for  $L \rightarrow \infty$  with  $L/N_{ref} \rightarrow 0$  [83]. In this case, the algorithm chooses the reference entry point for which the probability density function  $\Pr(\underline{x}_r | \underline{x}_c')$  evaluated at  $\underline{x}_r$  is greatest, since the algorithm selects the most frequently occurring coordinate within the nearest neighbour subset. Assuming that these functions are symmetrical and that the reference entry points lie on a regular, rectangular grid,  $\Pr(\hat{x}_e | \underline{x}_c')$  follows a uniform distribution covering a rectangular area centred around  $\hat{x}_e$ :

$$\begin{aligned} \Pr(\hat{x}_e | \underline{x}_c') &= U\left(x'_c - \frac{\Delta x_r}{2}, x'_c + \frac{\Delta x_r}{2}\right) U\left(y'_c - \frac{\Delta y_r}{2}, y'_c + \frac{\Delta y_r}{2}\right) \\ &= \begin{cases} \frac{1}{\Delta x_r \Delta y_r} & \text{if } -\frac{\Delta x_r}{2} \leq \hat{x}_e - x'_c \leq \frac{\Delta x_r}{2} \wedge -\frac{\Delta y_r}{2} \leq \hat{y}_e - y'_c \leq \frac{\Delta y_r}{2} \\ 0 & \text{elsewhere} \end{cases} \quad (5.7) \\ &\equiv \Upsilon(\hat{x}_e - \underline{x}_c') \end{aligned}$$

where  $\Delta x_r$  and  $\Delta y_r$  represent the distances between adjacent reference entry points in the  $x$ - and  $y$ -directions, respectively. For this case the probability distribution of  $\hat{x}_e$ , given  $\underline{x}_e$ , can be written:

$$\begin{aligned} PSF &\equiv \Pr(\hat{x}_e | \underline{x}_e) = \sum_{x_c} \sum_{y_c} \Pr(\hat{x}_e | \underline{x}_c') \Pr(\underline{x}_c' | \underline{x}_e) \\ &= \{\gamma_0 * N_\Sigma * \Upsilon\}(\hat{x}_e - \underline{x}_e) \quad \text{for } L \rightarrow \infty \wedge L/N_{ref} \rightarrow 0. \end{aligned} \quad (5.8)$$

This equation shows that the influence of  $\gamma_0$  and  $N_\Sigma$  on the PSF only occurs through the test data. According to the arguments that led to equation (5.7), the influence of these factors on the reference data do not affect the PSF, provided that  $L \rightarrow \infty$  and  $L/N_{ref} \rightarrow 0$ . According to equation (5.8), only the pitch of the reference grid may affect the PSF.

### Influence of test beam diameter

The model presented thus far describes the distribution of estimated entry points  $\hat{x}_e$  given a known entry point  $\underline{x}_e$ . In experiments however, the true entry points are known exactly neither in the reference nor in the test data, as the beam of annihilation photons used to record these data sets has a finite diameter. A measured PSF thus actually represents  $\Pr(\hat{x}_b | \underline{x}_b)$ , where  $\underline{x}_b$  represents the true beam position and  $\hat{x}_b$  the estimated one, defining the beam position as the location where the beam axis intersects the crystal front surface. The probability distribution of the  $x$ - and  $y$ -coordinates of the energy centroids due to a realistic experimental beam, having a finite diameter and possibly exhibiting divergence, can again be determined by Monte Carlo simulation and will be written as:

$$\gamma_b(\underline{x}_c - \underline{x}_b) \equiv \Pr(\underline{x}_c | \underline{x}_b), \quad (5.9)$$

where the subscript 'b' is used to indicate the use of a realistic beam. The probability distribution of  $\hat{x}_b$ , given  $\underline{x}_b$ , is then found by substituting  $\gamma_b$  for  $\gamma_0$  in the derivation given in the previous section, yielding:

$$\begin{aligned} PSF_b &\equiv \Pr(\hat{x}_b | \underline{x}_b) \\ &= \{\gamma_b * N_\Sigma * \Upsilon\}(\hat{x}_b - \underline{x}_b) \quad \text{for } L \rightarrow \infty \wedge L/N_{ref} \rightarrow 0. \end{aligned} \quad (5.10)$$

Similar to equation (5.8), the influence of  $\gamma_b$  only occurs through the test data and not through the reference data, provided that  $L \rightarrow \infty$  and  $L/N_{ref} \rightarrow 0$ .

### Background

To account for experimental artefacts, such as scattering of the annihilation photons in materials in between the source and the crystal (e.g. the entrance window of the detector box or the front side APD array, see section 5.3.1), a small background contribution is included in the model. For each true beam position  $\underline{x}_b$ , the background is assumed to be uniformly distributed over the available reference coordinates:

$$b(\hat{x}_b - \underline{x}_b) = c \cdot U(x_r^{min} - x_b, x_r^{max} - x_b) \cdot U(y_r^{min} - y_b, y_r^{max} - y_b) \quad (5.11)$$

TABLE 5.1: Summary of the PSF models with and without a finite beam diameter in the test data. In all models, it is assumed that  $N_{ref} \rightarrow \infty$ .

PSF	Test beam	Model
$PSF_0$	No	$\gamma_0 * N_\Sigma + B$
$PSF_b$	Yes	$\gamma_b * N_\Sigma + B$

where  $c$  is a constant, and  $x_r^{min}$ ,  $x_r^{max}$ ,  $y_r^{min}$ , and  $y_r^{max}$  are the minimum and maximum  $x$ - and  $y$ -coordinates in the reference data, respectively.

In our experiments, the PSF is often determined by summing the PSFs at multiple beam positions in order to improve statistics on the histogram. The model background contribution for this case is found by summing the individual contributions  $b(\hat{x}_b - \underline{x}_b)$  over all  $\underline{x}_b$  in the test data:

$$B(\hat{x}_b - \underline{x}_b) = c \cdot \sum_{x_b} \sum_{y_b} U(x_r^{min} - x_b, x_r^{max} - x_b) \cdot U(y_r^{min} - y_b, y_r^{max} - y_b), \quad (5.12)$$

where it is assumed that  $c$  is equal for all beam positions, and that equal numbers of test events are used at each beam position. This expression is equivalent to a scaled convolution of two uniform distributions: one spanning the area containing the test coordinates, and one spanning the area containing the reference coordinates. In general, it therefore has a trapezoidal shape.

### PSF model summary

Table 5.1 summarizes the model expressions for the different cases described above. The PSFs carry a subscript ‘0’ or ‘b’, corresponding to the case of a zero-width beam, and a beam with finite diameter and divergence, respectively.

As explained in sections 5.2.2, the influences of the beam diameter (as accounted for by  $\gamma_b$ ) and of statistics and electronic noise (as accounted for by  $N_\Sigma$ ) only occur through the test data, provided that  $N_{ref} \rightarrow \infty$ ,  $L \rightarrow \infty$  and  $L/N_{ref} \rightarrow 0$ . We will verify how well our experiments approximate these conditions in section 5.4.3.

In the remainder of this work, the uniform distribution  $\Upsilon$  describing the influence of the finite distances between adjacent reference entry points is approximated by a delta function, in view of its narrow width compared to the width of the measured PSFs. It thus disappears from the convolution.

## 5.3 Materials and methods

### 5.3.1 Detector

The detector module investigated in this work has been discussed in detail elsewhere [40]. Briefly, it consists of a monolithic  $\text{LYSO}:\text{Ce}^{3+}$  crystal read out by two Hamamatsu S8550SPL APD arrays in double-sided readout (DSR) geometry, see figure 5.1. This S8550SPL APD array, based on the commonly available S8550

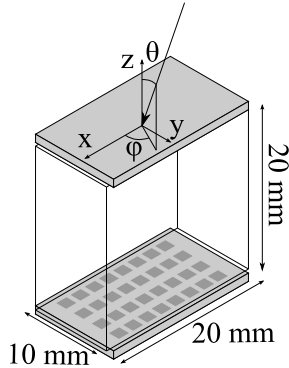


FIGURE 5.1: *Schematic representation of the detector investigated: a 20 mm thick  $\text{LYSO}:\text{Ce}^{3+}$  crystal read out by 2 position-sensitive, Hamamatsu S8550SPL APD arrays in double-sided readout (DSR) geometry. The thick arrow indicates a test beam of annihilation photons incident at some arbitrary position  $(x,y)$  on the front surface of the detector. Dimensions are indicated in mm.*

TABLE 5.2: *Properties of the crystal investigated*

Material	$\text{LYSO}:\text{Ce}^{3+}$
Surface	polished
Dimensions	20 mm $\times$ 10 mm $\times$ 20 mm
Light yield <sup>a</sup>	$2.02 \cdot 10^4$ ph/MeV
Energy resolution <sup>a</sup>	10.5% FWHM at 511 keV

<sup>a</sup> data from [40]

array, is a customized product optimized specifically for placement on the crystal front surface [3], as is done in DSR geometry. It consists of a  $4 \times 8$  array of  $1.6 \times 1.6$  mm APD pixels at a pitch of 2.3 mm. The properties of the crystal are summarized in table 5.2. The side surfaces of the crystal are wrapped in highly reflective Teflon tape.

### 5.3.2 Measurement setup

Reference and test data are recorded using a setup described elsewhere [40]. The detectors are contained in a light-tight, temperature controlled box. A test beam of 511 keV photons is defined by placing the detector close to a  $\varnothing 0.5$  mm  $^{22}\text{Na}$  source and operating it in coincidence with a second detector placed at a larger distance on the opposite side of the source. This second detector consists of a  $\varnothing 19 \times 35$  mm<sup>3</sup> BGO crystal coupled to an XP2020 PMT equipped with a 60 mm thick Pb collimator with  $\varnothing 5$  mm aperture, see figure 5.2. The diameter of the photon beam can be controlled by varying the distances between the APD detector, the source, and the BGO detector. Throughout this work, the FWHM diameter  $d$  of the fluence profile on the front surface of the LYSO crystal is used

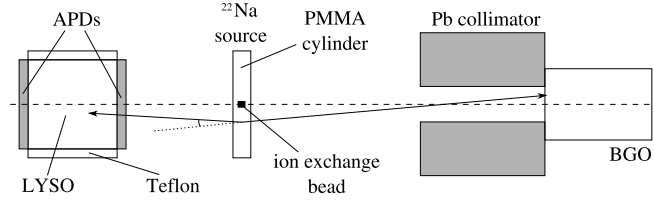


FIGURE 5.2: Schematic representation of the geometry of the test beam of annihilation photons used to measure detector PSFs (not to scale).

as a measure of the beam diameter.

### 5.3.3 Spatial resolution measurements

The detector PSF was evaluated for one half of the symmetric crystal only, in order to reduce measurement times. Reference data were recorded at a rectangular grid of beam positions in the region  $(-10 \leq x \leq 10 \text{ mm}, -2 \leq y \leq 5 \text{ mm})$ , in steps of 0.25 mm, see figure 5.1. Test data were recorded on a similar grid in the region  $(-3 \leq x \leq 3 \text{ mm}, 0 \leq y \leq 1.5 \text{ mm})$ . The margin between the two sets at  $-2 \text{ mm} < y < 0 \text{ mm}$  was applied to avoid truncation of the PSFs at  $y = 0$ . At each beam position,  $n_{ref} = 500$  reference events were recorded.

The entry point of each event in the test data set was estimated using the nearest neighbour procedure described in section 5.2.1. Calculation of the PSF was optimized by finding the value of  $L$  that minimized  $\langle \sigma_{PSF}^* \rangle \equiv (\sigma_{PSF,x}^* + \sigma_{PSF,y}^*)/2$ , i.e., the average of the standard deviations of the histogram in the  $x$ - and  $y$ - directions. The asterisks are used to indicate that PSF values below 1% of the peak amplitude were disregarded in order to reduce the sensitivity of the results to outliers.

The influences of some parameters (such as the beam diameter) were studied by varying the parameter of interest in a series of measurements performed in 1 dimension (1D) only, so as to reduce measurement times. In these studies,  $n_{ref} = 1500$  reference events were recorded per beam position between  $-10 \leq x \leq 10 \text{ mm}$  along the  $x$ -axis ( $y = 0$ ), in steps of 0.25 mm. Test data were recorded between  $-3 \leq x \leq 3 \text{ mm}$  ( $y = 0$ ). For optimization of  $L$  in 1D, the standard deviation  $\sigma_{PSF}^*$  of the measured 1D-PSF was minimized, again excluding bins lower than 1% of the peak amplitude.

### 5.3.4 Simulation of scattering and beam

To determine the energy centroid distribution  $\gamma_b$ , the experimental setup shown in figure 5.2 was modelled in a Monte Carlo simulation.

The simulated detector consisted of a  $20 \times 10 \times 20 \text{ mm}^3$  block of LSO coupled to two APD arrays, which were modelled as  $11.2 \times 19.5 \times 1.5 \text{ mm}^3$  slabs of silicon. The Teflon layer around the crystal was modelled as a 1 mm thick plastic layer (density  $0.9 \text{ g/cm}^3$ ).

The  $^{22}\text{Na}$ -source was simulated using the Monte Carlo simulation toolkit GATE [30]. The activity was assumed to be uniformly distributed within the

ion exchange bead. Positrons were generated and tracked until annihilation, and the coordinates of the annihilation positions were stored.

A simulation of pairs of 511 keV photons was then performed in GEANT4 [5]. For each photon pair, a point on the front surface of the BGO crystal lying within the collimator opening was randomly picked from a uniform distribution. The vector connecting this point to a randomly picked annihilation position from the set determined previously was then calculated. It was thus implicitly assumed that no 511 keV photons could reach the BGO-PMT detector through the lead of the collimator. Photon acollinearity was accounted for by adding a randomly picked angle to this vector at the annihilation position, according to a distribution determined experimentally for PMMA [31]. Annihilation photons were propagated along the resulting vector towards the APD detector, and upon interaction with the crystal, the coordinates of the energy deposition centroid were stored, taking a threshold of 100 keV for the total energy deposition into account.

The energy centroid distribution  $\gamma_0$  was simulated similarly, except that the test beam was replaced by a pencil beam of zero diameter perpendicularly incident on the detector.

The distributions  $\gamma_0$  and  $\gamma_b$  were obtained by creating histograms of the  $x$ - and  $y$ -coordinates of the energy deposition centroids within the crystal. The coordinates at which the 511 keV photons crossed the front surface of the crystal were also histogrammed, providing an estimate of the beam diameter  $d$ .

### 5.3.5 Model fitting procedure

Fitting the model to measured PSFs was done by minimizing the sum-of-squares (SSQ) difference between the appropriate model from table 5.1 and the experimental result. The simulated distributions  $\gamma_0$  and/or  $\gamma_b$  were used as fixed inputs, while the amplitude and covariance matrix of  $N_\Sigma$  and the amplitude of  $B$  were used as fit parameters.

## 5.4 Results and discussion

In the following, we first fit the model derived in section 5.2.2 to the measured detector spatial response. In section 5.4.2, the model is then used to quantify the influence of the test beam diameter on the measured spatial response and it is shown how a correction for this influence can be made to estimate the intrinsic detector PSF. Using the fitting and correction methods thus demonstrated, a detailed validation of the different model components is performed in section 5.4.3.

### 5.4.1 Detector PSF

All spatial resolution measurements were performed with a test beam having a finite diameter  $d$ , see section 5.3.2. Hence, the results are of type ‘ $PSF_b$ ’ as defined in table 5.1.

The cross-section of  $PSF_b(x)$  for the measured 2D detector spatial response in the  $x$ -direction at zero  $y$ -error is shown in figure 5.3 (circles). The result of a least-squares fit to the measured data of the model of  $PSF_b(x, y)$  for the

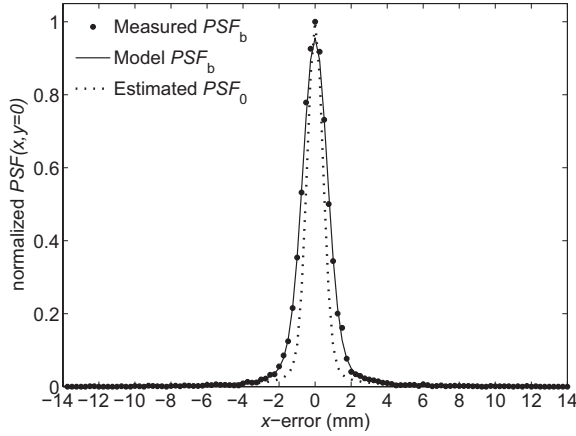


FIGURE 5.3: Cross-sections  $PSF_b(x)$  for the measured (solid circles) and fitted (solid curve)  $PSF_b(x, y)$ , and cross-section  $PSF_0(x)$  of the corrected  $PSF_0(x, y)$  (dotted curve).  $PSF_b(x, y)$  was obtained using  $L = 500$ .

case  $L \rightarrow \infty \wedge L/N_{ref} \rightarrow 0$  is indicated by the solid curve in the same graph. Excellent correspondence between the model and the experiment is observed. Similarly good correspondence was observed in the  $y$ -direction, i.e. for  $PSF_b(y)$ .

## 5.4.2 Correction for test beam diameter

Assuming that the model accurately describes the various contributions to the measured  $PSF_b$ , it can be used to quantify the influence of the test beam diameter and, therefore, to make a correction for this influence. This is done as follows. First, the distributions  $N_\Sigma$  and  $B$  are determined by fitting  $PSF_b(x, y)$  to the measured data, using a Monte Carlo simulation of the test beam for determining  $\gamma_b$  as in section 5.4.1. Subsequently,  $PSF_0(x, y)$  is estimated by convolving the resulting  $N_\Sigma$  with  $\gamma_0$ , and adding  $B$  (see table 5.1). Here,  $\gamma_0$  is determined from a Monte Carlo simulation of a beam with zero diameter. The result of this procedure is denoted by  $PSF_0(x, y)$ .

The dotted curve in figure 5.3 shows the cross-section  $PSF_0(x, y)$  estimated from the measured curve shown in the same figure. Figure 5.4 shows the corresponding cross-sections through  $\gamma_b$  (solid black curve),  $\gamma_0$  (solid grey curve),  $N_\Sigma$  (dashed curve), and  $B$  (dotted curve), where the amplitude of  $B$  has been scaled according to the amplitude of  $\{\gamma_b * N_\Sigma\}$ .

The FWHM and FWTM of the measured and corrected PSFs are listed in table 5.3. A very good intrinsic detector spatial resolution of 1.05 mm FWHM is found in the  $x$ -direction.

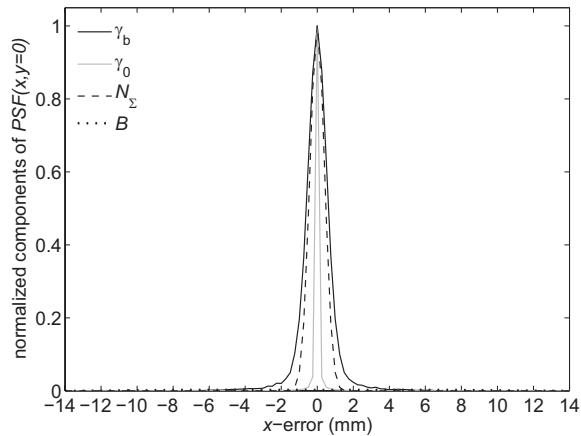


FIGURE 5.4: Cross-sections along the  $x$ -axis for the distributions  $\gamma_b$  (solid black curve),  $\gamma_0$  (solid grey curve),  $N_\Sigma$  (dashed curve) and  $B$  (dotted curve) for  $L = 500$ .

TABLE 5.3: FWHM and FWTM of cross-section  $PSF_b(x)$  of the measured  $PSF_b(x, y)$  and cross-section  $PSF_0(x)$  of the corrected  $PSF_0(x, y)$ , obtained with  $L = 500$ .

PSF	PSF(x) (mm)		PSF(y) (mm)	
	FWHM	FWTM	FWHM	FWTM
$PSF_b(x)$	1.54	3.33	1.61	3.80
$PSF_0(x)$	1.05	2.09	1.25	2.42

### 5.4.3 Validation of the model

We demonstrated in section 5.4.1 that the PSF model can accurately be fitted to measured PSFs. In section 5.4.2 it was shown how the model can be used to quantify the influence of the test beam diameter and to correct the measured PSF for this influence. In this section, we will further investigate the validity of the model. Section 5.4.3 presents a validation of the model parameter  $\gamma_b$ , section 5.4.3 investigates to which extent the conditions  $N_{ref} \rightarrow \infty$ ,  $L \rightarrow \infty$ , and  $L/N_{ref} \rightarrow 0$  are met in the present experiments, and section 5.4.3 discusses how well the influence of noise and statistics is accounted for by the Gaussian distribution  $N_\Sigma$ .

For efficiency, all experiments presented here were done in the form of 1D resolution measurements. This implies that each of the distributions  $\gamma_0$ ,  $\gamma_b$ ,  $N_\Sigma$  and  $B$  in table 5.1 reduce to 1D functions, i.e., only the x-coordinate is being taken into account. Instead of  $N_\Sigma$  we therefore use a 1D Gaussian distribution  $N_\sigma$  with standard deviation  $\sigma$ . The resulting point spread functions are denoted by ‘1D- $PSF_b$ ’ etc.

#### Validation of $\gamma_b$

One of the principle assumptions in the derivation of the model is that the influence on the measured  $PSF_b$  of the spatial distribution of the energy deposited within the crystal by the test beam can be accounted for by  $\gamma_b$ , the distribution of the energy deposition centroids of the recorded events. This assumption was tested by creating 1D-PSFs with various test data sets, each acquired with a different beam diameter  $d_t$  ranging from 0.84 mm FWHM to 1.46 mm FWHM. Each PSF was created using the value of  $L$  that minimized its standard deviation  $\sigma_{PSF}^*$  (see section 5.3.3), thus minimizing residual effects due to the finite number of reference events (which will be discussed in section 5.4.3). The same reference data set acquired with beam diameter  $d_r = 0.84$  mm FWHM was used for each PSF, in order to keep any remaining influence of the limited number of reference data constant. According to the model, it should then be possible to accurately describe all 1D- $PSF_b$  using different  $\gamma_b$  but the same  $N_\sigma$ .

Figure 5.5 shows the FWHM (filled circles) and the FWTM (open circles) of 1D- $PSF_b$  as a function of  $d_t$ . The FWHM (black squares) and FWTM (open squares) of the corrected 1D- $PSF_0$  are shown in the same figure. Each 1D- $PSF_0$  was created by first fitting the model to the data using the appropriate  $\gamma_b$  and then convolving the resulting  $N_\sigma$  with  $\gamma_0$ . The FWHM and FWTM of the resulting 1D- $PSF_0$  indeed appear to be virtually independent of  $d_t$ . It appears that  $\gamma_b$  indeed describes the influence of intra-crystal scattering and of the finite beam diameter on the measured spatial response accurately, and that the proposed procedure to correct for this influence is adequate.

It is acknowledged that no theoretical justification is given for using the Gaussian distribution  $N_\sigma$  to describe the influence of statistical fluctuations and noise in the test data. However, the accuracy of the model fit presented in figure 5.3 indicates that this assumption is valid under the present experimental conditions. This will be discussed further in section 5.4.3.

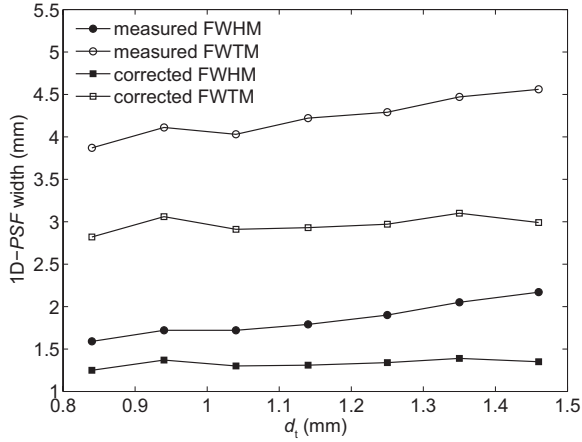


FIGURE 5.5: *FWHM and FWTM of measured  $1D-PSF_b$  and corrected  $1D-PSF_0$  as a function of the beam diameter  $d_t$  in the test data. All  $1D-PSFs$  were obtained using the same reference data recorded with a beam diameter  $d_r = 0.84$  mm FWHM, using  $n_{ref} = 1500$  and the value of  $L$  that minimized  $\sigma_{PSF}^*$ .*

#### Influence of the finite reference data set

In the derivation of the model, it was shown that the influences of the beam diameter and intra-crystal scattering on the reference data should not affect the measured spatial response, provided that  $N_{ref} \rightarrow \infty$ ,  $L \rightarrow \infty$ , and  $L/N_{ref} \rightarrow 0$ , see section 5.2.2. These conditions can however never be met experimentally, so that a small influence of the beam diameter in the reference data may still be expected.

This was investigated by calculating  $1D-PSF_b$  as a function of the beam diameter in the reference data  $d_r$  ( $0.84 \text{ mm} \leq d_r \leq 1.46 \text{ mm}$  FWHM), at various values of  $L$ . Here, each PSF was obtained using the same test data set recorded at  $d_t = 0.84 \text{ mm}$  FWHM.

Figure 5.6 shows the FWHM of  $1D-PSF_b$  as a function of  $d_r$  for various values of  $L$ . At  $L = 1$  the FWHM increases from 2.31 mm at  $d_r = 0.84 \text{ mm}$  to 2.78 mm at  $d_r = 1.46 \text{ mm}$ . At  $L = 500$  this dependence is reduced, resulting in an increase of the FWHM from 1.75 mm at  $d_r = 0.84 \text{ mm}$  to 1.86 mm at  $d_r = 1.46 \text{ mm}$ . Thus, a slight dependence on  $d_r$  remains, even at high values of  $L$ . This is attributed to the finite number of reference events  $n_{ref}$  per beam position ( $\sim 1500$  in these experiments). If the number of reference events recorded at the reference position  $\underline{x}_r$  closest to the  $\underline{x}_c'$  corresponding to the measured light distribution is not large compared to  $L$ , some of the nearest neighbours may be selected from other reference positions. In that case the probability  $\Pr(\hat{x}_e | \underline{x}_c')$  that the positioning algorithm assigns a coordinate  $\hat{x}_e$ , given the measured  $\underline{x}_c'$ , may no longer be given by the uniform distribution  $\Upsilon$  (see equation (5.7)). It is therefore expected that increasing the number of reference events may allow some further improvement of the detector resolution by eliminating the slight

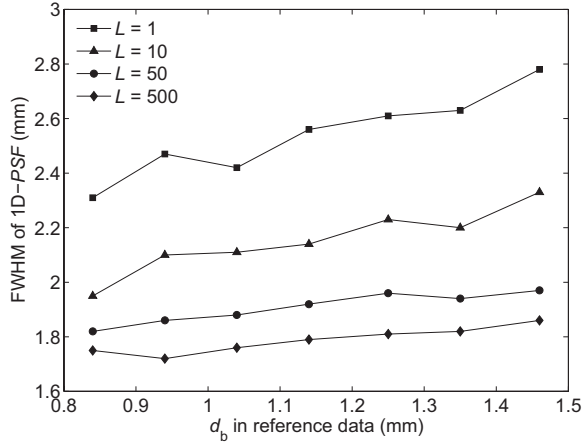


FIGURE 5.6: *FWHM of measured 1D-PSF<sub>b</sub> as a function of the beam diameter  $d_r$  in the reference data, for various values of  $L$ . Each 1D-PSF<sub>b</sub> was created using the same set of test data recorded at  $d_t = 0.84$  mm.*

influence of  $d_r$  still observed in the present experiments.

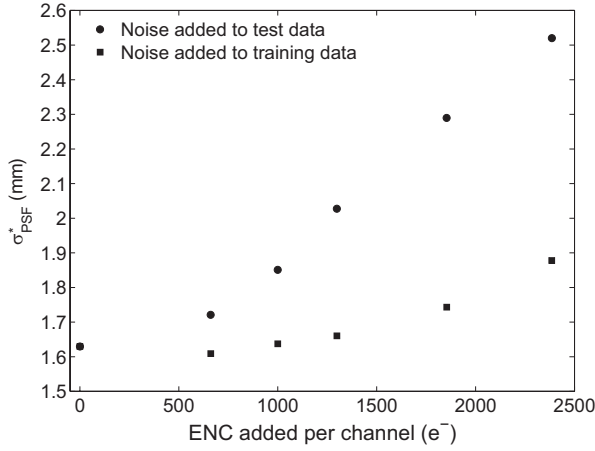
#### Influence of statistical fluctuations and noise

The influence of the statistical fluctuations and noise in the measured light distributions on 1D-PSF<sub>b</sub>, which is accounted for by  $N_\Sigma$  in the model, was investigated by adding Gaussian noise to the data by software. This was done on top of the  $\sim 750$  e<sup>-</sup> per channel equivalent noise charge (ENC) already present at the APD array outputs [40].

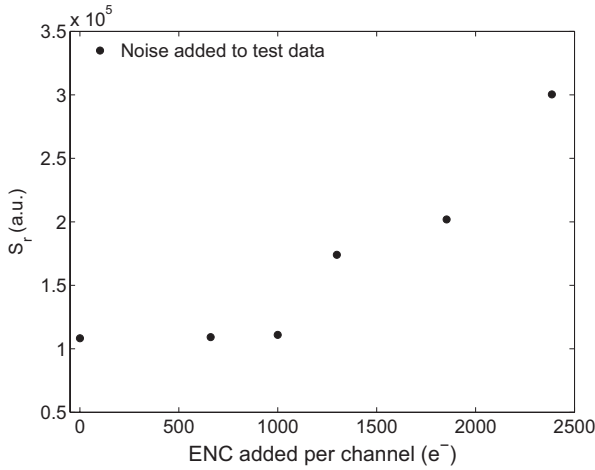
The squares in figure 5.7 show the standard deviation  $\sigma_{PSF}^*$  of 1D-PSF<sub>b</sub> as a function of the noise added to the reference data. Here, the same test data set without added noise was used in each case. For comparison, the opposite case (noise added to the test data, but not to the reference data) is indicated by the circles in the same figure.

While  $\sigma_{PSF}^*$  increases immediately when noise is added to the test data, it remains approximately constant when noise is added to the reference data, up to an added ENC of  $\sim 1250$  e<sup>-</sup>. This indicates that under the present experimental conditions, the finite signal-to-noise ratio (SNR) of the reference data has a negligible influence on the PSF. However, if the SNR of the reference data is decreased too much, a broadening of the PSF may be expected. The minimum SNR required for the reference data depends on the number of reference events  $N_{ref}$ .

To investigate up to which noise level the influence of statistical fluctuations and noise is accurately accounted for by the Gaussian distribution  $N_\Sigma$  in the model, the residual sum of squares  $S_r = \sum_i (PSF_{b,fit}(x_i) - PSF_{b,exp}(x - i))^2$  was calculated as a function of the amount of noise added to the test data. Here,  $PSF_{b,fit}$  and  $PSF_{b,exp}$  represent the fitted and measured 1D-PSF<sub>b</sub>, respectively.



(a)



(b)

FIGURE 5.7: (a) standard deviation  $\sigma_{PSF}^*$  of measured  $1D-PSF_b$  and (b) residual sum of squares  $S_r$  resulting from fitting the model to the same  $1D-PSF_b$ , as a function of the equivalent noise charge in the test data (circles) and in the reference data (squares). The values on the horizontal axis represent the noise added to the  $\sim 750 e^-$  of electronic noise per channel already present in the experimental data. At each data point, the value of  $L$  that minimized  $\sigma_{PSF}^*$  for that particular noise level was used.

The results of this analysis are shown in figure 5.7b. Below  $\sim 500$   $e^-$  ENC added per channel,  $S_r$  does not increase strongly with increasing noise. At higher noise levels, however,  $S_r$  starts to increase more rapidly. This suggests that  $N_\Sigma$  can indeed be approximated by a Gaussian distribution at the relatively low noise levels found in our measurements, but that this simple approximation loses its applicability if the noise level is increased too much.

## 5.5 Conclusions

We derived a simple model of the point spread function of monolithic scintillator detectors, which accounts for the spatial distribution of the energy depositions following the interaction of annihilation photons within the scintillator, as well as for the influence of signal fluctuations arising from photon and charge carrier statistics and from electronic noise. The model was used to analyze the measured spatial response of a prototype monolithic scintillator detector consisting of a  $\text{LYSO:Ce}^{3+}$  crystal and two APD arrays in double-sided readout (DSR) geometry. The effect of the finite diameter of the test beam of annihilation photons used in our experiments on the measured detector spatial response was quantified, and it was demonstrated how a correction for this influence can be made to estimate the intrinsic detector PSF.

The results show that the proposed model describes the measured spatial response well within certain boundary conditions. Specifically, the model is based on the assumption that  $N_{ref} \rightarrow \infty$ . For this case, the model predicts that the best possible spatial resolution is achieved if  $L \rightarrow \infty$  with  $L/N_{ref} \rightarrow 0$ . The extent to which these conditions are approximated by the finite values of  $L$  and  $N_{ref}$  used in practice depends not only on the values of  $L$  and  $N_{ref}$  themselves, but also on the beam diameter  $d_b$  and on the signal-to-noise ratio of the measured light distributions. Furthermore, the extent to which the influence of the signal-to-noise ratio on the measured point spread function is accurately represented by a simple Gaussian distribution  $N_\Sigma$  was found to depend on the signal-to-noise ratio. It was shown that this approximation is valid at the signal-to-noise ratios found in our experiments.

We thus conclude that the proposed model is an accurate and useful tool for analyzing the detector PSF of monolithic scintillator detectors and for correcting measured spatial resolution of such detectors for the influence of the finite diameter of the test beam of annihilation photons used in spatial resolution measurements.

---

### Simulated performance of small-animal PET scanners based on monolithic scintillator detectors<sup>1</sup>

---

**This chapter presents a pilot study of the performance of small-animal PET systems based on monolithic scintillator detectors. The study is based on Monte Carlo simulations which use measurements of the PSFs and other detector properties as input. Simulations are performed of scanners consisting of 1 or 4 rings with an inner diameter of 123.8 mm and an axial extent of 19.5 mm, each containing 32 detectors of 20 mm thick LSO.**

**The system resolution of the 1-ring scanner is estimated in 2D, both for ideal mathematical point sources without positron range or photon acollinearity, and for realistic  $\varnothing 0.5$  mm  $^{18}\text{F}$  sources. Very little degradation of the system resolution towards the edge of the field of view of the scanner is observed in either case. A 2D image of a simulated  $^{18}\text{F}$ -filled micro-Derenzo hot rod phantom reconstructed with an OSEM algorithm shows that rods with a diameter of 2.4 mm are well resolved.**

**The sensitivity for coincident detection at low count rates is estimated at 21% at the centre of the FOV of a 4-ring scanner with trapezoidally shaped detectors. This is substantially higher than the 3–4% reported for current state of the art systems. The NECR calculated for this system reaches 2000 kcps in a  $\varnothing 36 \times 67$  mm<sup>3</sup> water phantom uniformly filled with  $^{18}\text{F}$  at an activity of 70 MBq.**

**Further improvement of the image quality is expected with an optimisation of the reconstruction algorithm and the detector geometry.**

---

<sup>1</sup>Part of this chapter has been published as: D. J. van der Laan, M. C. Maas, H. W. A. M. de Jong, D. R. Schaart, P. Bruyndonckx, C. Lemaitre and C. W. E. van Eijk, 'Simulated performance of a small-animal PET scanner based on monolithic scintillation detectors, *Nuclear Instruments and Methods in Physics Research A* 571 (2007), 227–330.

## 6.1 Introduction

The performance of monolithic scintillator detectors has been summarised in [40]. The results were promising: a corrected detector spatial resolution of  $\sim 1.05$  mm FWHM was found (see section 5.4.2, comparable to current state-of-the-art small animal PET systems, and the correction for the depth-of-interaction of incident 511 keV photons was found to be excellent. The energy and timing resolutions measured with these detectors are suitable for application in PET. In addition, the detectors have a high detection efficiency and compact design, suggesting that a PET scanner based on these detectors could have excellent performance characteristics.

This chapter presents a pilot study into the performance potential of small-animal PET scanners based on monolithic scintillator detectors, in terms of the image spatial resolution, the scanner sensitivity and the count rate performance. This is done by Monte Carlo simulations using experimental point spread functions (PSFs) and other performance parameters measured on a prototype detector module as input.

The image spatial resolution obtainable with these scanners is investigated in 2D acquisition mode. This is done by simulating a PET system consisting of 1 ring with an inner diameter of 123.8 mm containing 32 trapezoidally shaped detectors. The intrinsic system resolution of this system is analysed by simulating mathematical point sources emitting back-to-back annihilation photons at a range of radial distances from the scanner axis, neglecting positron range and photon acollinearity. The system resolution in response to realistic point sources is also investigated, by simulating eight  $\varnothing 0.5 \times 1$  mm<sup>3</sup> <sup>18</sup>F-sources at various radial distances from the scanner axis, taking positron range and photon acollinearity into account. Finally, the image resolution obtained with a Micro-Derenzo hot rod phantom filled with <sup>18</sup>F is analysed.

The scanner sensitivity and noise equivalent count rate (NECR) are analysed for scanners consisting of four rings of detectors. A comparison is made between trapezoidal monolithic detector modules, rectangular monolithic detector modules, and detector modules consisting of  $8 \times 4$  matrices of  $2 \times 2 \times 20$  mm<sup>3</sup> crystals. The scanner sensitivity is investigated as a function of the axial and the radial distance from the scanner centre using a 1 MBq mathematical point source emitting back-to-back 511 keV photons. The NECR is determined using simulations of a mouse phantom and a rat phantom, modelled respectively as a  $\varnothing 36 \times 67$  mm<sup>3</sup> and a  $\varnothing 60 \times 150$  mm<sup>3</sup> water cylinder filled with uniform <sup>18</sup>F activity.

## 6.2 Methods

### 6.2.1 Monte Carlo simulations

Simulations were performed using the Monte Carlo simulation toolkit GATE [30]. The simulated scanners consisted of one or four rings of 32 detector modules each. Each ring had an inner diameter of 123.8 mm and an axial length of 19.5 mm. In the 4-ring scanners, the rings were positioned at an axial pitch of 21 mm.

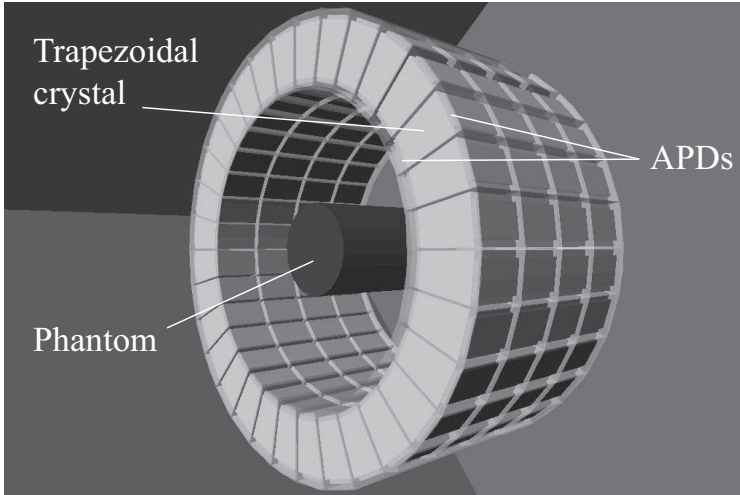


FIGURE 6.1: *Four-ring scanner with trapezoidal detectors.*

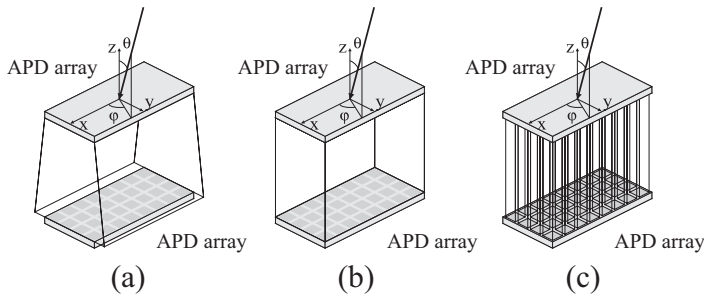


FIGURE 6.2: *Detector types investigated: (a) trapezoidal, (b) rectangular, (c) pixel matrix.*

Three different detector geometries were investigated: trapezoidal monolithic crystal detectors, rectangular monolithic crystal detectors, and detectors with  $8 \times 4$  crystal matrices. An illustration of the 4-ring scanner with trapezoidal detectors is presented in figure 6.1. The detector types are depicted in figure 6.2, which also shows the coordinate system used to specify positions and angles of incidence on the detector front surface. The trapezoidal crystals had a front surface of  $11.5 \times 19.5 \text{ mm}^2$ , a back surface of  $15.4 \times 19.5 \text{ mm}^2$  and a depth of 20 mm. The rectangular crystals had dimensions of  $19.5 \times 11.5 \times 20 \text{ mm}^3$ , and the matrix detectors had  $8 \times 4$  crystals of  $2 \times 2 \times 20 \text{ mm}^3$  at a pitch of 2.2 mm. The crystal material in each detector was LSO:Ce, and each module was coupled to 2 Hamamatsu S8550-SPL APD arrays, modelled as  $11.2 \times 19.5 \times 1.5 \text{ mm}^3$  slabs of silicon.

In each simulation, the locations and energy depositions of the interactions within the crystal of each 511 keV photon entering a detector were stored. The total energy deposited was blurred with a Gaussian distribution with a FWHM

of 10% of the energy value as an approximation of the energy resolution measured with these detectors, see [40]. Events with blurred total energy depositions outside an energy window of 250–750 keV were rejected. For each single event within the energy window, a detector dead time of 0.5  $\mu\text{s}$  was applied. All single events were stored in list mode for offline coincidence sorting.

The time stamp of each detected single was blurred with a Gaussian distribution with a FWHM of 2 ns, based on measurements of the timing resolution of a prototype detector module [40]. A coincidence time window of 5 ns was used, approximately twice the coincidence timing resolution of 2.8 ns obtained experimentally [44]. Coincident events in which more than two detector modules were involved were rejected.

After sorting the coincidences, the entry point and incidence angle of each 511 keV photon was determined. Each entry point was then projected onto the detector  $y$ -axis (see figure 6.2), since the image resolution was determined in 2D only in this study. The projected entry points were then blurred by adding a positioning error randomly selected from the corrected 1D-PSF of the detector corresponding to the nearest test beam position and incidence angle (see section 6.2.2). The lines-of-response (LORs) corresponding to these blurred entry points were then calculated and sorted into 2D sinograms.

### 6.2.2 Intrinsic detector PSF

The 1D-PSF of the trapezoidal detectors was measured according to the procedure outlined in [40]. A prototype detector (LYSO20T-P) was stepped through a beam of 511 keV photons of  $d_b = 0.96$  mm FWHM along the detector  $y$ -axis in steps of 0.25 mm, i.e. in the plane of the detector ring. At each beam position,  $n_{ref} = 1500$  reference light distributions were recorded. This was done for incidence angles between  $\theta = 0^\circ$  and  $\theta = 40^\circ$ , in steps of  $5^\circ$ , at  $\varphi = 90^\circ$  (see figure 6.2), yielding a total of 9 data sets. The oblique sides of the crystals were included in the data sets at all angles of incidence. The entry point coordinate of each event in each of the data sets was estimated with the  $L$ -nearest neighbour method, using the leave-one-out approach (see chapter 5).

The positioning error of each test event was calculated by subtracting the estimated coordinate from the true, known coordinate. This way, histograms of positioning errors were created for each beam position and each angle of incidence. Each of these histograms corresponds to the detector 1D-PSF at a certain position and angle of incidence on the front surface of the detector. In the present analysis, the 1D-PSFs were averaged over 1 mm data segments.

The intrinsic 1D-PSF exhibited by the detectors in a PET system corresponds to their response to an infinitely narrow beam. The measured 1D-PSFs were therefore corrected for the finite width of the test beam. The beam profile was determined using Monte Carlo simulations of an accurate model of the measurement setup in Geant4 [5], see chapter 5. The procedure to correct the PSFs for the finite diameter of the test beam presented in chapter 5 could not be used in this study, because the model on which it is based was only derived for normally incident 511 keV photons at the centre of the detector front surface. The intrinsic detector 1D-PSFs were therefore estimated by deconvolution of the

measured 1D-PSFs with the simulated beam profile.

### 6.2.3 Scanner performance

#### Image spatial resolution

The system resolution obtainable with the proposed scanner type was investigated in 2D, by simulating a 1-ring system of trapezoidal detectors. To investigate the intrinsic resolution of this scanner, a 0.5 kBq mathematical point source emitting back-to-back annihilation photons was simulated, neglecting positron range and acollinearity. The source was placed at radial positions  $r$  in the field of view (FOV) ranging from  $r = 0$  mm (center FOV) to  $r = 29$  mm, in steps of 1 mm. A simulation of  $10^6$  events was performed at each source position, and no attenuation correction, normalisation or subtraction of random coincidences was performed. The LORs were binned into 2D sinograms with a bin size of  $r \times \phi = 0.5 \text{ mm} \times 0.9^\circ$ . Reconstruction of the sinograms was performed by filtered backprojection with a ramp filter with a cutoff at the Nyquist frequency, resulting in an image with pixels with a size of  $0.5 \times 0.5$  mm.

The system resolution obtainable with realistic point sources was investigated by simulating eight 0.5 kBq  $\varnothing 0.5 \times 1 \text{ mm}^3$   $^{18}\text{F}$ -sources each embedded in a  $\varnothing 4.6 \times 5 \text{ mm}^3$  PMMA cylinder, at radial positions ranging from  $r = 0$  mm to  $r = 35$  mm in steps of 5 mm. A total number of  $37 \cdot 10^6$  positron emission events were simulated, taking positron range and photon acollinearity into account. The LORs were binned into 2D sinograms with a bin size of  $r \times \phi = 0.5 \text{ mm} \times 0.9^\circ$ . Reconstruction of the sinograms was performed by filtered backprojection with a ramp filter with a cutoff at the Nyquist frequency, resulting in an image with pixels with a size of  $0.5 \times 0.5$  mm.

Finally, simulations were performed of a micro-Derenzo phantom, consisting of a  $\varnothing 77 \times 35 \text{ mm}^3$  PMMA cylinder with 6 segments of radioactive rods with diameters of 1.2, 1.6, 2.4, 3.2, 4.0 and 4.8 mm containing 2 MBq of  $^{18}\text{F}$ . The distance between the rods in each segment was twice the diameter, and the activity was contained in the central 1 cm of the axial field of view. A total number of  $3.3 \cdot 10^8$  events were simulated. No correction for scattered events, attenuation or random coincidences was performed, and the sinograms were not normalised. The sinograms were reconstructed using a 2D-OSEM algorithm with 10 subsets and 30 iterations, resulting in an image with pixels with a size of  $0.5 \times 0.5$  mm.

#### Scanner sensitivity

To assess the scanner sensitivity, simulations of three 4-ring systems with trapezoidal monolithic detectors, rectangular monolithic detectors and crystal matrix detectors were performed, see section 6.2.1. The sensitivity of each of these systems was investigated by stepping a 1 MBq point source of back-to-back 511 keV photons from the centre to the edge of the FOV, both axially and radially, in steps of 1 mm. At each source position,  $\sim 10^6$  events were simulated. An energy window of 250–750 keV was used for each detector. The sensitivity was calculated by dividing the true coincidence count rate by the activity of the point source.

### Count rate performance

The count rate performance of a scanner represents its ability to reject random and scattered coincidences at a given source activity. It can be quantified using the noise equivalent count rate (NECR), which can be calculated using the relationship [72]:

$$\text{NECR} = \frac{T^2}{T + S + 2kR}, \quad (6.1)$$

where  $T$  is the rate of true coincidences,  $S$  is the rate of scattered coincidences,  $R$  is the rate of random coincidences and  $k$  is the ratio of the phantom diameter and the scanner diameter. The factor 2 in the denominator accounts for the method of randoms correction, which is assumed to be a delayed coincidence technique for the present study.

The NECR of the 4-ring system with trapezoidal detectors was determined using simulations of a mouse phantom and a rat phantom. The phantoms were modelled respectively as a  $\varnothing 36 \times 67$  mm<sup>3</sup> and a  $\varnothing 60 \times 150$  mm<sup>3</sup> water cylinder filled with uniform <sup>18</sup>F activity.

## 6.3 Results

### 6.3.1 Spatial resolution

Figure 6.3 shows the radial (squares) and tangential (triangles) FWHM intrinsic system resolution in response to mathematical point sources emitting back-to-back 511 keV photons at a range of radial distances from the central field of view (CFOV). These numbers were obtained by linear interpolation of the intensity profile through the pixel with maximum intensity for each source position. The spatial resolution is essentially uniform and isotropic over a range up to 3 cm off-centre, in agreement with the excellent correction for the DOI previously reported for these detectors [40].

Figure 6.4 shows an filtered back-projection (FBP) reconstructed image of the eight  $\varnothing 0.5$  mm <sup>18</sup>F point sources. Linear interpolation of the profiles through the pixel with maximum intensity yields a system resolution at the CFOV of  $\sim 1.4$  mm FWHM and  $\sim 3.3$  mm FWTM. At 35 mm from the CFOV, this degrades to 2.1 mm FWHM and 4.1 mm FWTM radially, and 2.3 mm FWHM and 5.7 mm FWTM tangentially.

Figure 6.5 shows 2D-OSEM reconstructed images of the micro-Derenzo phantom. In figure 6.5a, the source emitted back-to-back 511 keV photons, neglecting positron range and photon acollinearity. Attenuation and scatter within the phantom were set to zero. In figure 6.5b, a realistic positron source with an energy distribution corresponding to <sup>18</sup>F was simulated, and photon acollinearity, attenuation and scatter within the phantom were taken into account. No attenuation correction, scatter correction or normalisation was applied to the data to create either image. No randoms correction was applied in view of the low activity (0.5 kBq) of the simulated sources.

In figure 6.5a, the 2.4 mm rods are clearly separated while the 1.6 mm rods are not, in agreement with the results presented for the mathematical point sources

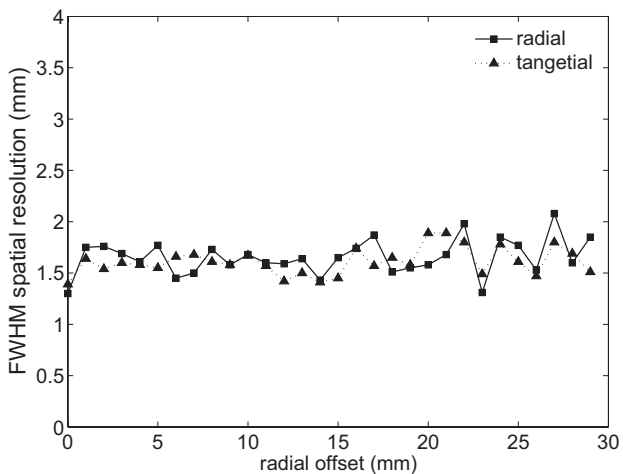


FIGURE 6.3: Radial (squares) and tangential (triangles) FWHM spatial resolution of a mathematical point source as a function of the radial position. Positron range and photon acollinearity were set to zero in these simulations.

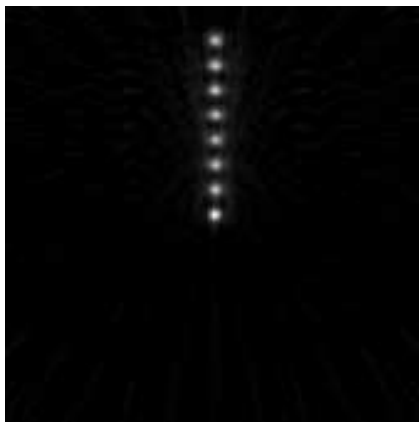


FIGURE 6.4: Reconstructed image of eight  $\varnothing 0.5$   $^{18}\text{F}$  point sources at radial distances of 0, 5, ..., 35 mm from the scanner CFOV.

(figure 6.3). In figure 6.5b, the 2.4 mm rods can still be identified, but the separation is less distinct due to the blurring effect of positron range and photon acollinearity. Radial distortion of the rods on the outside of the FOV is observed in neither image, owing to the good DOI correction of the detectors.

Ring-shaped artefacts can be observed around each row of rods in figure 6.5a. Although less clearly discernible, these artefacts are also observed in figure 6.5b.

### 6.3.2 Sensitivity

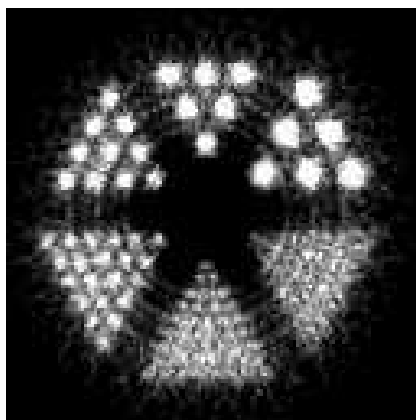
The point source sensitivity is plotted in figure 6.6 as a function of the radial and axial distance from the CFOV for the three 4-ring systems with trapezoidal monolithic detectors (solid lines), rectangular monolithic detectors (dotted lines), and crystal matrix detectors (dashed lines). The sensitivities at the CFOV are 21% for the trapezoidal detectors, 17.5% for the rectangular detectors and 8% for the crystal matrix detectors. The rectangular monolithic detectors have a sensitive volume that is  $\sim 56\%$  larger than that of the crystal matrix detectors, resulting in an increase of the scanner sensitivity of approximately a factor 2. The more favourable geometry of the trapezoidal detectors compared to the rectangular ones results in a further increase of the scanner sensitivity of 20%. In addition, the radial sensitivity profile is smoother for the trapezoidal detectors than for the other geometries, due to the reduced dead space between the detector modules.

### 6.3.3 Count rate performance

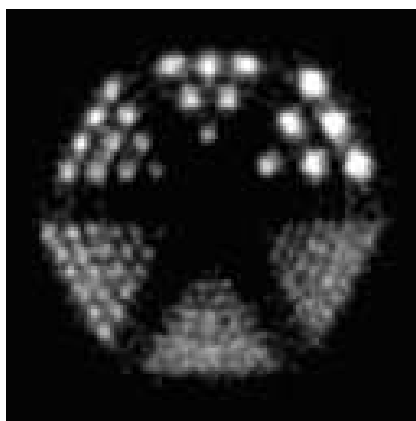
The noise equivalent count rate of the 4-ring scanner with trapezoidal detectors is plotted in figure 6.7 as a function of the total activity for the  $\varnothing 36 \times 67 \text{ mm}^3$  mouse phantom (solid line) and the  $\varnothing 60 \times 150 \text{ mm}^3$  rat phantom (dotted line). The NECR reaches a maximum of 2000 kcps with the mouse phantom at an activity of 70 MBq. The NECR obtained with the rat phantom is considerably lower, reaching a maximum of 550 kcps at an activity of 70 MBq. This is due to the larger dimensions of the rat phantom, of which approximately 48% of the volume lies outside the scanner FOV. This activity outside the FOV leads to an increased number of random coincidences, but does not contribute to the number of true coincidences. In addition, the number of scattered events coming from within the FOV is larger in the rat phantom due to its larger diameter. For both NECR curves, only a minor deviation from linearity is observed at activities commonly used in small-animal PET ( $< 40 \text{ MBq}$ ).

## 6.4 Discussion

The unconventional shape of the detector point spread function complicates estimating the system resolution that should be achievable intuitively. In order to obtain such an estimate, an image of a mathematical point source at the CFOV was re-created using idealised detector PSFs. This was done by creating a model 1D-PSF, convolving an energy centroid distribution in response to a zero-width pencil beam with a Gaussian distribution. The standard deviation of the Gaussian was set at  $\sigma = 0.46 \text{ mm}$ , which is a common value for our detectors (see



(a)



(b)

FIGURE 6.5: Reconstructed images of a micro-Derenzo hot rod phantom with rods with diameters of 1.2, 1.6, 2.4, 3.2, 4.0, and 4.8 mm, uniformly filled with activity. In (a), the source emits back-to-back photons, and positron range and photon acollinearity are neglected. Attenuation and scatter within the phantom are set to zero. In (b), a positron emitting source with an energy distribution corresponding to  $^{18}\text{F}$  is used, and photon acollinearity is taken into account, as well as attenuation and scatter within the phantom. Correction for attenuation and scattered events and normalisation were not applied to obtain these images.

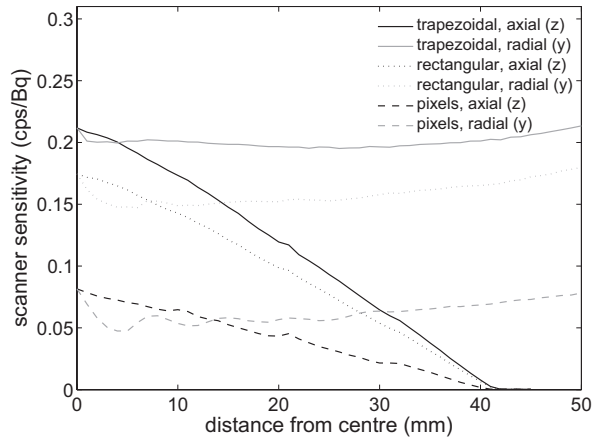


FIGURE 6.6: Axial and radial point-source sensitivity curves of the three 4-ring systems with trapezoidal monolithic detectors (solid lines), rectangular monolithic detectors (dotted lines), and crystal matrix detectors (dashed lines).

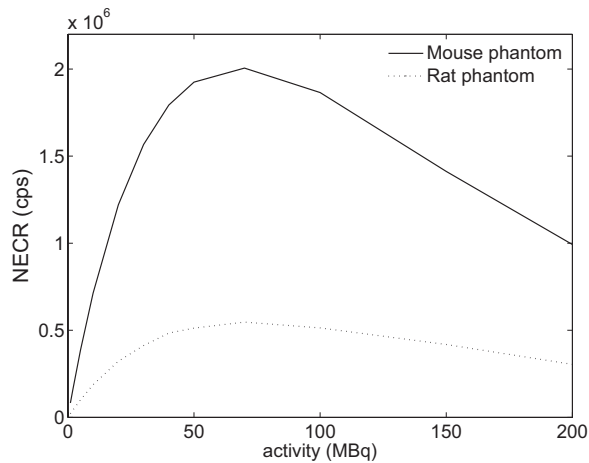


FIGURE 6.7: Noise equivalent count rate as a function of total activity of the 4-ring scanner with trapezoidal detectors for the mouse phantom (solid line) and the rat phantom (dotted line).

chapter 5). This resulted in a 1D-PSF with a FWHM of 1.24 mm. This model PSF was applied to all entry points in the data, regardless of position or incidence angle, eliminating any statistical variances or deteriorations at the edges of the detectors observed in the measured PSFs. These new entry points were used to calculate a sinogram, which was subsequently reconstructed in the same way as the original study. The image spatial resolution resulting from this idealised situation was 1.10 mm FWHM at the CFOV, an improvement of  $\sim 0.25$  mm compared to the result in figure 6.3.

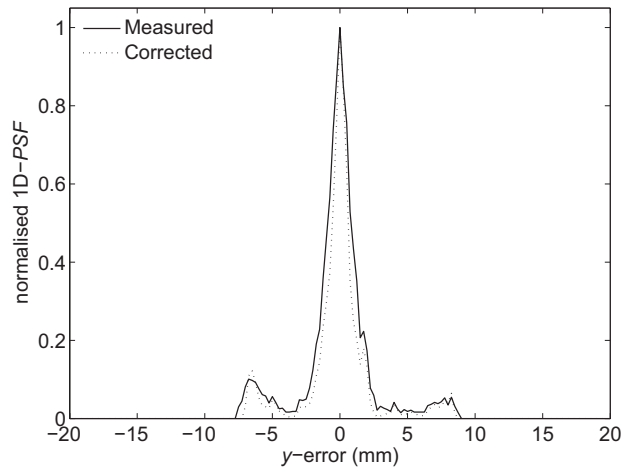
A number of possible causes for this difference can be identified. Firstly, the degradation of the detector spatial resolution at the crystal edges is likely to have an adverse effect on the image resolution. This would suggest that reducing the number of events taking place close to a detector edge, i.e. using detectors with a larger surface area and more light sensors per crystal surface, may result in a relative reduction of these effects. However, this approach would also result in a lower average number of detected scintillation photons per light sensor, reducing the signal-to-noise ratio per pixel, which could result in an overall deterioration of the detector PSF.

A second cause could be the limited statistics in the measured PSFs used in this study. Increasing the number of test events per local PSF may make the deconvolution of the test beam more accurate, possibly leading to an improved image resolution. The present number of events per local PSF was a compromise between statistics and measurement and computation times.

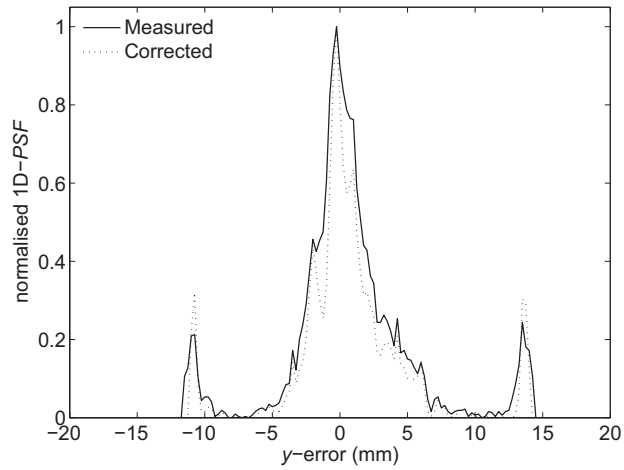
A further improvement of the image quality could be achieved by reducing the ring-shaped artefacts observed in figure 6.5. It was found that a significant fraction of the measured 1D-PSFs, mainly at oblique incidence angles, had artifacts at the edges of the histograms, which may give rise to the observed effects. Examples of such artefacts are shown in figure 6.8, which shows measured (solid lines) and deconvolved (dotted lines) 1D-PSFs obtained at  $y = 0.5$  mm and  $\theta = 0^\circ$  (a), and at  $y = 5.5$  mm and  $\theta = 30^\circ$  (b). The artefacts in the 1D-PSF in (b) at the edges of the histogram are clearly visible.

A cause for these artefacts has thus far not been established. They were also observed in 1D-PSFs obtained by Monte Carlo simulations in GEANT4 [5], making it unlikely that they are the result of a flaw in the experimental procedure. Furthermore, energy thresholding was not found to lead to a reduction of the artefacts. It may be that internal reflections in the crystal cause similarities in the scintillation light distributions at different entry points. In that case, a reduction of the artefacts could be achieved by using crystals with a rough or an absorbing surface. Finally, it may also be that using an alternative event positioning scheme, for example one using neural networks, would result in a reduction of the artefacts.

Further improvements of the image quality obtained with the Micro-Derenzo phantom could be obtained by further optimising the image reconstruction algorithm. For instance, scatter correction, attenuation correction and normalisation of the sinograms have not been performed in this pilot study. Furthermore, using more sophisticated reconstruction techniques such as resolution recovery could lead to an improved image resolution.



(a)



(b)

FIGURE 6.8: Measured (solid lines) and corrected (dotted lines) 1D-PSFs obtained at  $y = 0.5$  mm and  $\theta = 0^\circ$  (a), and at  $y = 5.5$  mm and  $\theta = 30^\circ$  (b).

## 6.5 Conclusions

A pilot study assessing the performance of small-animal PET scanners based on monolithic scintillator detectors was presented in this chapter. The study was based on Monte Carlo simulations using measured detector line spread functions and other detector characteristics as input. The image resolution of a 1-ring system with trapezoidal monolithic detectors was investigated in 2D. A system resolution of  $\sim 1.4$  mm FWHM was found at the centre of the FOV using a  $\varnothing 0.5$  mm point source of  $^{18}\text{F}$ . Very little degradation of the system resolution with increasing radial distance from the CFOV was found, and no anisotropy in the system resolution was observed. This is in agreement with the excellent correction for depth-of-interaction reported previously for these detectors.

Further improvements to the image resolution are likely to be achievable by an adjustment of the detector geometry. This could reduce the relative number of events entering the detectors close to a crystal edge, which exhibit a larger position uncertainty than events entering at the centre of the crystals. An additional improvement of the image resolution is expected with the reduction of artefacts on the measured PSFs, which may be achieved using alternative event positioning algorithms or crystals with a different surface finish.

The favourable geometry of the trapezoidal detectors results in a very high peak sensitivity of 21% at low activity in a 4-ring system, a great improvement compared to the peak sensitivity of 3–4% currently reported for small-animal PET systems. Furthermore, a high peak noise equivalent count rate of 2000 keps was calculated for a mouse phantom in this system, using an energy window of 250–750 keV, a coincidence time window of 5 ns and a detector dead time of 1000 ns. These very high values can lead to a significant improvement of the signal-to-noise ratio of reconstructed images compared to the current standards, improving image quality, and permitting more accurate quantification of tracer concentrations in dynamic small-animal PET studies.



# CHAPTER 7

---

## Conclusion

---

In this chapter I will use the results of the previous chapters to give an answer to the main research question of this thesis. I will repeat the research question here:

*What processes influence the performance of PET detector modules based on monolithic scintillation crystals read out by avalanche photodiode arrays; and in what way do they influence the performance?*

Two methods were used to get to the answer. First, Monte Carlo simulations that model measurements of the spatial resolution, were used to determine the spatial resolution for different sets of parameters (chapter 3). Second, a mathematical model was derived that gives the lower bound on the spatial resolution achievable with the detector (chapters 4 and 5). The two methods complement each other, since each method can overcome some of the limitation of the other.

For the Monte Carlo simulations a simulation programme was written and all relevant parameters were determined either from literature from measurement. The simulations were validated by comparing simulation results to measurement results. The results agreed very well, which suggests that the models and parameters used in the simulations are accurate.

With the simulation programme the influence of the parameters on the spatial resolution can be investigated in the same way as is done in measurements. However, the possibilities for varying parameters (including physics parameters) are much higher in simulations than in measurements. These simulations allow us to investigate the spatial resolution and the results can generally be assumed to give accurate predictions of the actual performance of the detector. However, these simulations also have a disadvantage, since like in measurements the spatial resolution is always a combination of a large number of factors (e.g. there is always the contribution of the position estimation algorithm), which makes it difficult to separate the contributions of each of these factors.

The mathematical model of the lower bound consists of two parts. The first part describes the lower bound of the spatial resolution for a point source of light. The second part describes the influence of the width of the measurement beam, Compton scatter and fluorescence, and the estimation algorithm on the spatial resolution.

When the two are combined, the influence of each of the parameters on the spatial resolution is known. Therefore, the influence of each of the parameters on the spatial resolution can be investigated separately. This leads to a better understanding of the factors determining the spatial resolution. Of course, since some approximations have been made in deriving the model and since the model gives the lower bound on the spatial resolution, it is not to be expected that the model gives an exact prediction of the spatial resolution of the detector obtained in reality.

Furthermore, since the model gives the lower bound on the spatial resolution, it can be used to investigate how well the estimation algorithm is working. Results show that the spatial resolution obtained with the current algorithm is close to the lower bound. Therefore, the estimation algorithm is performing well and the spatial resolution can not be much improved by changing the estimation algorithm.

## 7.1 The parameters and their importance

This section reviews all parameters that influence the spatial resolution and describes how they influence the spatial resolution. The parameters are ordered approximately in order of decreasing importance. As was mentioned in the introduction, I will focus on LSO/LYSO crystals read out by Hamamatsu S8550 APD arrays. Although, the models can also be used for other types of detectors (different crystals, different light detectors, different geometries), the relative importance of the different parameters will probably be different for these detectors. For example, presently the influence of the excess noise factor of the APD array on the spatial resolution is much larger than that of the electronic noise, but should we use a different APD with a much higher dark current and thus much more electronic noise, the electronic noise could become dominant.

**Optical photon transport** It is very difficult to quantify this process, since it depends on the shape and dimensions of the crystal, the type of crystal, the surface treatment of the crystal, the material used to clad the surface of the crystal, the type of optical coupling used between the crystal and the APD arrays, the type of APD arrays, etc. In the model for the lower bound, this process is described by the four dimensional function  $f_i(\underline{x})$  in chapter 4.

Since it is difficult to quantify this parameter, it is also difficult to quantify the influence of this parameter on the spatial resolution. One could say that this is the most important parameter, since monolithic scintillation detectors work by the fact that the light distributions of annihilation photons absorbed at different points inside the crystal differ. When they would not differ, the estimation algorithm could not distinguish between the two points.

For the position estimation, we want the light distribution to change strongly when the absorption point changes. This is reflected in the fact that the information matrix is proportional to the partial derivative of the light distribution ( $f_i(\mathbf{x})$ ) to the position of the source. As for the parameters that influence the photon transport, measurements and simulations show that the surface treatment has little influence on the spatial resolution.

The 10 mm thick crystal with single sided readout and the 20 mm thick crystal with double sided readout have approximately the same spatial resolution. Switching from one APD to two APDs has two effects. First, the amount of detail with which the light distribution is measured increases improving the spatial resolution. Second, the scintillation light is distributed over more pixels causing the signal to noise ratio to decrease and the spatial resolution to decrease. Switching from a 10 mm thick crystal to a 20 mm thick crystal decreases the resolution since the resolution decreases farther away from the APD array. When switching from the 10 mm thick crystal with single sided readout to the 20 mm thick crystal with double sided readout these three contributions cancel each other out.

**Beam width** The measured spatial resolution is affected by the width of the test beam. The measured spatial resolution can never be better than the width of the measurement beam. At the moment the measured spatial resolution is approximately 1.7 mm FWHM with a measurement beam of 1.1 mm FWHM (see chapter 3). The influence of the measurement beam should be removed if one wants to know the spatial resolution of the detector when used in a scanner. But even in a scanner the detector needs to be trained, and during training a beam with finite width is used. When an infinitely large number of training distributions are used, this training beam should not influence the spatial resolution when a very large number of nearest neighbours are used in the estimation algorithm (see chapter 5). However, because of the finite size of the training set, the training beam will also influence the spatial resolution. Simulations predict a spatial resolution of 0.85 mm when a perfect pencil beam is used during training (1000 events per position, see chapter 3). When a training beam of 1.1 mm FWHM is used, simulations predict a spatial resolution of 1.2 mm. This resolution can be improved by either increasing the number of distributions in the reference set or by decreasing the width of the training beam.

**Compton scattering and fluorescence inside the crystal** These influence the spatial resolution in approximately the same way as the beam width does. This can be seen in the fact that in the model for the point spread function, the influence of the beam width and the influence of the Compton scatter and fluorescence are combined in one contribution (see chapter 5). Therefore, the same conclusions that were drawn for the influence of beam width also hold for the contribution of Compton scatter and fluorescence. However, since the distribution of this contribution is sharply peaked with strong tails, this contribution mainly influences the tails of the measured LSF. Therefore, the FWHM is not that strongly influenced by this contribution, but the FWTM is.

This contribution can be influenced by changing the scintillator that is employed in the detector. Ideally one would like to have a scintillator in which only

photo-electric effect occurs. Therefore, one would like to have a scintillator with high  $Z$  and high density. However, the scintillator material will also need to have a high light yield and good energy resolution (see below).

**Light yield of the scintillator** As was shown in chapter 4, the light yield is one of the most important terms in the lower bound of the spatial resolution. However, the light yield can only be influenced by changing the scintillator. There are some differences in light yield of LSO/LYSO between different manufacturers, but these differences are relatively small and could also be caused by increased absorption which influences photon transport. Scintillators that are very interesting in this respect are lanthanum bromide ( $\text{LaBr}_3$ ) and lanthanum chloride ( $\text{LaCl}_3$ ), which have a much higher light yield than LSO/LYSO (70,000 photons per MeV). However, the density and  $Z$ -value of these scintillators are much lower, which will decrease the efficiency of the detectors (for a given thickness) and increases the contribution of Compton scatter and fluorescence.

**Quantum efficiency, gain and excess noise factor of the APD array** The external quantum efficiency of the APD array is made up of two contributions: reflectivity and the internal quantum efficiency. Since the reflectivity influences the photon transport, it is difficult to quantify this contribution. However, an increase in the reflectivity, will increase the number of interactions the optical photons undergo and will therefore decrease the amount of information in the optical photons. The internal quantum efficiency is approximately one for the wavelengths emitted by LSO/LYSO and therefore does not deteriorate the spatial resolution. For scintillators that emit at lower wavelengths (such as  $\text{LaBr}_3$  and  $\text{LaCl}_3$ ), the internal quantum efficiency will play an important role.

The influence of the gain is directly coupled to that of the electronic noise: the only reason to have amplification in the APD array is to reduce the influence of noise. This is reflected in the lower bound (see equation 4.16), where the spatial resolution increases as  $\sigma_e^2/\bar{M}$  increases. Of all the noise contributions, excess noise is one of the most important (see chapter 4). Unfortunately, it is very difficult to improve on the excess noise factor without switching to a light detector that uses a completely different gain mechanism.

**Electronic noise** In the detector investigated in this thesis electronic noise is not the main noise contribution. Contributions from excess noise and light yield are much larger. However, when the electronic noise increases the spatial resolution quickly deteriorates. Therefore, the electronic noise should not exceed the current level.

**Incident angle** Since this type of detector can implicitly determine the depth of the interaction, it does not suffer from the parallax error. This has been shown in measurements and simulations (see chapter 3).

**Intrinsic energy resolution** Since the signals in each of the APD channels are correlated (a higher number of scintillation photons causes a higher signal in each

of the channels), the energy resolution has hardly any influence on the spatial resolution. However, the energy resolution and timing resolution do depend on the intrinsic energy resolution.

## 7.2 Conclusion

The models derived in this thesis provide a much better understanding of the operation principle and the performance of monolithic scintillation detectors than there was previously. All contributions to the spatial resolution have been identified and their influence on the spatial resolution can be quantified. Of course, the model has some limitations. For example, the model for the line spread function is only valid in the center of the detector. However, for understanding the influence of the parameters on the spatial resolution, it is adequate enough.

In this thesis, the modelling was done for the spatial resolution of a novel type of PET detector, but the methods used can easily be adapted to model radiation detectors used for other applications and also for other performance characteristics than the spatial resolution. Especially for detectors that estimate the position of an ionizing particle from the light distribution of a scintillating/fluorescing material, the amount of modifications needed are probably very small. I hope this work will motivate and help others to model their detectors.



# APPENDIX A

---

## The lower bound on the spatial resolution: geometry<sup>1</sup>

---

**We are investigating the possibility of using monolithic scintillator blocks as detectors for small animal positron emission tomography (PET). These detectors consist of several cm<sup>3</sup> of scintillating material, read out by one or more avalanche photo-diode (APD) arrays. The entry point of an incoming gamma photon is estimated from the distribution of the scintillation light over the APD pixels. To optimize the detector design, the influence of different design parameters is investigated using Geant4 simulations. To make it possible to study the influence of individual design parameters on the intrinsic spatial resolution of the detector, the use of a performance measure is proposed that is independent of the algorithm used to estimate the entry point, namely the Cramér-Rao lower bound on the estimation of the coordinates of a point source of light inside the crystal. To illustrate the use of this method, the influence of optical transport inside the detector is investigated for different detector designs, surface finishes and APD pixel sizes. A comparison with resolutions obtained from simulations involving beams of 511 keV annihilation photons indicates that this approach gives valid results.**

### A.1 Introduction

In recent years there has been an increase of interest in small animal positron emission tomography (PET). Small animal PET requires a high spatial resolution and, especially when dynamic studies are to be performed, a high sensitiv-

---

<sup>1</sup>The model derived in this appendix has been superseded by the model derived in chapter 4. Also the optical simulation model that is used, is much simpler than that derived in chapter 3 and used in chapter 4. However, some of the results in this appendix are not presented in the other chapters. Therefore, this article has been included in the appendix. This chapter has been published as: D. J. van der Laan and M. C. Maas and D. R. Schaart, P. Bruyndonckx, S. Léonard and C. W. E. van Eijk, 'Using Cramér-Rao theory combined with Monte Carlo simulations for the optimization of monolithic scintillator PET detectors', *IEEE Transactions on Nuclear Science* 53 (2006), no. 3, 1063–1070.

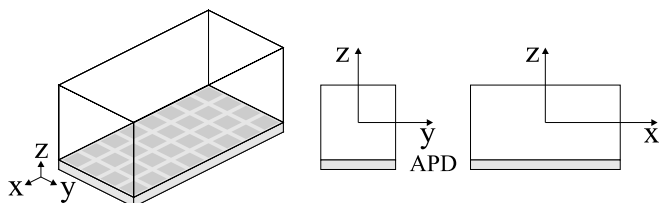
ity [13]. In order to achieve the required resolution, most current designs use arrays of small scintillation crystals coupled to position-sensitive photomultiplier tubes (PMTs). Although in principle the resolution can be increased in this design by decreasing the dimensions of the crystals, much sensitivity is lost because of the dead space between the crystals occupied by reflective material for optical separation. Additional dead space may exist between the detector modules, which may, for example, be dictated by the relatively large size of the position-sensitive photomultiplier tubes. Finally, increasing the length of the crystals in order to increase the sensitivity requires correction for the depth-of-interaction (DOI), since otherwise the resulting parallax error will decrease the resolution outside the center of the scanner.

Monolithic scintillation detectors can avoid these problems. These detectors consist of a continuous scintillation crystal read out by position sensitive photo-detectors. The Philips CPET system is, for example, based on this type of detector, although without DOI correction [4]. Designs with DOI correction have also been investigated [19, 16, 6], but these are either too complicated or have insufficient spatial resolution for small animal PET.

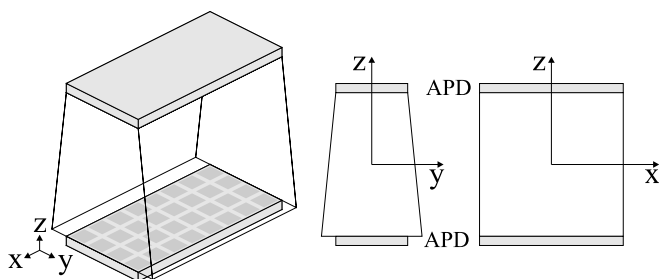
The detectors we are investigating consist of several cubic centimeters of scintillating material coupled on one or more sides to avalanche photo-diode (APD) arrays. Three examples of this detector are shown in Fig. A.1. The coordinates of the entry point of an incoming gamma photon are estimated from the light distribution on the pixels of the APD arrays. This can be done by either a statistical method or neural networks. Before estimation can take place, the algorithm is first trained using measured light distributions produced by annihilation photons with known entry points.

Compared to detectors using arrays of small crystals, the proposed monolithic scintillation detectors have several advantages. First of all, the detection efficiency is increased because the dead space between the crystals in a crystal array is avoided and because the dead space between the detector modules can be minimized due to the small size of the APD arrays. They are also easier to manufacture. Furthermore, integration with MRI devices may become possible because of the use of APD arrays instead of PMTs.

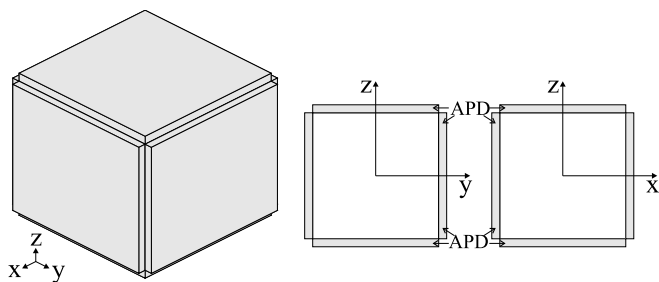
Measurements on this type of detector show that the intrinsic detector resolution is comparable to that of detectors using arrays of small crystals [42, 10, 11]. However, the resolution obtained in measurements is always determined by a large number of factors, such as the shape of the monolithic scintillator, the crystal surface finish, the width of the beam used in the measurements, electronic noise and the algorithm used to estimate the coordinates of the entry point. This makes it difficult to determine the individual effect of each of these factors on the resolution. Understanding these influences can make optimization of the design more efficient. Monte Carlo simulations mimicking the measurements can help, since certain parameters can be varied more easily in a simulation than in an experiment. Furthermore, influences that are unavoidable in experiments, such as electronic noise, can even be left out completely if one wishes to study solely the effect of other parameters. However, even in such simulations the resolution still depends on the estimation algorithm used. When for example a better spatial resolution is found for a crystal whose surfaces are polished than for an



(a)  $20 \times 10 \times 10 \text{ mm}^3$



(b)  $20 \times 14(10) \times 20 \text{ mm}^3$



(c)  $20 \times 20 \times 20 \text{ mm}^3$

FIGURE A.1: Three examples of detector design. A  $20 \times 10 \times 10 \text{ mm}^3$  LSO crystal read out on one side by an APD array, a 20 mm thick tapered LSO crystal read out by two APD arrays, and a  $20 \times 20 \times 20 \text{ mm}^3$  LSO crystal read out on six sides by single APDs.

unpolished crystal, it is not known if this is because this specific estimation algorithm works better for crystals with polished surfaces or that the polished crystal is inherently better. Perhaps the detector would perform even better with an unpolished crystal with a different estimation algorithm.

In this paper we propose the use of a performance measure, that is independent of the estimation algorithm, namely the Cramér-Rao lower bound on the estimation of the coordinates of a point source of light inside the crystal. Since this measure gives the lower bound on the variance in the estimated coordinates for any unbiased estimation algorithm, it does not depend on the estimation algorithm used. This makes it possible to better understand the influence of different design parameters on the resolution. After introducing the Cramér-Rao lower bound, we will illustrate it with results obtained from simulations in which the geometry, surface finish and pixel size is varied. Finally, we will compare these results to actual resolutions obtained using a simple estimation algorithm on simulated data.

## A.2 Cramér-Rao lower bound

In the monolithic scintillator detectors the entry point of an impinging annihilation photon is estimated from the distribution of the scintillation light over the pixels of the APD arrays using a learning algorithm (for an example see section A.3.2) that has been trained using light distributions produced by annihilation photons with known entry points. By estimating the entry point of the annihilation photon the DOI is intrinsically corrected for.

When the annihilation photon deposits its energy in one point inside the crystal, the light distribution is determined by the  $x$ ,  $y$  and  $z$ -coordinate of this interaction point. In that case, the estimation algorithm can be considered to estimate the  $x$ ,  $y$  and  $z$ -coordinate of the interaction point, from which the entry point is calculated using the angle of incidence. In a PET scanner this angle may be derived from the positions of the two detectors firing in coincidence, as is explained in more detail in [11]. In reality, the energy of an annihilation photon will not always be deposited in a single point, due to the occurrence of Compton scattering, X-ray fluorescence, etc. The estimation algorithm will still estimate one entry point, which can be considered to be based on a kind of average interaction point. Even though there may be some blurring in this case, the estimation of entry point can again be considered to be based on the estimation of an interaction point. Therefore, it seems reasonable to assume that the ability to estimate the  $x$ ,  $y$  and  $z$ -coordinates of single point sources of light is a good indicator of the ability to estimate the entry points of realistic events.

For the case of a single point source of light, it is possible to derive the Cramér-Rao lower bound on the estimate of its coordinates. This lower bound equals the smallest value of the standard deviation that any unbiased estimator of the parameters of interest (in this case the coordinates of the point source) can achieve, given a statistical model of the observations (in this case the simulated light distributions). In the following derivation of the statistical model, it is assumed that the annihilation photon deposits all of its energy at position  $\underline{x} =$

$(x, y, z)^T$  inside the crystal. The number of optical photons emitted is assumed to follow a Poisson distribution with mean  $N$ .  $N$  is the light yield of the scintillator at 511 keV.

Assume that  $P$  APD pixels detect the optical photons emitted by the point source, and that pixel  $i$  detects a fraction  $f_i(\underline{x})$  of the optical photons. Then, the number of detected optical photons on a pixel will follow a Poisson distribution and be independent of the number detected on the other pixels. The probability of detecting  $n_i$  photons on pixel  $i$  is therefore given by

$$p_i(n_i|\underline{x}, N, \eta) = \frac{(N \cdot \eta \cdot f_i(\underline{x}))^{n_i}}{n_i!} \cdot e^{-N \cdot \eta \cdot f_i(\underline{x})}, \quad (\text{A.1})$$

where  $\eta$  is the quantum efficiency of the APD array. The likelihood of the pixels detecting  $\underline{n} = (n_1, n_2, \dots, n_P)^T$  photons is given by

$$L(\underline{n}|\underline{x}, N, \eta) = \prod_{i=1}^P p_i(n_i|\underline{x}, N, \eta). \quad (\text{A.2})$$

Using this likelihood function the information matrix is defined as [73]

$$\mathbf{M} = -\text{E}[\partial^2 \ln L(\underline{n}|\underline{x}, N, \eta)/\partial \underline{x}^2]. \quad (\text{A.3})$$

The Cramér-Rao inequality, which gives the lower bound on the covariance matrix of an unbiased estimator, then states that

$$\text{cov}(\hat{\underline{x}}, \hat{\underline{x}}) \geq \mathbf{M}^{-1}, \quad (\text{A.4})$$

where  $\hat{\underline{x}}$  is the estimator of the coordinate  $\underline{x}$  [73]. The lower bound on the variances on  $\hat{x}$ ,  $\hat{y}$  and  $\hat{z}$  are given by the three diagonal elements of this matrix.

Using the likelihood function as defined in (A.2) and (A.1), the elements of the information matrix become

$$M_{vw} = N \cdot \eta \cdot \sum_{i=1}^P \frac{1}{f_i(\underline{x})} \frac{\partial f_i(\underline{x})}{\partial v} \frac{\partial f_i(\underline{x})}{\partial w}, \quad (\text{A.5})$$

with  $v$  and  $w$  equal to  $x$ ,  $y$ , or  $z$ . From this equation follows that

$$\mathbf{M}^{-1} \propto \frac{1}{N \cdot \eta}, \quad (\text{A.6})$$

which shows that the variance is inversely proportional to the number of photons emitted and the quantum efficiency.

To evaluate these expressions for a given point  $\underline{x}$  in the crystal, the expectation value of the fraction of photons that reaches each pixel,  $f_i(\underline{x})$  and the first derivative of this fraction to each of the coordinates must be known. Both can be estimated using optical Monte Carlo simulations. When a large number of optical photons are tracked through the detector after emission from the point source, the expectation value of the detected fraction can be calculated for each pixel by dividing the number of detected photons by the total number of emitted

photons. The partial derivatives of this fraction can be determined by doing the same simulation for points located  $\pm h$  in the  $x$ ,  $y$ , and  $z$  direction from  $(x, y, z)$ . The derivative is then found by numerical derivation. For example, the partial derivative to  $x$  is estimated by

$$\left. \frac{\partial f_i(x, y, z)}{\partial x} \right|_{x, y, z} = \frac{f_i(x + h, y, z) - f_i(x - h, y, z)}{2h} + O(h^2). \quad (\text{A.7})$$

The partial derivatives to  $y$  and  $z$  can be calculated in a similar way.

Although it is in theory possible to derive the lower bound on the estimation of the entry point of an annihilation photon, thus taking Compton scatter and X-ray fluorescence into account, this is not practical. The likelihood has to be derived directly from simulations, since the number of photons detected by the APD pixels will no longer be Poisson distributed and independent. This would take a huge amount of simulation time and would make it necessary to do all calculations numerically thereby losing the clarity of the method.

The Cramér-Rao theory gives the lower bound on the standard deviation in each of the coordinates. In case of perpendicular incidence of the annihilation photon, only the lower bound on the  $x$  and  $y$ -coordinate are of importance. However, when the photon has an incident angle, the lower bound on the  $z$ -coordinate determines how well the parallax error can be avoided. It appears that the results for the lower bound on the standard deviation of the  $x$ -coordinate are often representative for the other coordinates as well, and therefore we will primarily focus on this coordinate. However, when the lower bound on any of the other two coordinates shows interesting behavior, this will of course be discussed.

## A.3 Methods

### A.3.1 Cramér-Rao simulations

The Cramér-Rao lower bound has been calculated for a three-dimensional grid of points in a number of different geometries and for several different surface finishes. The simulations needed to calculate the functions  $f_i(x, y, z)$  have been performed using the Monte Carlo code Geant4 [5]. With this code it is possible to simulate the transport and interactions of the gamma photons, the scintillation process, and the transport of the optical photons, but for the calculation of the Cramér-Rao lower bound only the transport of optical photons is needed.

In order to reduce computation times, use has been made of symmetry in the detector where possible. For example, all geometries investigated are symmetrical in the  $x$  and  $y$ -direction. The lower bound therefore needs to be calculated for only one quadrant of the crystal. By mirroring these results the lower bound for the remainder of the crystal is found. For every point source position 1.7 million photons were tracked, and a value of 0.5 mm was chosen for  $h$  to calculate the derivative using (A.7). This value is a compromise between the bias (for large  $h$ ) and the standard deviation (for small  $h$ ) in the estimate of the derivative and was determined from preliminary simulations.

Five different geometries have been used in the simulations. In the description of these geometries, the crystal surface facing the center of the scanner is called the front surface.

1. A  $20 \times 10 \times 10 \text{ mm}^3$  LSO: $\text{Ce}^{3+}$  crystal with a front and back surface of  $20 \text{ mm} \times 10 \text{ mm}$  read out on the back side by an APD array. This design is shown in Fig. A.1(a).
2. A  $20 \times 10 \times 20 \text{ mm}^3$  LSO: $\text{Ce}^{3+}$  crystal with a front and back surface of  $20 \text{ mm} \times 10 \text{ mm}$  read out on the back and front side by an APD array. The increased thickness of the crystal in this geometry increases the probability of an interaction of an 511 keV annihilation photon from 58% to 83% [81].
3. A 20 mm thick tapered LSO: $\text{Ce}^{3+}$  crystal, with a  $20 \text{ mm} \times 10 \text{ mm}$  front surface and a  $20 \text{ mm} \times 14 \text{ mm}$  back surface, see Fig. A.1b. Both surfaces are read out by an APD array. Because of the taper, this shape eliminates almost all dead space between the crystals if they are placed in a ring. The dimensions of this geometry will be written as  $20 \times 14(10) \times 20 \text{ mm}^3$ .
4. A  $20 \times 10 \times 20 \text{ mm}^3$  LaBr<sub>3</sub>: $\text{Ce}^{3+}$  crystal read out on the back and front side by an APD array. An advantage of LaBr<sub>3</sub> is the high light yield (61,000 photons/MeV) compared to LSO (26,000 photons/MeV) [81], since, as follows from (A.6), the lower bound on the standard deviations is inversely proportional to the square root of the number of emitted photons per event. However, the density is smaller than that of LSO ( $5.3 \text{ g}\cdot\text{cm}^{-3}$  versus  $7.4 \text{ g}\cdot\text{cm}^{-3}$  for LSO) causing the interaction probability of an annihilation photon to be only 61% [81].
5. A  $20 \times 20 \times 20 \text{ mm}^3$  LSO: $\text{Ce}^{3+}$  crystal read out on all sides by single-pixel APDs. This design is shown in Fig. A.1c. LeBlanc and Thompson [36] have already reported on simulations of a similar design. The APDs have a surface of  $20 \text{ mm} \times 20 \text{ mm}$ . The active area is  $16 \text{ mm} \times 16 \text{ mm}$ , which leaves a gap of 2 mm around the edge. The timing and energy resolution could benefit from the fact that almost all light is collected in this design. Since there are no reflections inside the crystal for this design (see the discussion of the optical model below), the Cramér-Rao lower bound can be calculated from the solid angle of the APDs seen from the point source position. The solid angles and the lower bound are therefore calculated numerically for this design.

The model that has been used to simulate the optical interactions at surfaces is the UNIFIED model, which has been described by Levin and Moisan [37]. This model is implemented in Geant4 [1]. In this model a surface consists of small micro-facets, whose normals have a random angle,  $\alpha$ , with the overall surface normal. The angles follow a normal distribution with an expectation value of zero and a standard deviation of  $\sigma_\alpha$ , which is therefore a measure of surface roughness. In our case, the surface is covered on the outside by a reflective cladding with a refractive index that is equal to that of air. If the cladding is reflective, it reflects the optical photons diffusely.

A number of different surface finishes were investigated. We simulated two types of polished surfaces. One was clad in Teflon (reflectivity 95%) and one in an absorbing material (reflectivity 0%). The same types of cladding were also used for a rough surface. The polished surface was modelled with a  $\sigma_\alpha$  of  $0.1^\circ$  and the rough surface with a  $\sigma_\alpha$  of  $6.0^\circ$ . These values were taken from Moisan et al. [54]. As an extreme case we also studied a specularly reflecting surface. The specularly reflecting surface reflects 100% of the optical photons with the angle of reflection equal to the angle of incidence.

In the Cramér-Rao simulations only the refractive indices and the light yield of the scintillating materials are needed. For LSO these are 1.82 and 26,000 photons/MeV respectively and for LaBr<sub>3</sub> 1.88 and 61,000 photons/MeV [81, 9]. The optical coupling between the APD arrays and the crystal has been assumed to be perfect. This means that all optical photons reaching the crystal-APD surface are absorbed by the APD array. Furthermore, the quantum efficiency of the APD array has been assumed to be equal to one, since at the moment we are only interested in the effect of the light transport on the resolution. Furthermore, the quantum efficiency has no influence when comparing results from one scintillator to each other, since it is then only a constant factor according to (A.6).

In our measurements we have been using the Hamamatsu S8550 APD array [42]. The size of the pixels on this array is  $1.6 \text{ mm} \times 1.6 \text{ mm}$  and the center to center distance between the pixels is 2.3 mm in both directions. All of the results presented in this paper for the different surface finishes and for the different detector geometries are based on this APD array, except for the  $20 \times 20 \times 20 \text{ mm}^3$  crystal that is read out by six single APDs. In order to investigate the influence of the APD pixel size on the detector performance, the lower bound for the  $20 \times 10 \times 20 \text{ mm}^3$  LSO crystal was additionally calculated for four different pixel sizes. Besides the aforementioned pixel size the following sizes were investigated:  $1.1 \text{ mm} \times 1.1 \text{ mm}$  with a pitch of 1.8 mm,  $3.9 \text{ mm} \times 1.6 \text{ mm}$  with a pitch of 4.6 mm in the  $x$ -direction and 2.3 mm in the  $y$ -direction, and  $3.9 \text{ mm} \times 3.9 \text{ mm}$  with a pitch of 4.6 mm. The numbers of pixels on these arrays are  $10 \times 5$ ,  $4 \times 4$ , and  $4 \times 2$  respectively. In all cases, the pixels are separated by a 0.7 mm dead region.

### A.3.2 Simulations using beams

The results obtained for the Cramér-Rao lower bound were compared to results from simulations that resemble the measurements done in our group [42] and in Brussels [10, 11]. In these simulations a beam of 511 keV gamma photons having a diameter of zero is stepped in steps of  $250 \mu\text{m}$  over the center of the crystal in the  $x$  and  $y$ -direction. The number of photons detected by each APD pixel was recorded for 400 events for every beam position. Electronic noise was not modeled.

In order to calculate the spatial resolution the entry point of each of the simulated distributions is estimated using the remainder of the distributions as training data for our estimation algorithm. The distribution for which the entry point has to be estimated is compared using least squares to each of the distributions in the training set. The entry point of the distribution in the training

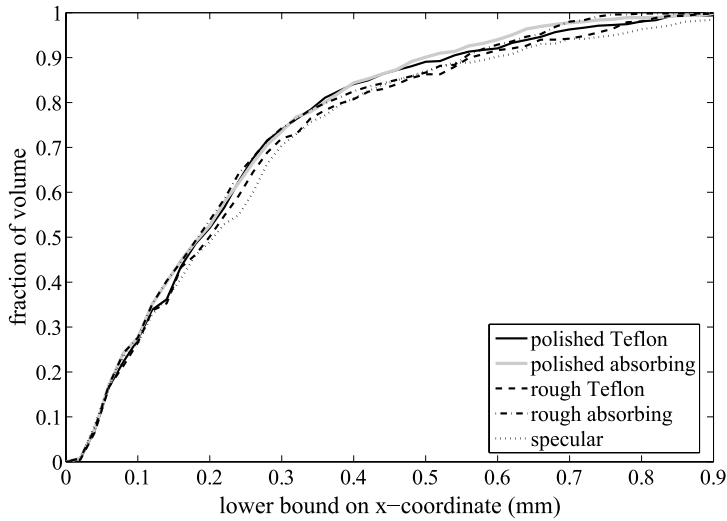


FIGURE A.2: *Cumulative distribution of the Cramér-Rao lower bound on the  $x$ -coordinate inside the  $20 \times 10 \times 20 \text{ mm}^3$  LSO crystal for different surface finishes. The  $y$ -axis shows the fraction of the crystal volume for which the lower bound is smaller than the value given on the  $x$ -axis.*

set giving the smallest least squares value is used as the estimate of the entry point. The full width at half maximum (FWHM) and the full width at tenth maximum (FWTM) of the histogram of all the errors, defined as the distances between the true and estimated entry points, of the scan are used as a spatial resolution measure. More information on the estimation algorithm and beam measurements has been presented elsewhere [42].

## A.4 Results and Discussion

### A.4.1 Cramér-Rao results

#### Surface finish

Fig. A.2 shows the cumulative distribution of the Cramér-Rao lower bound on the  $x$ -coordinate inside the  $20 \times 10 \times 20 \text{ mm}^3$  LSO crystal for the different surface finishes described in the previous section. For example, more than 80% of the crystal volume has a lower bound smaller than 0.4 mm for all surface finishes. The five surface finishes show little performance difference for the lower bound on the  $x$ -coordinate. Similar results were obtained for the  $y$ -coordinate. The lower bound on the  $z$ -coordinate is slightly higher for the specularly reflecting surface than for the other four, more realistic, surface finishes. The surface finish, therefore, seems to have little to no influence on the spatial resolution of the detectors. The polished Teflon clad surface finish is, therefore, used in

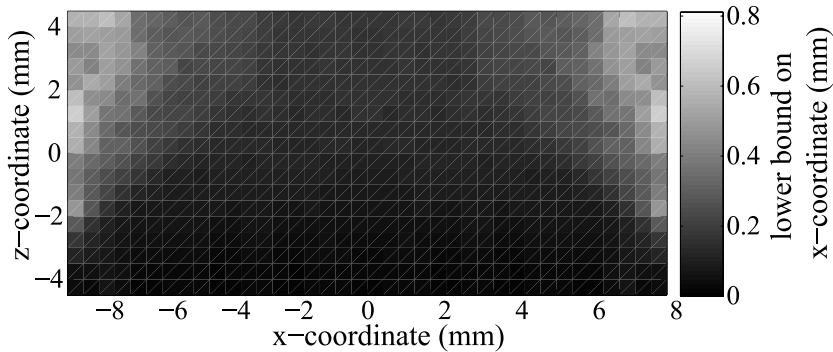


FIGURE A.3: *The lower bound on the  $x$ -coordinate as a function of position in the  $x$ - $z$  plane in the center of the crystal for the  $20 \times 10 \times 10$  mm<sup>3</sup> LSO crystal with polished surfaces and wrapped in Teflon.*

the comparison of the different detector geometries. This is motivated by the fact that the use of a Teflon wrapped crystal will yield larger and more constant signal amplitudes, which may improve the timing characteristics and the energy resolution of the detector.

#### Crystal geometry

Fig. A.3 and Fig. A.4a show the lower bound on the  $x$ -coordinate as a function of position in a plane in the center of the crystal for the  $20 \times 10 \times 10$  mm<sup>3</sup> and the  $20 \times 10 \times 20$  mm<sup>3</sup> LSO crystal respectively. From these figures it can be seen that the lower bound increases further away from the APD array and near the edges of the crystal. Therefore, the thickness of the  $20 \times 10 \times 10$  mm<sup>3</sup> can not be increased in order to increase the sensitivity without degrading the resolution. This is enhanced by the fact that most interactions occur in the front part of the crystal. For example, in a 20 mm thick LSO crystal approximately 70% of the annihilation photons that interact inside the crystal interact in the first 10 mm. Placing the APD array on the front side of the crystal could help in this respect. Another solution might be the use of double-sided readout, as can be seen in Fig. A.4a, which allows one to increase the crystal size to  $20 \times 10 \times 20$  mm<sup>3</sup> without sacrificing position resolution.

The distributions of the Cramér-Rao lower bound on the  $x$ ,  $y$  and  $z$ -coordinate in the five detector geometries with polished surfaces clad in Teflon are shown in Fig. A.5 and Fig. A.6. When comparing figures A.5a and A.5b, it can be seen that the lower bound is higher in  $y$ -direction for all geometries except the  $20 \times 20 \times 20$  mm<sup>3</sup> crystal. This is caused by the fact that in these geometries the crystals are twice as long in the  $x$ -direction than in the  $y$ -direction, while the lower bound is higher near the edges. As can be seen from Fig. A.6, for the designs that are read out by two APD arrays the lower bound in the  $z$ -direction is slightly lower than in the other two directions. Compared to the other designs, the design read out by only one APD array on the back performs worst in the  $z$ -direction.

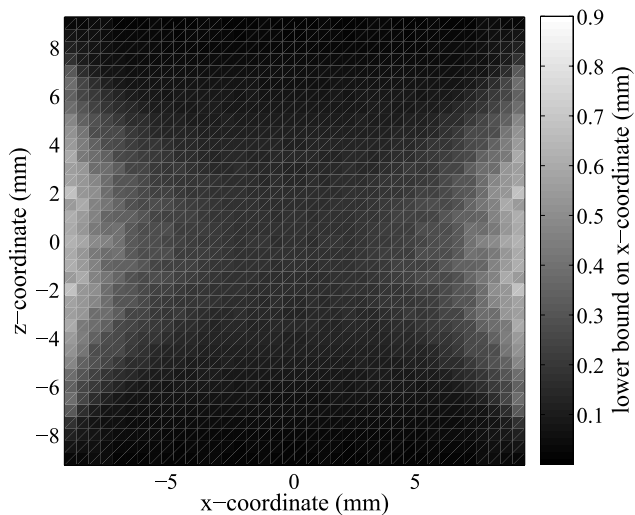
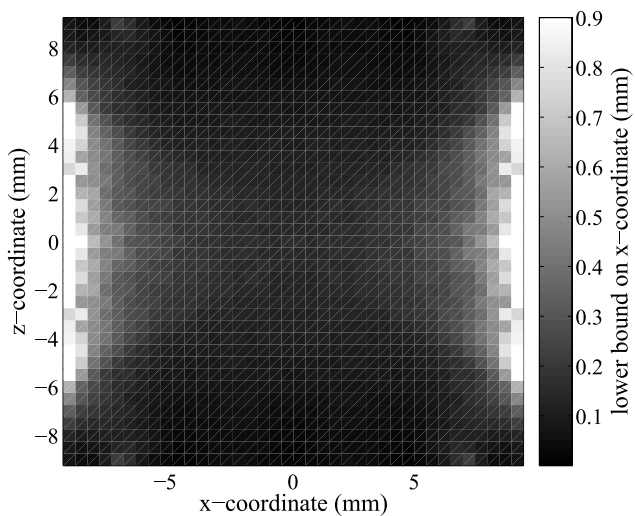
(a)  $1.6 \text{ mm} \times 1.6 \text{ mm}$ (b)  $3.9 \text{ mm} \times 3.9 \text{ mm}$ 

FIGURE A.4: The lower bound on the x-coordinate as a function of position in the x-z plane in the center of the  $20 \times 10 \times 20 \text{ mm}^3$  LSO crystal clad in Teflon for two pixel sizes.

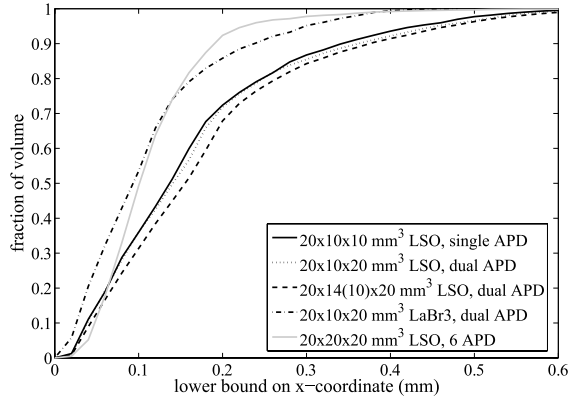
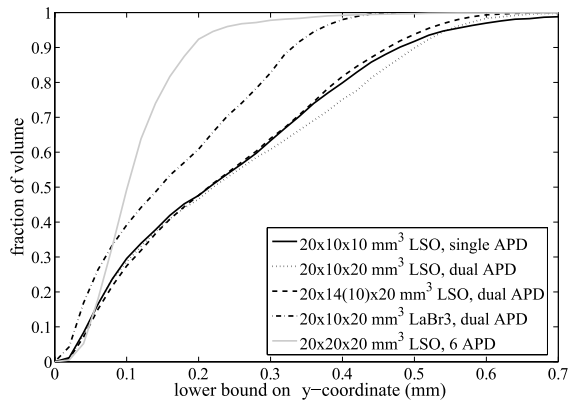
(a)  $x$ (b)  $y$ 

FIGURE A.5: Cumulative distribution of the Cramér-Rao lower bound on the  $x$  and  $y$ -coordinate for the five detector geometries. The  $y$ -axis shows the fraction of the crystal volume for which the lower bound is smaller than the value given on the  $x$ -axis.

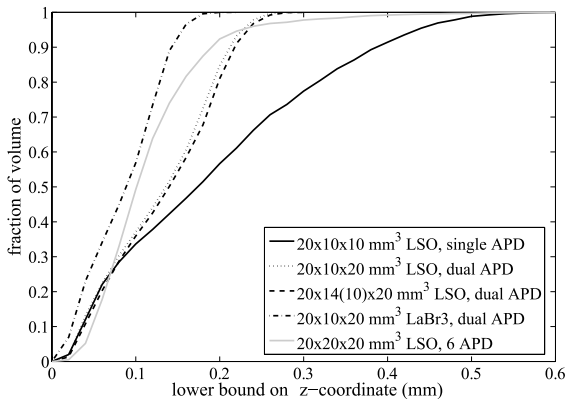


FIGURE A.6: *Cumulative distribution of the Cramér-Rao lower bound on the  $z$ -coordinate for the five detector geometries. The  $y$ -axis shows the fraction of the crystal volume for which the lower bound is smaller than the value given on the  $x$ -axis.*

This is probably because the other designs have two APD arrays opposite each other in the  $z$ -direction making a better estimation of the  $z$ -coordinate possible.

The  $20 \times 10 \times 10 \text{ mm}^3$  and the  $20 \times 10 \times 20 \text{ mm}^3$  crystal perform approximately equally well when looking at the  $x$ -coordinate. The same is true for the  $y$ -coordinate, but the  $20 \times 10 \times 20 \text{ mm}^3$  crystal performs significantly better when estimating the  $z$ -coordinate for the reason mentioned in the preceding paragraph.

Furthermore, the  $20 \times 10 \times 20 \text{ mm}^3$  and the  $20 \times 14(10) \times 20 \text{ mm}^3$  crystal show similar performance. While the tapered crystal has a slightly higher larger bound on the  $x$ -coordinate, it has a slightly smaller lower bound on the  $y$ -coordinate. Therefore, adding a taper to the crystal hardly influences the resolution, in spite of the fact that the back surface of the tapered crystal is significantly larger than the APD array. This is probably caused by the fact that the part of the crystal that sticks out is very close to the APD array, while the resolution improves closer to the APD array as is shown in Fig. A.3 and Fig. A.4. Another factor could be that there is less internal trapping of light, since the taper reflects light towards the back side of the crystal.

Concerning the  $\text{LaBr}_3$  crystal, one would expect the lower bound to be approximately a factor  $\sqrt{61,000/26,000}$  lower (see (A.6)) than that of the corresponding LSO crystal, because all relevant parameters except the light yield are approximately the same. This is indeed the case. The  $20 \times 10 \times 20 \text{ mm}^3$   $\text{LaBr}_3$  crystal and the  $20 \times 20 \times 20 \text{ mm}^3$  LSO crystal read out on all six sides perform approximately equally well for the  $x$ -coordinate, but for the  $y$ -coordinate the performance of the  $\text{LaBr}_3$  crystal is less good. Both designs, however, perform better than the other designs based on LSO. Close to the APD arrays, the  $\text{LaBr}_3$  crystal performs somewhat better than the  $20 \times 20 \times 20 \text{ mm}^3$  crystal, because the small APD pixel size of the 32 pixel array in the  $\text{LaBr}_3$  design results in a better estimation close to the APD array.

### APD pixel size

Fig. A.7 shows the distribution of the lower bound on the  $x$  and  $z$ -coordinate in the  $20 \times 10 \times 20$  mm<sup>3</sup> polished Teflon clad LSO crystal for various APD pixel sizes. When estimating the  $x$ -coordinate the smaller pixel sizes perform better, while the larger pixel sizes perform better when estimating the  $z$ -coordinate. This can probably be explained by assuming that the performance for different pixel sizes is a balance between capturing the shape of the light distribution (small pixel sizes) and good statistics (large pixel sizes, resulting in less dead space). When estimating the  $x$ -coordinate the shape of the light distribution is important, so smaller pixel sizes perform better. The  $z$ -coordinate can largely be determined by the ratio of the amount light detected on the front surface and that detected on the back surface. This ratio is determined more accurately using larger pixel sizes, because large pixels have less dead space between them. For example, the  $1.6 \text{ mm} \times 1.6 \text{ mm}$  pixels have 60% dead space, while the  $3.9 \text{ mm} \times 3.9 \text{ mm}$  pixels have only 40% dead space.

Since Fig. A.7 does not show in which part of the crystal the resolution changes as a result of changing the pixel size, Fig. A.4 shows the lower bounds on the  $x$ -coordinate in the  $x$ - $z$  plane in the center of the crystal for a pixel size of  $1.6 \text{ mm} \times 1.6 \text{ mm}$  and for a pixel size of  $3.9 \text{ mm} \times 3.9 \text{ mm}$ . In the center of the crystal and near the APD arrays the lower bounds are approximately equal in both cases. The lower bound increases especially near the edges of the crystal if the pixel size is increased. A possible explanation might be that for a point source of optical photons near the edge of the crystal most of the light will be detected by a small number of pixels near the edge. For larger pixels this number will be smaller, making the determination of the position more difficult.

### A.4.2 Comparison with beam simulations

In order to check whether the results for the lower bounds can indeed be used as a meaningful measure of the performance of a detector, a comparison has been made with resolutions obtained from simulations using perfect beams. These simulations mimic the measurements that are currently being performed within our group [42] and Brussels [10, 11], with the difference that in the simulations a beam width of zero is assumed and electronic noise is not modeled. Simulations with a finite beam width show that the differences between the results presented here and the measurements, are mainly due to the difference in beam width.

Because the Cramér-Rao results describe the detector's ability to estimate the coordinates of a point source of light at a given location inside the crystal, and the beam results describe the detector's ability to estimate the entry point of an impinging gamma photon, the absolute values of both types of results cannot be compared directly. Both types of results must, however, show similar trends if the Cramér-Rao results are to be used as a performance measure for optimizing the detector geometry.

Table A.1 shows the resolutions obtained from the beam simulations for the surface finishes investigated. The standard deviations on the FWHM and the FWTM are estimated to be approximately 0.04 mm and 0.06 mm respectively. The results show no significant differences between the different surface finishes.

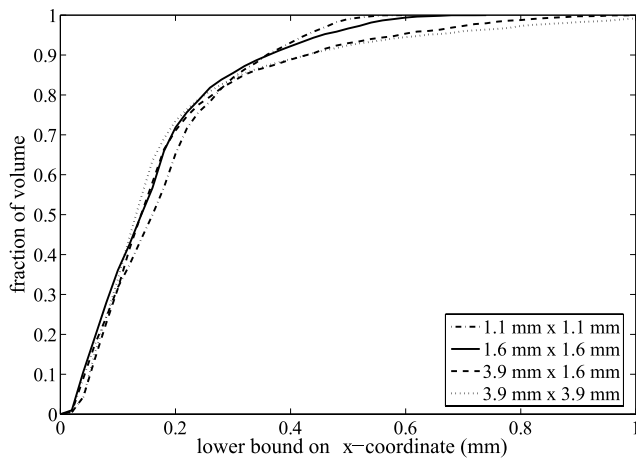
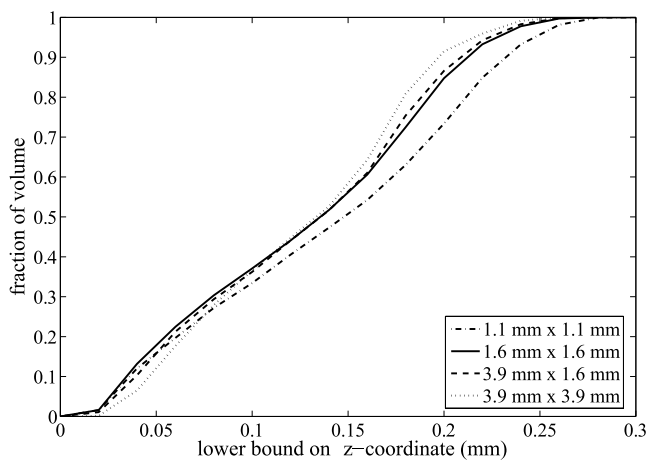
(a)  $x$ (b)  $z$ 

FIGURE A.7: Cumulative distribution of the Cramér-Rao lower bound on the  $x$ -coordinate for various APD pixel sizes. The  $y$ -axis shows the fraction of the crystal volume for which the lower bound is smaller than the value given on the  $x$ -axis.

TABLE A.1: *Simulation results for the spatial resolution of the  $20\times 10\times 20$  mm<sup>3</sup> LSO crystal read out on two sides by an APD array using photon beams scanned in the  $x$ -direction over the center of the crystal.*

Surface Finish	FWHM (mm)	FWTM (mm)
Polished, Teflon clad	0.64	2.76
Rough, Teflon clad	0.55	2.73
Polished, absorbing clad	0.57	2.76
Rough, absorbing clad	0.56	2.71
Specular reflecting	0.62	2.81

TABLE A.2: *Simulation results for the spatial resolution of the five different detector geometries using beams scanned in the  $x$  and  $y$ -direction over the crystal.*

Detector geometry	$x$ -direction		$y$ -direction	
	FWHM (mm)	FWTM (mm)	FWHM (mm)	FWTM (mm)
$20\times 10\times 10$ mm <sup>3</sup> LSO	0.84	3.24	0.90	3.60
$20\times 10\times 20$ mm <sup>3</sup> LSO	0.64	2.76	0.62	2.98
$20\times 14(10)\times 20$ mm <sup>3</sup> LSO	0.66	2.82	0.68	2.99
$20\times 10\times 20$ mm <sup>3</sup> LaBr <sub>3</sub>	0.48	2.28	0.54	2.66
$20\times 20\times 20$ mm <sup>3</sup> LSO	0.60	1.90	–	–

This agrees with the results from Fig. A.2, where the differences between the surface finishes were also very small.

The resolutions obtained from the beam simulations for the different crystal geometries are shown in table A.2. The results agree quite well with the results obtained for the lower bounds in these crystals: the  $20\times 10\times 10$  mm<sup>3</sup> LSO crystal performs worst, probably caused by the fact that most interactions occur furthest away from the APD array, the two 20 mm thick LSO crystals with double sided read out perform equally well, and the LaBr<sub>3</sub> crystal performs best. According to the results for the Cramér-Rao lower bound presented in the previous section, the  $20\times 20\times 20$  mm<sup>3</sup> LSO crystal and the  $20\times 10\times 20$  mm<sup>3</sup> LaBr<sub>3</sub> should perform approximately equally well. The FWHM for the  $20\times 20\times 20$  mm<sup>3</sup> LSO crystal is larger than the FWHM for the  $20\times 10\times 20$  mm<sup>3</sup> LaBr<sub>3</sub> crystal, but the FWTM is smaller.

## A.5 Conclusion

In this paper the use of the Cramér-Rao lower bound has been proposed for investigating the intrinsic spatial resolution performance of PET detector modules. This performance measure makes a better understanding of the influence of different design parameters on the spatial resolution possible. Firstly, because the measure does not depend on the specific algorithm used to estimate the entry

points, secondly because the performance of a detector can be investigated as a function of all three coordinates, and finally because the influence of individual parameters can be made explicit. For example, the effect of the number of primary photons and the quantum efficiency of the APD array on the lower bound can be directly seen from (A.6).

In the derivation of the Cramér-Rao lower bound it is assumed that the ability to estimate the entry point of an impinging annihilation photon is related to the ability to estimate the position of a point source of optical photons within the block. If the lower bound is to be used as a meaningful performance measure, it should give the same relative ordering of the performance of different designs as obtained from beam simulations. From the results presented in the previous section this does indeed appear to be the case.

In order to illustrate the method, the influence of surface finish, crystal geometry, and pixel size on the performance were investigated. For the sake of simplicity, only the influence of light transport and detection were investigated. From these simulations a few interesting observations can be made. First of all, it appears that the surface finish of the monolithic scintillator crystals has little influence on the intrinsic resolution of the detector. The polished or rough Teflon clad surfaces therefore appear to be a good choice, because the reflective cladding may improve the energy resolution and the timing properties of the detector.

Several observations can be made concerning the crystal geometries. First, it can be concluded that  $\text{LaBr}_3$  is an interesting material for further study. Its high light yield improves the lower bound by approximately a factor of 1.5, but the quantum efficiency of the APD has not yet been taken into account. This will have an influence, because the quantum efficiency of the Hamamatsu S8550 for the peak wavelength of  $\text{LaBr}_3$  is smaller than for the peak wavelength of LSO, viz. 50% compared to 70%. Taking these numbers into account, the improvement is reduced to approximately  $\sqrt{0.5/0.7} \cdot 1.5 = 1.3$ , see (A.6), which is still substantial. Secondly, increasing the thickness of the  $20 \times 10 \times 10 \text{ mm}^3$  crystal in order to increase the sensitivity, without adding more APD arrays, is not possible without severely degrading the spatial resolution. Thirdly, tapered crystals, which could improve the sensitivity when placed in a ring, perform as well as rectangular blocks. Finally, the  $20 \times 20 \times 20 \text{ mm}^3$  crystal read out on all sides by single APDs seems promising, since it gives a uniform resolution throughout the detector, but the large area of the APDs in this design will probably lead to a significant increase in the electronic noise, because of a larger dark current and increased detector capacitance. Electronic noise will therefore have to be taken into account in the model, before any definite conclusions can be drawn with respect to this design.

From the comparison of the lower bound for the  $20 \times 10 \times 20 \text{ mm}^3$  crystal for the different APD pixel sizes it appears that the smallest pixel sizes perform best regarding the resolution in the  $x$ -coordinate, even though the statistics in the number of optical photons detected per pixel will be worse, and the total number of detected optical photons is also smaller because of the increased amount of dead space between the pixels. This result may change when we add electronic noise to our model, because the electronic noise will have more influence if the number of detected photons per channel is less.

The method derived in this paper has one important limitation, which is the fact that the influence of Compton scattering is ignored. This will especially have an influence when different scintillators are compared to each other. However, when geometries with approximately the same dimensions and using the same scintillator material are compared, the influence of Compton scattering will be the same for all geometries. The model used to illustrate the method is still relatively simple and ignores the influence of quantum efficiency and electronic noise. The quantum efficiency is approximately constant for a given combination of APD array and scintillator and is furthermore a constant factor in the lower bound (see (A.6)). Therefore, when only the quantum efficiency is added to the model, the conclusions concerning the surface finish, single or double sided read out and pixel size will not change for the Hamamatsu S8550 APD array combined with the LSO crystal. However, as the previous discussion showed, adding electronic noise to the model might influence some of the conclusions. We are therefore working on including electronic noise in our models in order to investigate its influence on the performance.

## A.6 Acknowledgments

We would like to thank Lucas van Vliet and Michel Defrise for their helpful advice and discussions, and professor Uwe Pietrzyk for allowing us to do some of our computations on his computer cluster.

## APPENDIX B

---

### Derivation of the covariance matrix

---

In this appendix equation (4.18) is derived. The covariance matrix for the binomial selection has already been given in equation (4.17).

We will first derive the covariance matrix for the APD amplification process. The diagonal elements were already given in equations (4.4) and (4.5):

$$\text{cov}(n_i, n_i) = \text{var}\{M\}E[n_{eh,i}] + \text{var}\{n_{eh,i}\}\overline{M}^2. \quad (\text{B.1})$$

In order to derive the off-diagonal elements, we use the following relation

$$\text{cov}(\underline{x}, \underline{x}) = E[\underline{x}\underline{x}^T] - E[\underline{x}]E[\underline{x}]^T. \quad (\text{B.2})$$

The second order moment of the number of output electrons is defined as

$$E[n_i n_j] = \sum_{n_{eh,i}=0}^{\infty} \sum_{n_{eh,j}=0}^{\infty} E[n_i n_j | n_{eh,i}, n_{eh,j}] \text{Pr}(n_{eh,i}, n_{eh,j}). \quad (\text{B.3})$$

Since the amplification process in each APD pixel is independent of that in all the others, the number of output electrons in each APD pixel, given the numbers of primary electron-hole pairs, is independent of the others. Therefore,

$$E[n_i n_j] = \sum_{n_{eh,i}=0}^{\infty} \sum_{n_{eh,j}=0}^{\infty} E[n_i | n_{eh,i}] E[n_j | n_{eh,j}] \text{Pr}(n_{eh,i}, n_{eh,j}). \quad (\text{B.4})$$

The expectation value of the number of output electrons for a given number of electron-hole pairs is the expectation value of the gain times the number of electron-hole pairs. Therefore,

$$E[n_i n_j] = \overline{M}^2 \sum_{n_{eh,i}=0}^{\infty} \sum_{n_{eh,j}=0}^{\infty} n_{eh,i} n_{eh,j} \text{Pr}(n_{eh,i}, n_{eh,j}) = \overline{M}^2 E[n_{eh,i} n_{eh,j}]. \quad (\text{B.5})$$

Using equation (B.2) for both  $E[n_i n_j]$  and  $E[n_{eh,i} n_{eh,j}]$ , the off-diagonal elements of the covariance matrix of the number of output electrons are given by

$$\begin{aligned} \text{cov}(n_i, n_j) &= \overline{M}^2 E[n_{eh,i} n_{eh,j}] - E[n_{eh,i}] \overline{M} E[n_{eh,j}] \overline{M} \\ &= \overline{M}^2 (E[n_{eh,i} n_{eh,j}] - E[n_{eh,i}] E[n_{eh,j}]) = \overline{M}^2 \text{cov}(n_{eh,i}, n_{eh,j}). \end{aligned} \quad (\text{B.6})$$

Combining equations (4.17), (B.1) and (B.6) gives

$$\begin{aligned} \text{cov}(n_i, n_j) &= \text{var}\{M\} \overline{n}_{eh,i} \delta_{ij} + \overline{M}^2 \text{cov}(n_{eh,i}, n_{eh,j}) \\ &= \text{var}\{M\} \varepsilon f_i(\underline{x}) \overline{n}_{ph} \delta_{ij} + \overline{M}^2 \varepsilon f_i(\underline{x}) \overline{n}_{ph} (\delta_{ij} + \varepsilon(\alpha^2 - 1) f_j(\underline{x})) \\ &= \overline{M}^2 \varepsilon f_i(\underline{x}) \overline{n}_{ph} \left\{ \left( \frac{\text{var}\{M\}}{\overline{M}^2} + 1 \right) \delta_{ij} + \varepsilon(\alpha^2 - 1) f_j(\underline{x}) \right\} \\ &= \overline{M}^2 \varepsilon f_i(\underline{x}) \overline{n}_{ph} (J \delta_{ij} + \varepsilon(\alpha^2 - 1) f_j(\underline{x})) \end{aligned} \quad (\text{B.7})$$

Since the contribution of the electronic noise is completely independent of the other contributions, the covariance matrix of the output signals  $\Sigma$  is given by

$$\Sigma_{ij} = \overline{M}^2 \varepsilon f_i(\underline{x}) \overline{n}_{ph} (J \delta_{ij} + \varepsilon(\alpha^2 - 1) f_j(\underline{x})) + \sigma_e^2 \delta_{ij} \quad (\text{B.8})$$

---

## Bibliography

---

- [1] *Geant4 physics reference manual*, geant4 7.0 december 2004 ed., December 2004.
- [2] *Geant4 user's guide for application developers*, geant4 7.1 june 2005 ed., June 2005.
- [3] M.C. Abreu, J.D. Aguiar, F.G. Almeida, P. Almeida, et al., *Design and evaluation of the clear-pem scanner for positron emission mammography*, IEEE Transactions on Nuclear Science **53** (2006), no. 1, 71–77.
- [4] L. E. Adam, J. S. Karp, and M. E. Daube-Witherspoon, *Evaluation of performance of the CPET scanner using standardized measurement techniques*, IEEE Nuclear Science Symposium and Medical Imaging Conference Record, vol. 3, IEEE, 2000, pp. 17/46–17/50.
- [5] S. Agostinelli, J. Allison, K. Amako, J. Apostolakis, et al., *GEANT4 - a simulation toolkit*, Nuclear Instruments and Methods in Physics Research A **506** (2003), no. 3, 250–303.
- [6] P. P. Antich, N. Malakhov, R. Parkey, N. Slavin, and E. Tsyganov, *3D position readout from thick scintillators*, Nuclear Instruments and Methods in Physics Research A **480** (2002), 782–787.
- [7] H.H. Barrett and K.J. Myers, *Foundations of image science*, John Wiley & Sons, 2004.
- [8] M. D. Birowosuto, P. Dorenbos, C. W. E. van Eijk, K. W. Krämer, and H. U. GÜdel, *Scintillation properties of LuI<sub>3</sub>:Ce<sup>3+</sup>-high light yield scintillators*, IEEE Transactions on Nuclear Science **52** (2005), no. 4, 1114–1118.
- [9] A. Braem, L. Chamizo, E. Chesi, J. G. Correia, F. F. Garibaldi, et al., *Feasibility of a novel design of high resolution parallax-free Compton enhanced PET scanner dedicated to brain research*, Physics in Medicine and Biology **49** (2004), 2547–2562.

- [10] P. Bruyndonckx, S. M. A. Léonard, J. Liu, S. P. K. Tavernier, P. Szupryczynski, and A. Fedorov, *Study of spatial resolution and depth of interaction of APD-based PET detector modules using light sharing schemes*, IEEE Transactions on Nuclear Science **50** (2003), no. 5, 1415–1419.
- [11] P. Bruyndonckx, S. M. A. Léonard, S. P. K. Tavernier, C. Lemaître, O. Devroede, Y. Wu, and M. Krieguer, *Neural network-based position estimators for PET detectors using monolithic LSO blocks*, IEEE Transactions on Nuclear Science **51** (2004), no. 5, 2520–2525.
- [12] Ciprian Catana, Daniel Procissi, Yibao Wu, Martin S. Judenhofer, Jinyi Qi, Bernd J. Pichler, Russell E. Jacobs, and Simon R. Cherry, *Simultaneous in vivo positron emission tomography and magnetic resonance imaging*, Proceedings of the National Academy of Sciences of the United States of America **105** (2009), no. 10, 3705–3710.
- [13] A. F. Chatziioannou, *Molecular imaging of small animals with dedicated PET tomographs*, European Journal of Nuclear Medicine and Molecular Imaging **29** (2002), no. 1, 98–114.
- [14] S. R. Cherry, *In vivo molecular and genomic imaging: new challenges for imaging*, Physics in Medicine and Biology **49** (2004), R13–R48.
- [15] S. R. Cherry, Yiping Shao, S. Siegel, R. W. Silverman, E. Mumcuoglu, K. Meadors, and M. E. Phelps, *Optical fiber readout of scintillator arrays using a multi-channel PMT: a high resolution PET detector for animal imaging*, IEEE Transactions on Nuclear Science **43** (1996), no. 3, 1932–1937.
- [16] D. Clément, R. Frei, J. Loude, and C. Morel, *Development of a 3D position sensitive scintillation detector using neural networks*, IEEE Nuclear Science Symposium and Medical Imaging Conference Record, vol. 3, IEEE, 1998, pp. 1448–1452.
- [17] T. M. Cover and P. E. Hart, *Nearest neighbor pattern classification*, IEEE Transactions on Information Theory **IT13** (1967), no. 1, 21–&.
- [18] J.T.M. de Haas, P. Dorenbos, and C.W.E. van Eijk, *Measuring the absolute light yield of scintillators*, Nuclear Instruments and Methods in Physics Research A **537** (2005), 97–100.
- [19] S. Delorme, R. Frei, C. Joseph, J. Loude, and C. Morel, *Use of a neural network to exploit light division in a triangular scintillation crystal*, Nuclear Instruments and Methods in Physics Research A **373** (1996), 111–118.
- [20] T. A. DeVol, W. W. Moses, and S. E. Derenzo, *Monte Carlo optimization of depth-of-interaction resolution in PET crystals*, IEEE Transactions on Nuclear Science **40** (1993), no. 2, 170–174.
- [21] P. A. Dokhale, R. W. Silverman, K. S. Shah, R. Grazioso, R. Farrell, J. Glodo, M. A. McClish, G. Entine, V.-H. Tran, and S. R. Cherry, *Performance measurements of a depth-encoding PET detector module based on*

- position-sensitive avalanche photodiode read-out*, Physics in Medicine and Biology **49** (2004), no. 18, 4293–4304.
- [22] P. Dorenbos, J. T. M. de Haas, and C. W. E. van Eijk, *Non-proportionality in the scintillation response and the energy resolution obtainable with scintillation crystals*, Nuclear Science, IEEE Transactions on **42** (1995), no. 6, 2190–2202.
- [23] A. A. R. Fremout, R. Chen, P. Bruyndonckx, and S. P. K. Tavernier, *Spatial resolution and depth-of-interaction studies with a PET detector module composed of LSO and an APD array*, IEEE Transactions on Nuclear Science **49** (2002), no. 1, 131–138.
- [24] T. R. Gentile, J. M. Houston, and C. L. Cromer, *Realization of a scale of absolute spectral response using the National Institute of Standards and Technology high-accuracy cryogenic radiometer*, Applied Optics **36** (1996), no. 22, 4392–4403.
- [25] G. E. Golub and C. F. Van Loan, *Matrix computations*, North Oxford Academic, London, 1986.
- [26] E. Gramsch, R. E. Avila, and P. Bui, *Measurement of the depth of interaction of an LSO*, IEEE Transactions on Nuclear Science **50** (2003), no. 3, 307–312.
- [27] J. S. Huber and W. W. Moses, *Conceptual design of a high-sensitivity small animal PET camera with  $4\pi$  coverage*, IEEE Transactions on Nuclear Science **46** (1999), no. 3, 498–502.
- [28] J. S. Huber, W. W. Moses, M. S. Andreaco, and O. Petterson, *An LSO scintillator array for a PET detector module with depth of interaction measurement*, IEEE Transactions on Nuclear Science **48** (2001), no. 3, 684–688.
- [29] J. S. Huber, W. W. Moses, and P. R. G. Virador, *Calibration of a PET detector module the measures depth of interaction*, IEEE Transactions on Nuclear Science **45** (1998), no. 3, 1268–1272.
- [30] S. Jan, G. Santin, D. Strul, S. Staelens, K. Assié, et al., *GATE: a simulation toolkit for PET and SPECT*, Physics in Medicine and Biology **49** (2004), 4543–4561.
- [31] Y.C. Jean, H. Nakinishi, L.Y. Hao, and T.C. Sandreczki, *Anisotropy of free-volume-hole dimensions in polymers probed by positron-annihilation spectroscopy*, Physical Review B **42** (1990), no. 15, 9705–9708.
- [32] A. P. Jeavons, R. A. Chandler, and C. A. R. Dettmar, *A 3D HIDAC-PET camera with sub-millimetre resolution for imaging small animals*, IEEE Transactions on Nuclear Science **46** (1999), no. 3, 468–473.
- [33] Martin S. Judenhofer, Hans F. Wehrl, Danny F. Newport, Ciprian Catana, Stefan B. Siegel, et al., *Simultaneous PET-MRI: a new approach for functional and morphological imaging*, Nature Medicine **14** (2008), 459–465.

- [34] M. Khodaverdi, S. Weber, M. Streun, Ch. Parl, H. Larue, et al., *High resolution imaging with ClearPET Neuro - first animal images*, IEEE Nuclear Science Symposium Conference Record, vol. 3, 2005, pp. 1641–1644.
- [35] C. Knoess, S. Siegel, A. Smith, D. Newport, R. Richerzhagen, A. Winkeler, A. Jacobs, R. N. Goble, R. Graf, K. Wienhard, and W. D. Heiss, *Performance evaluation of the microPET R4 PET scanner for rodents*, European Journal of Nuclear Medicine and Molecular Imaging **30** (2003), no. 5, 737–747.
- [36] J. W. LeBlanc and R. A. Thompson, *A novel PET detector block with three-dimensional hit position encoding*, IEEE Transactions on Nuclear Science **51** (2004), no. 3, 746–751.
- [37] A. Levin and C. Moisan, *A more physical approach to model the surface treatment of scintillation counters and its implementation into DETECT*, IEEE Nuclear Science Symposium and Medical Imaging Conference Record, vol. 2, IEEE, 1996, pp. 702–706.
- [38] T. K. Lewellen, *Recent developments in PET detector technology*, Physics in Medicine and Biology **54** (2008), R287–R317.
- [39] M. C. Maas, Carel W. E. van Eijk D. J. van der Laan, Freek J. Beekman, P. Bruyndonckx, C. Lemaître, and D. R. Schaart, *Model analysis of the point spread function of monolithic scintillator PET detectors*, submitted to Medical Physics.
- [40] M. C. Maas, D. R. Schaart, D. J. van der Laan, P. Bruyndonckx, C. Lemaître, F. J. Beekman, and C. W. E. van Eijk, *Monolithic scintillator PET detectors with intrinsic depth-of-interaction correction*, Physics in Medicine and Biology **54** (2009), 1893–1908.
- [41] M. C. Maas, D. J. van der Laan, D. R. Schaart, P. Bruyndonckx, C. Lemaître, and C. W. E. van Eijk, *Performance of APD-based monolithic-crystal detectors for small animal PET*, IEEE Nuclear Science Symposium Conference Record, vol. 4, 2005, pp. 2017–2021.
- [42] M. C. Maas, D. J. van der Laan, D. R. Schaart, J. Huizenga, J. C. Brouwer, P. Bruyndonckx, S. Léonard, C. Lemaître, and C. W. E. van Eijk, *Experimental characterization of novel small animal PET detector modules based on scintillation crystal blocks read out by APD arrays*, Nuclear Science Symposium Conference Record, 2004 IEEE, vol. 5, 2004, pp. 2942–2946.
- [43] ———, *Experimental characterization of monolithic-crystal small animal PET detectors read out by APD arrays*, IEEE Transactions on Nuclear Science **53** (2006), no. 3, 1071–1077.
- [44] M. C. Maas, D. J. van der Laan, D. R. Schaart, H. T. van Dam, P. Bruyndonckx, C. Lemaître, and C. W. E. van Eijk, *Signal to noise ratio of APD-based monolithic scintillator detectors for high resolution PET*, IEEE Transactions on Nuclear Science **55** (2008), no. 3, 842–852.

- [45] R. MacDonald L. and M. Dahlbom, *Depth of interaction for PET using segmented crystals*, IEEE Transactions on Nuclear Science **45** (1998), no. 4, 2144–2148.
- [46] ———, *Parallax correction in PET using depth of interaction information*, IEEE Transactions on Nuclear Science **4** (1998), no. 2232, 2237.
- [47] Jan R. Magnus and Heinz Neudecker, *Matrix differential calculus with applications in statistics and econometrics*, third ed., John Wiley & Sons, Chichester, January 2007.
- [48] S. McCallum, P. Clowes, and A. Welch, *A four-layer attenuation compensated PET detector based on APD arrays without discrete crystal elements*, Physics in Medicine and Biology **50** (2005), no. 17, 4187–4207.
- [49] D. P. McElroy, W. Pimpl, B. J. Pichler, M. Rafecas, T. Schuler, and S. I. Ziegler, *Characterization and readout of MADPET-II detector modules: validation of a unique design concept for high resolution small animal PET*, IEEE Transactions on Nuclear Science **52** (2005), no. 1, 199–204.
- [50] S. R. Meikle, Peter Kench, Michael Kassiou, and Richard B. Banati, *Small animal spect and its place in the matrix of molecular imaging technologies*, Physics in Medicine and Biology **50** (2005), R45–R61.
- [51] C. L. Melcher and J. S. Schweitzer, *Cerium-doped lutetium oxyorthosilicate: a fast, efficient new scintillator*, IEEE Transactions on Nuclear Science **39** (1992), no. 4, 502–502.
- [52] L. J. Meng and D. Ramsden, *Performance results of a prototype depth-encoding PET detector*, IEEE Transactions on Nuclear Science **47** (2000), no. 3, 1011–1017.
- [53] R. S. Miyoaka, T. K. Lewellen, H. Yu, and D. L. McDaniel, *Design of a depth of interaction (DOI) PET detector module*, IEEE Transactions on Nuclear Science **45** (1998), no. 3, 1069–1073.
- [54] C. Moisan, M. S. Andreaco, J. G. Rogers, S. Paquet, and D. Voza, *Segmented LSO crystals for depth-of-interaction encoding in PET*, IEEE Transactions on Nuclear Science **45** (1997), no. 6, 3030–3035.
- [55] C. Moisan, A. Levin, and H. Laman, *Testing scintillation transport models with photoelectron yields measured under different surface finishes*, IEEE Nuclear Science Symposium and Medical Imaging Conference Record, vol. 1, IEEE, 1997, pp. 824–828.
- [56] C. Moisan, G. Tsang, J. G. Rogers, and E. M. Hoskinson, *Performance studies of a depth encoding multicrystal detector for PET*, IEEE Transactions on Nuclear Science **43** (1996), no. 3, 1926–1931.
- [57] C. Moisan, D. Voza, and M. Loope, *Simulating the performances of an LSO based position encoding detector for PET*, IEEE Nuclear Science Symposium and Medical Imaging Conference Record, vol. 2, IEEE, 1996, pp. 1211–1215.

- [58] J.-B. Mosset, *Développement d'un module de détection phoswich LSO/LuYAP pour le prototype de caméra à positrons ClearPET*, Ph.D. thesis, Ecole Polytechnique Fédérale de Lausanne, 2006.
- [59] J. B. Mosset, S. Saladino, J. F. Loude, and C. Morel, *Characterisation of arrays of avalanche photodiodes for small animal positron emission tomography*, Nuclear Instruments & Methods in Physics Research Section A **504** (2003), no. 1-3, 325–330.
- [60] H. Murayama, H. Ishibashi, H. Uchida, T. Omura, and T. Yamashita, *Design of a depth of interaction detector with a PS-PMT for PET*, IEEE Transactions on Nuclear Science **47** (2000), no. 3, 1045–1049.
- [61] S. K. Nayar, K. Ikeuchi, and T. Kanade, *Surface reflection: physical and geometrical perspectives*, IEEE Transactions on Pattern Analysis and Machine Intelligence **13** (1991), no. 7, 611–633.
- [62] N. Orita, H. Murayama, H. Kawai, N. Inadama, and T. Tsuda, *Three-dimensional array of scintillation crystals with proper reflector arrangement for a depth of interaction detector*, IEEE Transactions on Nuclear Science **52** (2005), no. 1, 8–14.
- [63] C.M. Pepin, P. Bérard, A.-L. Perrot, C. Pépin, D. Houde, R. Lecomte, C.L. Melcher, and H. Dautet, *Properties of LYSO and recent LSO scintillators for phoswich PET detectors*, IEEE Transactions on Nuclear Science **51** (2004), no. 3, 789–795.
- [64] B. J. Pichler, E. Lorenz, R. Mirzoyan, L. Weiss, and S. I. Ziegler, *Production of a diffuse very high reflectivity material for light collection in nuclear detectors*, Nuclear Instruments and Methods in Physics Research A **442** (2000), 333–336.
- [65] M. Rey, J.-M. Vieira, J.-B. Mosset, M. Moulin Sallanon, P. Millet, J.-F. Loude, and C. Morel, *Measured and simulated specifications of Lausanne ClearPET scanner demonstrator*, Nuclear Science Symposium Conference Record, 2005 IEEE, vol. 4, 2005, pp. 2070–2073.
- [66] D.W. Rickey, R. Gordon, and W. Huda, *On lifting the inherent limitations of positron emission tomography by using magnetic fields (MagPET)*, Automedica **14** (1992), 355–369.
- [67] D. R. Schaart, H. T. van Dam, J. A. Seibert, R. Vinke, R. DenDooven, Löhner H., and F. J. Beekman, *A novel, sipm-array based, monolithic scintillator detector for PET*, Physics in Medicine and Biology **54** (2009), 3501–3512.
- [68] J. Seidel, J. J. Vaquero, and M. V. Green, *Resolution uniformity and sensitivity of the NIH ATLAS small animal PET scanner: comparison to simulated LSO scanners without depth-of-interaction capability*, IEEE Transactions on Nuclear Science **50** (2003), no. 5, 1347–1351.

- [69] J. Seidel, J. J. Vaquero, S. Siegel, W. R. Gandler, and M. V. Green, *Depth identification accuracy of a three layer phoswich PET detector module*, IEEE Transactions on Nuclear Science **46** (1999), no. 3, 485–491.
- [70] Y. Shao, S. R. Cherry, K. Farahani, K. Meadors, S. Siegel, R. W. Silverman, and P. K. Marsden, *Simultaneous PET and MR imaging*, Physics in Medicine and Biology **42** (1997), 1965–1970.
- [71] Y. Shao, K. Meadors, R. W. Silverman, R. Farrel, L. Cirignano, R. Grazioso, K. S. Shah, and S. R. Cherry, *Dual APD array readout of LSO crystals: optimization of crystal surface treatment*, IEEE Transactions on Nuclear Science **49** (2002), no. 3, 649–654.
- [72] S. C. Strother, M. E. Casey, and E. J. Hoffman, *Measuring PET scanner sensitivity: relating countrates to image signal-to-noise ratios using noise equivalent counts*, IEEE Transactions on Nuclear Science **37** (1990), no. 2, 783–788.
- [73] A. Stuart and J. K. Ord, *Kendall's advanced theory of statistics volume 1 - distribution theory*, Edward Arnold, London, 1991.
- [74] ———, *Kendall's advanced theory of statistics volume 2 - classical inference and relationship*, Edward Arnold, London, 1991.
- [75] Y. C. Tai, A. F. Chatziioannou, S. Siegel, J. Young, D. Newport, R. N. Goble, R. E. Nutt, and S. R. Cherry, *Performance evaluation of the microPET P4: a PET system dedicated to animal imaging*, Physics in Medicine and Biology **46** (2001), 1845–1862.
- [76] Y. C. Tai, A. F. Chatziioannou, Y. Yongfeng, R. W. Silverman, K. Meadors, S. Siegel, D. F. Newport, J. R. Stickel, and S. R. Cherry, *MicroPET II: design, development and initial performance of an improved microPET scanner for small-animal imaging*, Physics in Medicine and Biology **49** (2003), 1519–1539.
- [77] Y. C. Tai, A. Ruangma, D. Rowland, Siegel S., D. F. Newport, P. L. Chow, and R. Laforest, *Performance evaluation of the microPET Focus: a third generation microPET scanner dedicated to animal imaging*, The Journal of Nuclear Medicine **46** (2005), no. 3, 455–463.
- [78] T. Tsuda, H. Murayama, K. Kitamura, T. Yamaya, E. Yoshida, T. Omura, H. Kawai, N. Inadama, and N. Orita, *A four-layer depth of interaction detector block for small animal PET*, IEEE Transactions on Nuclear Science **51** (2004), no. 5, 2537–2542.
- [79] D. J. van der Laan, M. C. Maas, D. R. Schaart, P. Bruyndonckx, S. Léonard, and C. W. E. van Eijk, *Using Cramér-Rao theory combined with Monte Carlo simulations for the optimization of monolithic scintillator PET detectors*, IEEE Transactions on Nuclear Science **53** (2006), no. 3, 1063–1070.

- [80] D. J. van der Laan, Dennis R. Schaart, Marnix C. Maas, Freek J. Beekman, Peter Bruyndonckx, and Carel W. E. van Eijk, *Optical simulation of monolithic scintillator detectors using GATE/GEANT4*, submitted to Physics in Medicine and Biology.
- [81] C.W.E. van Eijk, *Inorganic scintillators in medical imaging*, Physics in Medicine and Biology **47** (2002), R85–R106.
- [82] K. M. Van Vliet and L. M. Rucker, *Theory of carrier multiplication and noise in avalanche devices. I. One-carrier processes*, IEEE Transactions on Electron Devices **ED-26(5)** (1979), 746–751.
- [83] A. R. Webb, *Statistical pattern recognition, 2nd edition*, John Wiley & Sons, Chichester, 2002.
- [84] S. Yamamoto and H. Ishibashi, *A GSO depth of interaction detector for PET*, IEEE Transactions on Nuclear Science **45** (1998), no. 3, 1078–1082.
- [85] T. Yamashita, M. Watanabe, K. Shimizu, and H. Uchida, *High resolution block detectors for PET*, IEEE Transactions on Nuclear Science **37** (1990), no. 2, 589–593.
- [86] E. Yoshida, Y. Kimura, K. Kitamura, and H. Murayama, *Calibration procedure for a DOI detector of high resolution PET through a Gaussian mixture model*, IEEE Transactions on Nuclear Science **51** (2004), no. 5, 2543–2549.
- [87] K. Ziemons, R. Achten, E. Auffray, A. Bauer, G. Brandenburg, et al., *The ClearPET Neuro scanner: a dedicated LSO/LuYAP phoswich small animal PET scanner*, IEEE Nuclear Science Symposium and Medical Imaging Conference Record, vol. 4, 2004, pp. 2430–2433.
- [88] K. Ziemons, E. Auffray, R. Barbier, G. Brandenburg, et al., *The ClearPET (TM) project: development of a 2nd generation high-performance small animal PET scanner*, Nuclear Instruments and Methods in Physics Research A **537** (2005), no. 1-2, 307–311.

---

## Summary

---

Many detectors for high resolution positron emission tomography (PET) are based on matrices of small scintillating crystals coupled to position-sensitive photo-multiplier tubes. However, much sensitivity is lost because of the dead space between the crystals needed to optically separate the crystals, and these detectors do not correct for depth-of-interaction. A promising alternative that avoids these two problems are monolithic scintillation detectors. These detectors consist of several cubic centimeters of scintillating material coupled on one or more sides to position-sensitive avalanche photo-diode (APD) arrays. The coordinates of the entry point of an incoming gamma photon are estimated from the light distribution on the APD arrays. This is done using a learning algorithm, that uses measured light distributions with known entry points as training data.

Measurements on these detectors have shown that these detectors are very promising for high resolution PET. The sensitivity of a scanner based on these detectors can be much higher than that of a detector based on small scintillation crystals — making dynamic imaging possible — while the spatial resolution appears to be close to that of detectors of current high resolution PET scanners. However, improvements in the spatial resolution are possible by optimizing the design.

Optimization of many detectors (not just monolithic scintillation detectors) is often done on a somewhat ad hoc basis: different modifications to the design are tried based on a vague notion of how the detector works until an improved design is found. However, as the design becomes more complex there are more parameters that can be varied and often it is not completely clear what changes lead to an improvement of the design. Furthermore, building a prototype of a design can be time consuming and expensive. Modelling the detector leads to a better understanding of the behaviour of the detector, which makes optimization more efficient. Also, different detector designs can be compared to each other using the model thereby reducing the need to perform measurements on prototypes.

In this thesis, two different approaches to model monolithic scintillation detectors are used. The first approach uses Monte Carlo simulations, where a model of the physics of the transport of radiation particles is used. A radiation particle can undergo different interactions with the material it is traveling through. The probability of occurrence of each of these interactions depends on the properties of the particle and those of the material. Using these probabilities and

(pseudo) random numbers, a possible trajectory is generated for each particle in the simulation. Results obtained from these simulation mimic those obtained in measurements (although it is possible to obtain information in simulations that is not possible to obtain in measurements). The main advantage of Monte Carlo simulations compared to the other models, lies in the fact that the results of Monte Carlo simulations can be compared more directly to those obtained in measurements.

The most complicated part in Monte Carlo simulations is determining accurate enough values of all the relevant parameters. In chapter 3 it is described how all the relevant parameters can be determined for monolithic scintillation detectors. A comparison of simulations to measurements shows that the simulation results agree very well with those of the measurements. The results obtained from simulations can therefore be used to predict the measurement results for different detector designs thereby reducing the need to perform measurements. Furthermore, it is more easy to vary some parameters in simulations than in measurements, and it is possible to let some parameters take values that are not possible in real measurements; e.g. in measurements there will always be electronic noise, in simulations it is possible to investigate the performance of an detector without electronic noise. This can lead to a better understanding of the behaviour of the detector.

For the second method, the lower bound on the spatial resolution achievable with position-sensitive scintillation detectors is derived. This lower bound depends on the geometry, the light collection statistics and noise parameters of the detector. Assuming that we can find a good position estimation algorithm, a smaller lower bound implies a better spatial resolution. Therefore, this method of calculating the lower bound can be used to optimize the performance of the detector. Furthermore, since the influence of the statistics and noise parameters on the lower bound can be investigated in detail, a better understanding of the behavior of these detectors is obtained. Since it is possible to predict the best possible performance of a detector with this model, it can be used to determine if a given performance requirement can be met with a given detector. Finally, the performance of the position estimation algorithm can be checked, i.e., when the spatial resolution obtained in practice is much higher than the lower bound, the spatial resolution can in principle be improved by improving the estimation algorithm.

In chapter 4 the lower bound is compared to measurements. The spatial resolution found in the measurements is reasonably close to the lower bound. Therefore, the estimation algorithm appears to be performing well and the spatial resolution can not be much improved upon by an improvement of the estimation algorithm. The lower bound is also able to explain the behaviour of the measurements with increasing electronic noise.

In chapter 4 the lower bound is derived on the position estimation of a point source of light in the detector. However, in practice many annihilation photons will undergo multiple interactions before being absorbed. Therefore, the scintillation will no longer be a single point source, but will consist of multiple point sources. In chapter 5 a model is derived that predicts among other things what is the effect of the multiple interactions. The model also predicts the effect of

the finite width of the measurement beam, and that of the estimation algorithm on the spatial resolution. Furthermore, the model is able to explain the observed spatial resolution (as measured by the point spread function).



---

## Samenvatting

---

Detectoren voor hoge resolutie positronen-emissie-tomografie (PET) zijn gewoonlijk gebaseerd op matrices van kleine scintillatiekristallen gekoppeld aan plaatsgevoelige photo-multiplier-buizen. Van de gevoeligheid gaat echter veel verloren door de dode ruimte tussen de kristallen. Deze dode ruimte is nodig om de kristallen optisch van elkaar te scheiden. Verder is het bij deze detectoren ook niet mogelijk om te corrigeren voor de vertekening die ontstaat als de gammafotonen schuin invallen. Monolitische scintillatiedetectoren kunnen beide nadelen vermijden. Deze detectoren bestaan uit een scintillatiekristal van enkele kubieke centimeters gekoppeld aan één of meerdere plaatsgevoelige avalanche-fotodiode-arrays (APD-array). De coördinaat waar de gammafoton binnen komt, wordt geschat uit de verdeling van het scintillatielicht op de APD-arrays. Hiervoor wordt een lerend algoritme gebruikt, dat getraind wordt met lichtverdelingen waarvan de coördinaten bekend zijn.

Metingen hebben reeds laten zien dat monolitische scintillatiedetectoren veelbelovend zijn voor hoge resolutie PET. De gevoeligheid van een scanner gebaseerd op deze detectoren kan veel hoger zijn dan die van een scanner gebaseerd op kleine kristallen. Tegelijkertijd is de plaatsresolutie vergelijkbaar met die van detectoren van huidige hoge resolutie PET-scanners. Verbeteringen in de plaatsresolutie zijn waarschijnlijk echter nog mogelijk door een optimalisatie van het ontwerp.

Bij optimalisatie van PET-detectoren in het algemeen worden vaak verschillende varianten op een detector uitgetprobeerd totdat een detector gevonden wordt die beter werkt dan de vorige. De keuze van welke detectoren uitgetprobeerd worden is vaak gebaseerd op een vaag begrip van de werking van de detector. Echter, naarmate het ontwerp complexer wordt, zijn er meer parameters die gevarieerd kunnen worden en is het vaak niet geheel duidelijk welke aanpassingen tot een verbetering leiden. Verder kan het bouwen en testen van een prototype duur en tijdrovend zijn. Het modelleren van de detector leidt tot een beter begrip van de detector waardoor optimalisatie efficiënter kan plaatsvinden. Verschillende detectorontwerpen kunnen modelmatig met elkaar vergeleken worden waardoor het bouwen van prototypes en het uitvoeren van metingen verminderd kan worden.

In het proefschrift wordt het modelleren van de detectoren op ruwweg twee manieren aangepakt. In het geval Monte-Carlosimulaties wordt het transport van straling door materie gemodelleerd. Een stralingsdeeltje kan meerdere interacties ondergaan in een materiaal. De kans op optreden van ieder van deze interacties

hangt af van de eigenschappen van het deeltje en van het materiaal. Gebruik makend van deze kansen wordt een mogelijke pad gegenereerd voor ieder van de deeltjes in de simulatie. Doordat hiermee nauwgezet de werkelijkheid wordt gesimuleerd, kunnen metingen hiermee nagebootst worden. In de simulaties is het echter mogelijk om zaken waar te nemen die in metingen niet waargenomen kunnen worden. Het voordeel van de Monte-Carlosimulaties is dat de resultaten direct vergelijkbaar zijn met die van metingen.

Ingewikkeld bij Monte-Carlosimulaties is echter het met voldoende nauwkeurigheid bepalen van alle relevante parameters. In hoofdstuk 3 wordt beschreven hoe alle relevante parameters bepaald kunnen worden voor monolitische scintillatiedetectoren. Een vergelijking tussen meting en simulatie laat zien dat de simulatieresultaten goed overeenkomen met de metingen. De simulatieresultaten kunnen daarom gebruikt worden in plaats van metingen, waardoor minder metingen nodig zijn. Verder zijn sommige parameters een stuk makkelijker te variëren in een simulatie dan in de werkelijkheid; het is mogelijk om parameters waarden aan te laten nemen die in de werkelijkheid niet mogelijk zijn. Zo zal er in metingen altijd elektronische ruis zijn. In simulaties is het echter mogelijk om de detector te bestuderen in een situatie waarin er geen ruis is.

Een andere methode om het gedrag van PET-detectoren te bestuderen is door de ondergrens op de plaatsresolutie te bepalen. In hoofdstuk 4 wordt de ondergrens op de plaatsresolutie van monolitische scintillatiedetectoren bepaald. Deze ondergrens hangt af van de geometrie, de statistiek van de lichtdetectie en ruis die de detector toevoegt. Als we aannemen dat we een schattingsalgoritme kunnen vinden die deze ondergrens bereikt of in ieder geval benadert, dan impliceert een lagere ondergrens een betere resolutie. De ondergrens kan daarom gebruikt worden om de detector te optimaliseren. Verder kan, omdat de ondergrens afhangt van de statistiek en ruis van de detector, een beter begrip verkregen worden van de invloed van deze parameters op het gedrag van de detector. Omdat het best mogelijke gedrag van een detector bepaald kan worden met dit model, kan worden nagegegaan of een gegeven detector aan gegeven kwaliteitseisen kan voldoen. Als laatste toepassingsmogelijkheid kan de ondergrens gebruikt worden om te bepalen hoe goed een gegeven schattingsalgoritme werkt. Als de resolutie verkregen met het schattingsalgoritme ver van de ondergrens af ligt, kan de plaatsresolutie verbeterd worden door het schattingsalgoritme aan te passen.

In hoofdstuk 4 wordt de ondergrens ook vergeleken met metingen. Hieruit blijkt dat de in de metingen gevonden plaatsresolutie redelijk dicht bij de ondergrens ligt. Het gebruikte schattingsalgoritme blijkt dus goed te werken en er valt dus niet veel winst te halen in een verdere verbetering van het schattingsalgoritme. Verder blijkt de ondergrens ook het waargenomen gedrag van de metingen bij toenemende ruis goed te verklaren.

In hoofdstuk 4 wordt de ondergrens op de plaatsresolutie afgeleid voor een puntbron van licht in de detector. In de praktijk zullen echter veel annihilatiephotonen meerdere interacties ondergaan voordat ze volledig zijn geabsorbeerd. Het scintillatielicht zal in dat geval niet uit één enkele puntbron bestaan, maar uit meerdere puntbronnen. In hoofdstuk 5 wordt een model afgeleid dat onder andere voorspelt wat het effect is van de meerdere interacties op de plaatsresolutie. Het model voorspelt verder ook de invloed van de meet- en testbundel en die van

het schattingsalgoritme. Dit model blijkt de gemeten plaatsresolutie (uitgedrukt in de point-spread-function) goed te kunnen verklaren.



---

## Curriculum Vitae

---

Jan van der Laan was born in Middelharnis in The Netherlands in 1977. He received the VWO (secondary education) diploma from the Regionale Scholengemeenschap Goeree-Overflakkee in Middelharnis in 1996. In September, the same year he started the study of Applied Physics at Delft University of Technology. He received the M.Sc. degree in Applied Physics in 2003. The same year he started the research described in this thesis. This research was performed in the section of Radiation Technology (now Radiation Detection & Medical Imaging) of the department of Radiation Radionuclides & Reactors in the years 2003 to 2009. Currently, Jan van der Laan is employed as a methodologist at Statistics Netherlands.



---

## List of publications

---

### Authored journal papers

D.J. van der Laan, M.C. Maas, D.R. Schaart, P. Bruyndonckx, S. Léonard and C.W.E. van Eijk, *Using Cramér-Rao theory combined with Monte Carlo simulations for the optimization of monolithic scintillator PET detectors*, IEEE Transactions on Nuclear Science 53 (2006), no. 3, 1063–1070.

D.J. van der Laan, M.C. Maas, H.W.A.M. de Jong, D.R. Schaart, P. Bruyndonckx, C. Lemaître and C.W.E. van Eijk, *Simulated performance of a small-animal PET scanner based on monolithic scintillation detectors*, Nuclear Instruments and Methods in Physics Research A 571 (2007), 227–330.

D.J. van der Laan, D.R. Schaart, M.C. Maas, F.J. Beekman, P. Bruyndonckx and C.W.E. van Eijk, *Optical simulation of monolithic scintillator detectors using GATE/GEANT4*, submitted to Physics in Medicine and Biology.

M.C. Maas, D.J. van der Laan, F.J. Beekman, C.W.E. van Eijk, P. Bruyndonckx, C. Lemaître and D.R. Schaart, *Model analysis of the point spread function of monolithic scintillator PET detectors*, submitted to Medical Physics.

D.J. van der Laan, D.R. Schaart, M.C. Maas, P. Bruyndonckx, F.J. Beekman and C.W.E. van Eijk, *Spatial resolution in position-sensitive scintillation detectors: influence of statistics and noise*, in preparation.

### Other

M.C. Maas, D.J. van der Laan, D.R. Schaart, H.T. van Dam, P. Bruyndonckx, C. Lemaître and C.W.E. van Eijk, *Signal to noise ratio of APD-based monolithic scintillator detectors for high resolution PET*, IEEE Transactions on Nuclear Science 55 (2008) no. 3, 842–852.

M.C. Maas, D.J. van der Laan, D.R. Schaart, J. Huizenga, J.C. Brouwer, P. Bruyndonckx, S. Léonard, C. Lamaître and C.W.E. van Eijk, *Experimental characterization of monolithic-crystal small animal PET detectors read out by APD arrays*, IEEE Transactions on Nuclear Science 53 (2006), no. 3, 1071–1077.

M.C. Maas, D.R. Schaart, D.J. van der Laan, P. Bruyndonckx, C. Lamaître, F.J. Beekman and C.W.E. van Eijk, *Monolithic scintillator PET detectors with intrinsic depth-of-interaction correction*, Physics in Medicine and Biology 54 (2009), 1893–1908.

S. Jan, G. Santin, D. Strul, S. Staelens, K. Assié *et al.*, *GATE: a simulation toolkit for PET and SPECT*, Physics in Medicine and Biology 49 (2004), vol. 49, 4543–4561.

D.J. van der Laan, M.C. Maas, D.R. Schaart, P. Bruyndonckx, S. Léonard and C.W.E. van Eijk, *Performance optimization of continuous detector modules using Cramér-Rao theory combined with Monte Carlo simulations*, 2004 IEEE Nuclear Science Symposium Conference Record, vol. 4, IEEE, 2004, pp. 2417–2421.

D.J. van der Laan, M.C. Maas, D.R. Schaart, P. Bruyndonckx, C. Lamaître and C.W.E. van Eijk, *Spatial resolution in position-sensitive monolithic scintillation detectors*, 2006 IEEE Nuclear Science Symposium Conference Record, vol. 4, IEEE, 2006, pp. 2506–2510.

M.C. Maas, D.J. van der Laan, D.R. Schaart, P. Bruyndonckx, C. Lamaître and C.W.E. van Eijk, *Performance of APD-based monolithic-crystal detectors for small animal PET*, 2005 IEEE Nuclear Science Symposium Conference Record, vol. 4, IEEE, 2005, pp. 2017–2021.

M.C. Maas, D.J. van der Laan, D.R. Schaart, P. Bruyndonckx, C. Lamaître and C.W.E. van Eijk, *Signal to noise ratio of monolithic scintillator detectors for high resolution PET*, 2006 IEEE Nuclear Science Symposium Conference Record, IEEE, 2006.

M.C. Maas, D.J. van der Laan, D.R. Schaart, J. Huizenga, J.C. Brouwer, P. Bruyndonckx, S. Léonard, C. Lamaître and C.W.E. van Eijk, *Experimental characterization of novel small animal PET detector modules based on scintillation crystal blocks read out by APD arrays*, 2004 IEEE Nuclear Science Symposium Conference Record, vol. 5, IEEE, 2004, pp. 2942–2946.